POLITECNICO DI TORINO

MASTER's Degree in Aerospace Engineering

MASTER's Degree Thesis

Planetary Sunshade for Solar Geoengineering: Precursor Mission for Shading the Solar Radiation Reflected by the Moon

Supervisors

Prof. Marcello ROMANO

Ph.D. Candidate: Catello Leonardo MATONTI

Ph.D. Candidate: Marina COCO

Candidate

Christian BELLINAZZI

December 2024

Summary

Since the onset of industrial development in the eighteenth century, climate change has increasingly threatened natural ecosystems and human society, driving the urgent need for innovative, large-scale solutions to mitigate its impact. In particular, space-based geoengineering has emerged as a promising strategy, offering a global scale intervention. Among these methods, the Planetary Sunshade System, based on Solar Radiation Modification, aims to reduce the oncoming solar radiation, thereby mitigating the greenhouse effect and the rise of Earth's temperature.

The main motivation behind this project lies in evaluating some of the critical technologies of a Planetary Sunshade System. In this perspective, a precursor mission demonstrator is designed. The mission scenario consists on deploying a solar-sail in proximity of the photo-gravitational equilibrium point L_1^*, where solar radiation pressure and gravitational pull balance. Using a CubeSat platform, chosen for its cost-effectiveness and rapid development cycle, the project aims to define optimal sizing and deployment parameters, including radius and mass, alongside essential supporting subsystems.

The preliminary design proposed covers the mission analysis and deployment mechanism tested for structural resilience under operational stresses. The main contributions consist first on the CubeSat's mass optimization, considering typical solar-sail lightness parameters from the literature. Subsequently, the orbit design is performed in the Sun–Earth–Moon Bi-Circular Restricted Four-Body Problem framework by exploiting the solar radiation pressure through attitude control. Finally, the sail deployment mechanism is presented, focusing on mechanical, electrical, and physical considerations. The mechanical analysis evaluates maximum stresses, strains, and vibrational modes to ensure resonance frequencies remain well above the operating ones of the electric motor. The electrical system is designed to ensure efficient motor operation with minimal energy consumption. The deployment mechanism employs four tape-measure booms, and a 1:3.8 scale model of the sail has been constructed to verify it can deploy without tearing.

Acknowledgements

I would like to express my gratitude to Prof. Marcello Romano and Prof. Chantal Cappelletti, as well as entire ASTRADORS and NOTTSPACE teams, for the incredible opportunity to work on groundbreaking topics I never explored before. This experience pushed me to challenge myself like never before, struggling to continuously make a meaningful impact. I am especially grateful to my supervisors, Leonardo, Marina, Takuto and Nishanth, for their invaluable guidance on how to continuously improve my skills.

A heartfelt thank you goes to my family, for their unwavering support, always providing me needed motivation to keep pushing forward. To my friends, thank you for all memorable times spent with lightheartedness and relaxation. A remarkable mention go to that person without whom I would never have achieved this long-held dream, Prof. Gianni Conte. His lessons, both didactic and life ones, sparked a passion in me that I never imagined could shape me into the person I have become today. I am deeply grateful to him.

This amazing journey was been long and challenging, full of obstacles and difficulties, but these remarkable individuals have turned it into a path of personal mind growth. The road to fully-learn our surrounding reality through science is still long, but I firmly believe that the only limit we can face is that one imposed by our own imagination, the imagination to shape our existence in the best way. This belief has driven me through the preparation and final drafting of this project, with the hope that it marks the beginning of a bright and hopeful future, despite all challenges life constantly throws our way. As my family has always taught me, only through tenacity, perseverance and respect there could be achieved dreams and life objectives. I truly hope that this would be only the beginning of a long journey, with many more chapters yet to be written.

"Look again at that dot. That's here. That's home. That's us. There is no hint that help will come from elsewhere to save us from ourselves. It is up to us."

Carl Sagan

Table of Contents

List of Tables

List of Figures

Acronyms

GHG
GreenHouse Gases

CR3BP
Circular Restricted Three Body Problem

BCR4BP
Bi-Circular Restricted Four Body Problem

ESA
European Space Agency

JPL
Jet Propulsion Laboratory

NASA
National Aeronautics and Space Administration

JAXA
Japan Aerospace Exploration Agency

ROSCOSMOS
State Corporation for Space Activities

COM
Center Of Mass

CP
Center of Pressure

SRM

Solar Radiation Modification

SRP

Solar Radiation Pressure

SPE

Solar Particle Events

GCR

Galactic Cosmic Rays

AU

Astronomical Unit

IC

Initial Condition

BVP

Boundary Value Problem

BC

Boundary Condition

ACS

Attitude Control System

IMS

International Measurement System

GPIO

General Purpose Input/Output

Chapter 1

Introduction

1.1 Climate Change as Global Survival Warning

Natural and scientific research highlights the fragility of Earth's climate and its vulnerability to cyclical variations driven by seemingly random events such as earthquakes, storms, and desertification. While some narratives suggest that such adversities are essential for human progress, others argue that this perspective cannot justify the rampant pollution that exacerbates ecological crises.

Historically the industrial revolution, beginning of the 18^{th} century, significantly impacted the environment, releasing huge quantities of particulate into atmosphere. This trend persisted through both world wars but also during last decades which have seen substantial technological advancements. This emergency has always more become of interest for space industry, supported by favorable political and economic policies, further focused on those applications aimed to solve global issues.

Fiction often portrays the extinction of natural species as an inevitable aspect of human evolution, conflating it with celebrated technological advancements, while overlooking its roots in climate change. Since the first atmospheric measurements in the 1950s, humanity has grown increasingly aware of the long-term consequences of rising global temperatures on the planet.

Significant social progress has positioned humankind to confront complex challenges like climate change, with solutions ranging from renewable energy production to large-scale artificial structures in space. One such innovative solution-central to this project involves deploying artificial systems to reduce the amount of solar energy that reaches Earth. This approach aims to lower global temperatures and protect vulnerable species of flora and fauna from the impacts of climate change.

Figure 1.1: ***Climate change, two sides of the same coin [1].***

"Everybody talks about weather, but nobody does anything to preserve it"

These famous words were spoken by Mark Twain in 1897, an American writer and humorist who dedicated much of his energy to exploring social issues, including pollution and the human impact on nature. It is evident that natural events are unpredictable and often result not only from human activities but also from external forces affecting our planet. Volcanic eruptions, flooding, hurricanes, and earthquakes contribute significantly to the sense of unpredictability surrounding these events, further complicating our understanding of their effects on Earth's ecosystems and the species that inhabit them.

1.1.1 Historical Natural Disasters

This project is supported by a series of historical examples and, as cited in [**2**], the first put into evidence is that referable in 1883, when *Krakatoa Volcano* erupted letting the skies becoming dark over many countries all over the world, staying so for months and years.

Figure 1.2: ***Krakatoa eruption, May 20 to August 26, 1883 [2].***

This has been one of the most explosive eruptions ever happened on Earth and it was been capable of decreasing the Earth's global mean temperatures of $1[°C]$, letting its surface colder than previously. Supporting this discussion, an other

Figure 1.3: ***New Orleans aftermath after Katrina's dissolvation [3].***

important historical event bound to climate change is *hurricane Katrina in 2005*,

as described in [**3**], which crushed the southern coast of USA, provoking floodings and electricity black-outs, as shown in **figure 1.3**, that is still considered one of the worst natural disasters in US history, displacing 1.2 million people.
The principal causes which had brought to this unpredictable event were been not only natural but also leadable back to the poor conditions in which local populations were usual to live. Scientists, and sector experts, agreed to the need of putting into evidence what could modify, after it, in terms of climate stability and consequences for natural species living the Earth. Katrina is actually a reminder to how much cruel may be natural disasters on human lives and always regarding to preserve the slight equilibrium between all natural species living our planet.

An example, instead coming from the American Filmography comes through an end of the world blockbuster, truly well-known in the natural scientific fields, maybe a little hasty to imagine for which could happen, in light of its quick developing

Figure 1.4: ***Los-Angeles hit by multiple twisters [4].***

events. It treats the Earth's climate changes in only a few days, after reaching the critical de-salting point in the Atlantic Ocean, and in several other seas in the world, bringing to catastrophic natural events, such as heavy thunder-storms, floodings and tsunamis. The film is named *The day after tomorrow*, **figure 1.4**, and it's become very famous not only for its cutting-edge special effects, but highlighting the increasing global warming temperatures' problem to both the public and the state-leades , giving the audience a certain sense of loss and carelessness so much crucial to all species that populates the Earth since the human wasn't even born to live the Earth.
On the same way, cataclysmic events imagined in the film *Geostorm* are not less spectacular and poor of imagination. In this case human capabilities have realized

a planetary climate-control system, whose Earth may be entirely surrounded by orbital-constellation of satellites for nullifying the eventual storms that would arise. Taking apart the filmography plot, its improved background makes the observer being directly launched inside both political intrigues and environmental-issues consciousness. In particular this last reflects how things are quickly modifying although all programmed interventions decided by politicians, putting into foreground all human incapabilities to face them.
Pollution is radically modifying the atmosphere composition to something so dangerous to our healthy, the rainy drop conditions which are reducing the water brought to specific locations, provoking drought and havoc. On the opposite side, mainly in the equatorial's bend, for lower Latitudes, the tropical-storms hitting mainly the under-developed countries, giving an higher sense of frustration and resignation to local populations.

Figure 1.5: ***Arab Emirates' shores hit by tsunamis provoked by a satellite's signal-loss [5].***

A truly different example, but not less noteworthy, is brought by the un-predictable movement of glaciers' basements, well-known as *"Glacial Earthquakes"*, as illustrated in [**6**], which happen always more often both in Northern, Southern territories relative to the equatorial Earth's plane, for higher and lower Latitudes. Below have been shown two different examples of just introduced, in **figure 1.6** and in **figure 1.7**. The increasing temperatures are melting the most cold ice situated in these Glaciers' core and this is due to a peak of frequency in summer months, although they had found a stabilizing positive rate of events. These events, like the previous ones, are very difficult to foresee and this is one of the most remarkable motifs that lead to them, not only for human's healthy but also for that of the natural's biodiversity care, causing deforestations and desertifications.

Figure 1.6: ***Trift Glacier, Switzerland, retreated by 1.17 km between 2006 and 2015, James Balog's collection [6].***

Figure 1.7: ***Columbia Glacier, Alaska, retreated by 6.5 km between 2009 and 2015, James Balog's collection [6].***

To counter-act the Greenhouse-effect, the international community is pronounced to confine the increasing global temperatures to the limit-threshold of $1.5°C$, in order that the mainly $C0_2$ levels in the atmosphere couldn't reach the critical 'stagnation' condition we would all be affected living beneath them. Moreover, most of countries in the world have decided to act supporting this ideological point of view contributing, each on their own, by reducing the emission of the green-house gases, trying to prevent a possible and catastrophic $2°C$ temperatures' limit, still

thought nowadays as the no-return way to uncontrollable natural disasters.

Someone already doesn't believe we have gathered this problem from null to a concrete sense of impotence and, what's most difficult to comprehend, who thinks that all these problems could be simply solved by passing from gasoil to electric cars should be in trouble. It's remarkable that these problems may be associated to the human-kind actions and not to its direct existence on Earth, and technological enhancements reached in the last centuries prove how much incredibly rapid could be believing in a better future of wellness and prosperity.

Turning our point to the discussion introduced at first, the climate change is inevitable and requires an higher understandable-level in order to match it as best as possible, supporting the possible solutions adopting, not only direct ways such as the reduction of pollution levels in the Earth's atmosphere, but also unconventional techniques taken-out by the reason of existence, which gives us so much incredible belonging senses, also associated to human's wills and wishes.

This project focuses on this specific theme, trying to look for an answer that could reflect a possible mitigation process, as just made in the previous decades by international companies, countries, scientists and engineers. The next steps to be followed need an higher level of responsibility, which goes, by hand in hand, from technological behavior thoughts to something still only imagined and never tried to have done, this for denying natural carelessness of its dwellers.

1.1.2 Pollution Affecting Temperatures' Rising

To pursue these purposes, several researches have demonstrated how the global *GHG* emissions could be potentially fatal for advising an overshoot in temperatures.

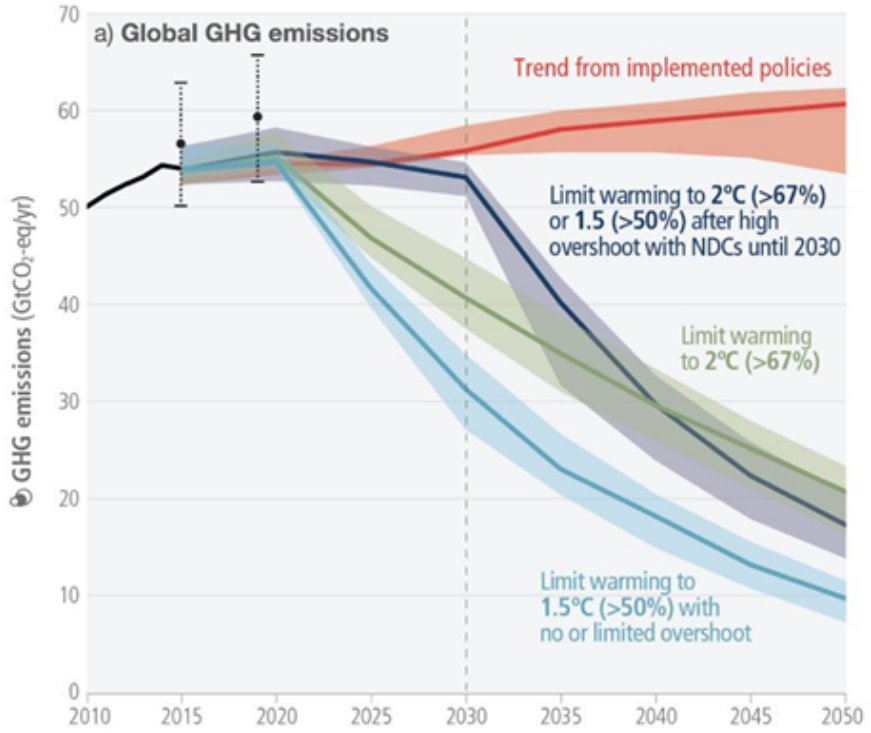

Figure 1.8: ***GHG emissions and projections until 2050 [7].***

The first boundary year assumed as reference for the increasing pollution concentrations is 2030, in which all the global countries that had decided to contribute to the Earth's survival need to respect by reducing of 26% the overall emissions, as discussed in [**7**]. It could be useful to examine which type of emissions are on the grounds of the energy absorption, inducing the Greenhouse-effect and compensating the increasing pollution levels. Physically speaking, this phenomena reduces the emissivity properties on the upper atmosphere particles, hence bringing inevitably to a major effect of radiation pressure coming from the Sun, and not only.

At this historical-time, several global-governments are looking for prevention-methods to let giving a reasonable solution for this problem, for example discussing about the technology green-passage of cars but also industrial mechanics, in order

to reduce harmful gases. The decarbonization perspectives results to be fundamental to the Earth's survival, regarding that the natural climate is always in equilibrium between several Ice Ages and desertification ones. Temperatures have always suffered these natural cycles and, what's been changed, the human activities risks to accelerate these processes, bringing all natural species to the extinction.

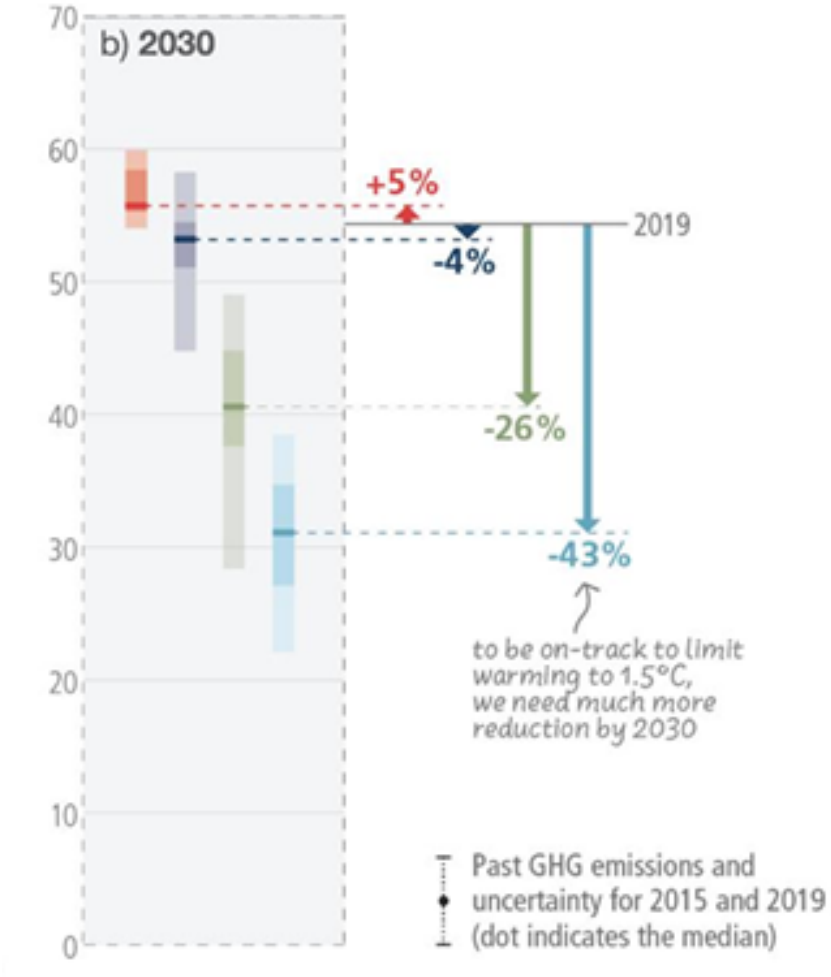

Figure 1.9: ***GHG reduction for climate change mitigation [7].***

The definition of climate change needs to be used also in these context, by seeing to the past and looking for a future without the errors committed in the previous centuries. We are far from the industrialization-age that distinguished the passage from the 19^{th} to the modern scientific revolutions-age, but someone thinks that its memory should be always resumed in our minds to learn, and tell, what could be some different solutions to these bigger problems.

The most important harmful emissions are surely the Carbon-Dioxide CO_2 ones, Tropospheric Nitrogen and Sulfur compounds, Carbon-Monoxide and Particulat-matter. These pollution elements trap the total energy, letting consequently the increasing of mean global temperatures. The ***"Kyoto protocol"*** and the ***"Paris climate agreement"***, signed on 11 December 1997 and 12 December 2015 respectively, sounds as an inexorable countdown to what could happen in terms of natural catastrophic events. The so famous net-zero reference appears to be so far to be achieved, for which there would be found a perfect equilibrium between Greenhouse-emissions, due to human activities, and that ones absorbed by Earth.

By the observation of **figure 1.8**, it's clear how the actual implemented trends could be un-successful to lowing down these promised increasing of *GHG* emissions. The first limit, imposed to the 2030, is very close to be reached. These results have been confirmed by the projected reduction levels shown in **figure 1.9**. Actual policies' trend could bring to terrifying effects on increasing these *GHG*s and these images suggest how there would be significant enhancements for being 'on-track' with global expectations. The 43% pollution-reduction until 2030 might be apparently unattainable for the most but it shall be useful trying to give an higher impulse for saving our environment. Lower percentage variations could lead to unsuccessful results and this may oblige the most doing their 'little-own' for making the difference. The previous cited optimal reduction in *GHG*s advised for the 2030's Paris agreement is necessary to be reached to avert a possible, and even worsening, climate change condition, although there would be also a -43% reference to achieve a possible *"on-track path"* to an accelerated full climate restoration.

1.2 Space-based Solar Geoengineering

One of the most reasonable solutions related to climate change mitigation is given by the *"space-based geoengineering"*, in which by using the space technology it could be possible looking for adaptive solutions given by small and large-scale systems and, as a complementary part, adopting other spacecrafts to confirm and foresee all these environmental changes. This project proposes to focus on the large-scale technology one, taking as reference a specific swarm of smaller satellites that, once connected one-another, would let the space-system behaving as a *"light-umbrella"*, whose singular example is shown in **figure 1.10**, capable to reflect a portion of energy and denying it hitting the planet of interest.

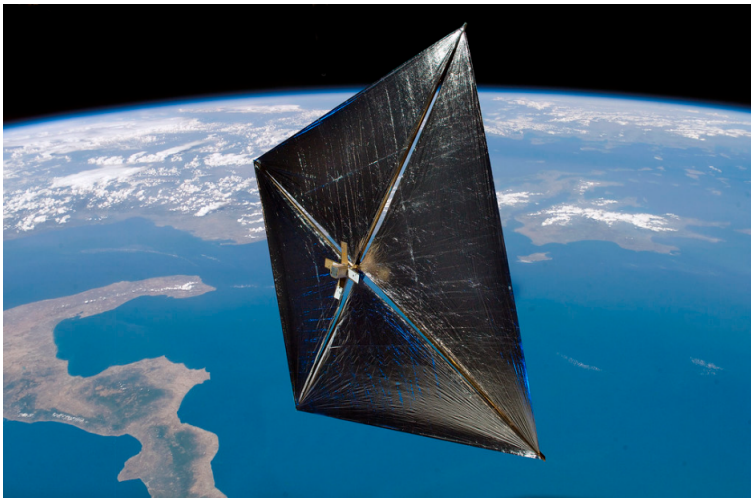

Figure 1.10: ***Reflecting operative solar sail [8].***

These facts appear as science-fiction but, as supported and preliminary advised in [**9**], its scientific potentials have convinced scientists continuing to work on it. This *"space-infrastructure"*, shown in **figure 1.14**, could work as a shading system, between two primary bodies, contributing to control and down-power the total solar-irradiance. The main problems referred to support its realization go from political policies to the economical budgets left available by governments supporting them. Applying numerical simulations it's been demonstrated that these on-orbit assembled structures can grant, considering all technological limitations from launch to deployment phases, a short reduction in global energy irradiance, in this case coming from the Sun. This decreasing percentage of irradiance would let desirable long-term effects for planet Earth, reducing to the mainly CO_2 and CO, and not only, the possibilities of absorbing an higher solar-energy. It's named *"swarm"*, as shown in **figure 1.11**, **figure 1.12** and **figure 1.13** because, on the ground of it, it's thought that it could be possible only launching thousands of thousands of

small satellites and, after have achieved the imagined orbital configuration, instead of taking bigger systems.

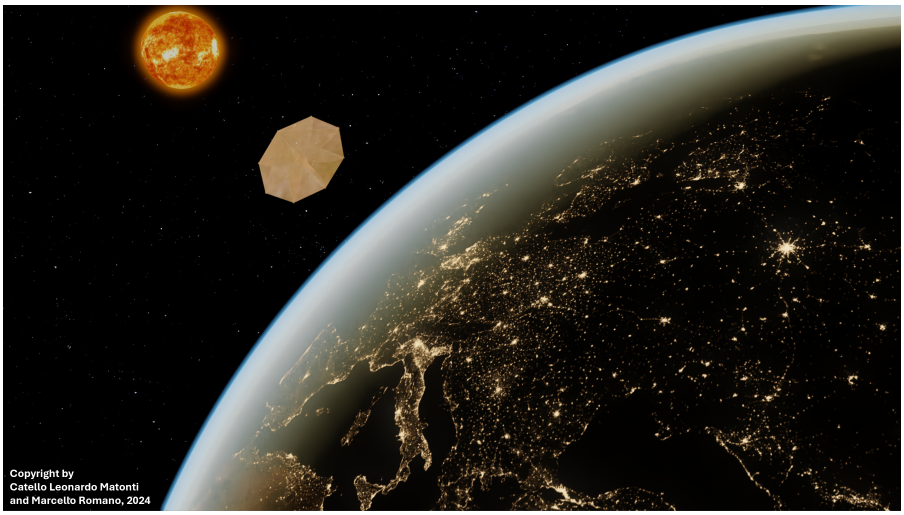

Figure 1.11: ***Conceptual visualization of space-based climate change mitigation strategies, represented by a planetary sunshade composed of a swarm of solar-sail satellites assembled in space [10].***

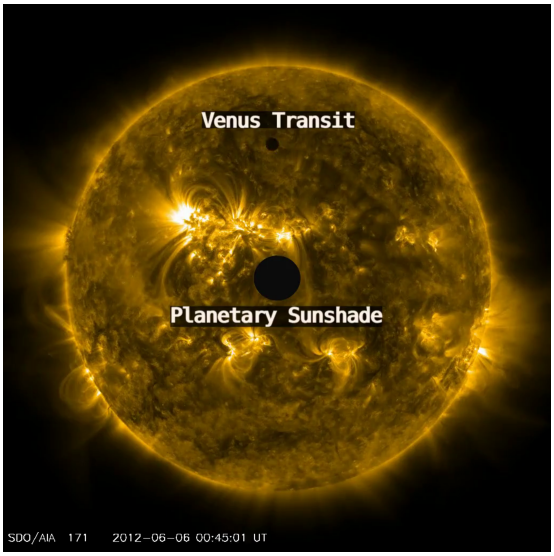

Figure 1.12: ***Mitigation strategy represented by a planetary sunshade system [11].***

If we thought to technical limitations, the astrodynamical, thermal, systems and

attitude analysis needs to be enrolled to the previous technological mixture of issues because of the incredible volatility of space-weather. At these purposes will be needed to take both stochastic and deterministic mathematical processes, letting us to foresee, accepting a certain error percentage, all correct systems' behaviors.

Figure 1.13: ***The Planetary sunshade concept as a swarm of solar sail satellites [9].***

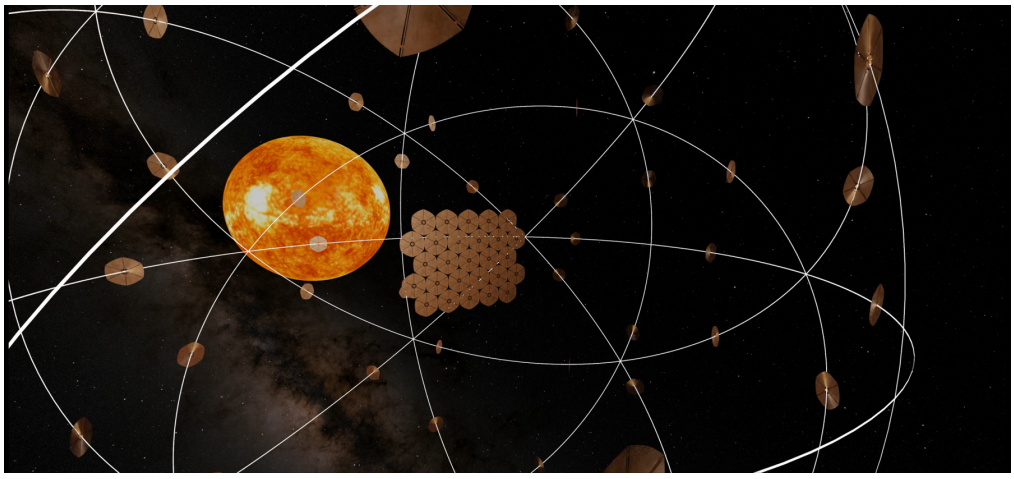

Figure 1.14: ***Solar sails' swarm orbital infrastructure [12].***

During on-Earth test-analysis, all these experiments are led on environmental-controlled pressurized chambers to have everything under direct measurements.

1.3 Solar Sail Technologies

Solar sails are considered one of the most promising solutions for climate change mitigation and space exploration due to their ability to carry large payloads without the need for fuel. By harnessing radiation pressure from sunlight, they generate thrust through momentum transfer, enabling long-duration missions, **figure 1.15**, without propellant use. Applications for solar sails range from interplanetary missions, allowing efficient travel, to both inner/outer planets and Earth-orbiting missions like satellite navigation and communication systems. They can also help extend satellite lifespans, reduce maintenance costs, and even manage space debris by gently de-orbiting objects. Additionally, solar sails offer potential for geoengineering, where large-scale space-based systems could reduce sunlight reaching Earth, helping to mitigate global warming. Solar sails provide a sustainable, scalable, and cost-effective alternative for both deep space exploration and environmental management, making them a vital technology for future interplanetary travels and climate solutions.

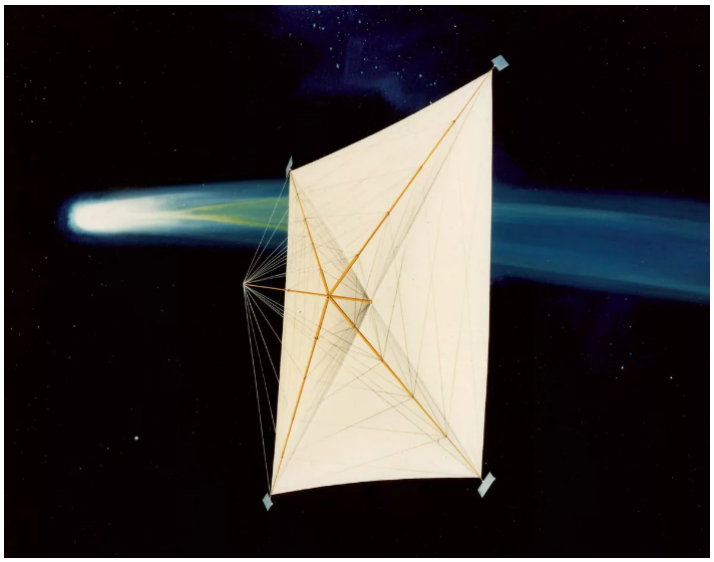

Figure 1.15: ***Approaching sail to Halley's comet, source [13].***

It could be useful to define several orbit classes for learning where and how positioning the solar sail swarm. Going through the history of solar sails, one of the most famous examples of imagine applications was been a vehicle designing capable, one day, to reach the ***Halley's Comet***, conceptually seen in **figure 1.15**. This project began in 1977 at *JPL* for the 1986 passage close the Earth, and the initial goals were to land the equipped probe on its surface. In light of funding problems, the starting of the Shuttle project by NASA and project's deadlines,

these factors contributed to the mission failing scheduled meeting, although all the efforts made. This could be considered, as obvious as, an example of Helio-gyro rendezvous space-mission for a comet interception, result of years of studies and researches that finally brought to an end in failure. Nowadays it's still considered one of the first projects projects that gave a huge impulse to Sun-light spacecrafts' developments, after have been reached in 2010 by *IKAROS* project, developed by *JAXA*.

Figure 1.16: ***Znamya space-mirror over Europe [14].***

At a certain history point, *ROSCOSMOS* decided to invest lots of capitals and time to a series of orbital mirror experiments with the intent of reflecting the Sun-light directly to the Earth. This project was named *Znamya*, shown in **figure 1.16**, nowadays has been considered one of the first examples of Solar-mirrors ever thought , reaching a fully-deployed configuration in 1993, hence three years later the project's starting-date. After several findings, it's been demonstrated that the luminosity factor induced by the mirror was equivalent to that of a full Moon, hence it produced a 5 Km bright spot, which passed from Europe to western Russia. This project could be seen as support to actual technological trends, that imagines to give a realistic-application to pursuing my thesis development, although made only theoretically but analyzing the principles to which found a space-swarm of smaller satellites deploying once stabilized and positioned to the specified project's transfer orbits. Space-mirrors would be extended to the space Sun-Shade concept, a system capable to deflect sunlight and countering global warming.

1.3.1 Solar Sails Paired to CubeSats

The concept of Sun-shading architecture, as introduced in [**15**], was first theorized in 1923 by physicist Hermann Oberth. His general idea has since evolved into a broad range of practical applications, extending to futuristic concepts like cooling the temperatures of Venus to make it potentially habitable for human colonization. Early missions aimed to demonstrate how solar energy could be concentrated or redirected onto specific regions of Earth's surface, creating significant temperature gradients between illuminated and shaded areas, as was attempted with the Znamya project. What remains certain is that engineering solutions alone will never be able to completely halt global warming or reverse rising temperatures. However, by adopting technologies like the Solar sail, experts can mitigate the catastrophic consequences of human activities on Earth, providing a valuable means of slowing down environmental damage. Some experts also believe that this technology could enable humanity to explore distant stars and planets, not necessarily within our solar system, supporting human expansion and the advancement of machines and instruments for space exploration. As with any space mission, however, it is essential to minimize both monetary costs and development time to ensure the project's feasibility, particularly in later stages of implementation. Solar-Sails, or more broadly referred to as ***Lightsails*** whenever paired with CubeSats, offer a promising solution for both interplanetary missions and on-orbit space applications. However, they introduce additional complexities in terms of deployment and attitude control, which must be carefully addressed to ensure successful mission outcomes.

1.4 Project Objectives

The primary goal of this project is to highlight the major challenges involved in designing a complex mechanical system capable of addressing environmental issues on a global scale. The idea of creating a *"planetary shade"* as a potential method for mitigating climate change is not as far-fetched as it might seem, and numerous studies could support its feasibility. While such a passive solution to reduce global mean temperatures may appear bold and unconventional, history particularly in aerospace engineering has shown that groundbreaking results are often achieved by pursuing unorthodox solutions. Thinking outside the ordinary and embracing the limits of human imagination are essential for progress. There is a wide range of possible solutions with the aim of designing a structural and physical system capable of partially shading the Earth's atmosphere throughout its operational lifetime. This project aims to outline a potential framework for such an endeavor, providing a basis for future developments. It seeks to conceptualize a new binary system between the Earth and the Moon, offering an initial sizing of subsystems. Furthermore, the project focuses on selecting and analyzing an attitude dynamics

model to stabilize the entire system along the conjunction line between the two primary bodies. It also explores deployment mechanisms, examining how they might influence the performance of actuation devices.

1.4.1 *PROMETHEUS* Mission Concept

The mission logo was been crafted down to both capture the key-findings of climate change and for representing its purposing scenario. At the center, the projected occulter is depicted, illustrating its periodic trajectory in yellow, surrounded by the stars, the Earth, the Moon, and finally the Sun, illuminating the mission's focal point. The entire concept is based on a symmetrical structure, representing the sail's envisioned final orbit around the photo-gravitational equilibrium point, L_1^*, this for exploiting the external disturbances equilibrium in time. In the foreground, at the top section, various elements such as tornadoes, factories, and burning trees are included, symbolizing the connection between natural disasters and human progress over past centuries. The highest yellow-shaded semicircle represents the greenhouse effect, caused by polluted gases emitted as a consequence of human activities. The overarching idea behind this thesis is to propose a potential working scenario that allows nature to grow and flourish with all its living natural species, for restoring and assuring the world natural order. This is symbolized by the black circular logo placed beneath each of the three key elements previously described.
The ***Prometheus myth*** (one of the Titans coming through the greek mythology) gives us a different perception whenever thinking about modern challenges, especially those related to climate change and potential use of space-based geo-engineering. Prometheus, who stole fire from gods for giving it humans, in a certain sense symbolizes knowledge and progress. His act can be paired to actual humanity's use of technology, harnessing the nature's power to improve our living, like science that look for a solution to solve climate crisis. Fire is representable as human innovation, like those tools we use to learn and forecast climate change. From Greek mythology, Prometheus was punished for stealing fire from gods. This punishment reminds us that from power comes great risks and higher responsibilities. Our industrial progress and exploitation of Earth's resources have led to climate problems we are now facing to. Temperatures' rising and extreme weather conditions are direct consequence of damaged ecosystems we perceive today. By trying to modify the inexorable path humankind is going on, we are taking bold steps towards the availability to control the unpredictable nature behavior. Geo-engineering can offer the correct way to interrupt oncoming even worse human actions affecting global climate, once using it wisely, but it also brings up several and serious interrogatives. Can we foresee all progress consequences? Prometheus represents hope and responsibility due its gift. This must be interpreted as an opportunity to grow, build and prosper with nature, not taking advantage from

Figure 1.17: ***Precursor mission logo.***

exploiting ecosystems' death. It's noticeable how much important would be to understand all risks that come from large-scale interventions, hence accepting our action's consequences without looking back yet. Prometheus story shows us that while human creativity and technology can solve big problems like climate change, they also need to come with caution and optimism. The key is how we care about the unstable balance between power innovation and direct consequences on nature, always perceiving progress with respect for nature.

Chapter 2

Astrodynamics in Sun-Earth-Moon System

This chapter concerns on introducing the mathematical modeling needed to design orbital trajectories for both Sun-Earth and Earth-Moon orbital planes, in which the latter is studied by adopting the Bi-Circular Restricted Four Body Problem pattern. The Sun-Earth modeling is described through Circular Restricted Three Body Problem to highlight most significant modifications to be made in orbital dynamics w.r.t. designing precursor mission delved into Earth-Moon orbital plane frame. The purpose is that of establishing the solar sail's proper capabilities to describe specific orbital trajectories, expected in proximity of L_1, for variable attitude dynamics, hence in absence of thrust or any other control possibly applicable.

2.1 Circular Restricted Three Body Problem

In order to comprehend the basis of the mathematical modeling, it could be possible to define the required gravitational potential forces relatively to the main bodies involved. The *CR3BP* aims to consider the only attraction of three different bodies by adopting the ***synodic reference frame***, centered in $\mathcal{O}$ with focus on Sun-Earth orbital plane, in which it always considers the first two bodies principal (celestial bodies like Earth and Sun), whereas the third is addressed as the solar sail. The radius vector $\mathbf{R}$ describes the solar sail relative position w.r.t. the synodic frame, after have defined the xyz axis, in which x is positively defined from $\mathcal{O}$ to Moon, z going out of plane, whereas y completing the orthonormal triad. $\boldsymbol{d}_1$ and $\boldsymbol{d}_2$ stand for Earth and Moon distances from $\mathcal{O}$, both applied on x-axis. Proposed chart, **figure 2.1**, need to focus on the main forces acting on the system itself and, beginning from that, the first ones applied to our system of reference are the gravitational contributes, in which these lasts should depend on the unit vector

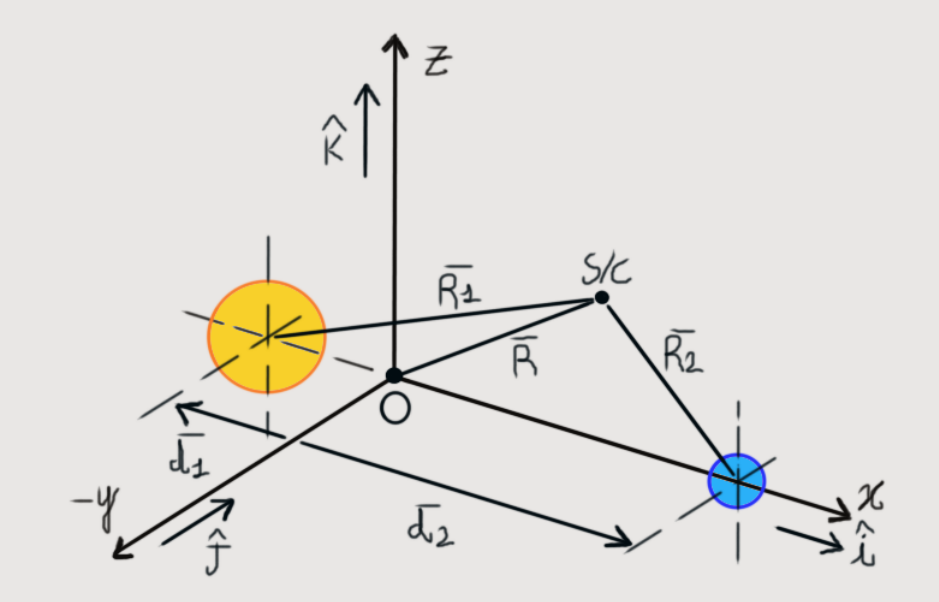

Figure 2.1: ***The CR3BP schematization.***

coupling the sail to each of the main bodies involved. These forces, referring to [**16**], are applicable as:

$$\boldsymbol{F}_s = -G\frac{M_S M_{S/C}}{R_1^2}\frac{\boldsymbol{R}_1}{R_1}$$

$$\boldsymbol{F}_{S/C} = -G\frac{M_T M_{S/C}}{R_2^2}\frac{\boldsymbol{R}_2}{R_2}$$

The first $\boldsymbol{F}_s$ stands for the attractive force due to the Sun, whereas $\boldsymbol{F}_{S/C}$ the equivalent given instead by the Earth. The radius vectors $\boldsymbol{R}_1$ and $\boldsymbol{R}_2$ would depict a continuous primary bodies' attraction, whereas $\boldsymbol{R}$ the generic applied to $\mathcal{O}$. By applying the Newton's second law of motion it's possible to write translational dynamics as:

$$\sum_{i=1}^{N} M_{S/C}\frac{d^2\boldsymbol{R}}{dt^2} = -G\frac{M_S M_{S/C}}{R_1^2}\frac{\boldsymbol{R}_1}{R_1} - G\frac{M_T M_{S/C}}{R_2^2}\frac{\boldsymbol{R}_2}{R_2} \tag{2.1}$$

$$\begin{cases} L^* = \|\boldsymbol{d}_1\| + \|\boldsymbol{d}_2\| \\ M^* = M_S + M_T \\ T^* = \sqrt{\frac{L^{*3}}{\mu}} \end{cases}$$

The characteristic time T^* is a dimensionless factor implemented to the final simulation time and to both primary bodies' angular velocities definition. The

total mass M^* is paired instead to the acceleration process estimation (through the second Newton law). What about L^*, this factor is used, together with T^*, for giving a dimensionless meaning to the 6 *IC*s and to each other parameter that would comprehend a length measurement. In light of the preliminary triad of dimensionless factors just introduced, it's useful to put into evidence the position dimensionless vectors:

$$\begin{cases} \boldsymbol{r} = \frac{\boldsymbol{R}}{L^*} \\ \boldsymbol{r}_1 = \frac{\boldsymbol{R}_1}{L^*} \\ \boldsymbol{r}_2 = \frac{\boldsymbol{R}_2}{L^*} \end{cases}$$

$$\mu = \frac{M_T}{M^*} \rightarrow \mu M^* = M_T \rightarrow \mu \left(M_S + M_T\right) = M_T \rightarrow M_T \left(\mu - 1\right) = -\mu M_S$$

$$M_T \left(1 - \mu\right) = \mu M_S \rightarrow \left(1 - \mu\right) = \mu \frac{M_S}{M_T} = \frac{M_S}{M^*}$$

$$\begin{cases} M_T = \mu M^* \\ M_S = \left(1 - \mu\right) M^* \end{cases}$$

This passage is necessary to consider a dimensionless equation of motion and letting it to show the $\overline{r}$, and equivalents, parameter. It leads to:

$$\frac{d^2\boldsymbol{r}}{dt^2} = -\frac{1-\mu}{\|r_1\|^3}\boldsymbol{r}_1 - \frac{\mu}{\|r_2\|^3}\boldsymbol{r}_2 \tag{2.2}$$

It's possible to define both the position vectors $\boldsymbol{r}_{1,2}$ starting from $\boldsymbol{r}$ and $\boldsymbol{d}_{1,2}$, as shown. Consequently, applying the static Momenta conservation, **equation 2.3**, between both the primary bodies and looking for $\boldsymbol{r}_{1,2}$. $\boldsymbol{d}_1$ will be the complementary part of $\boldsymbol{d}_2$: this is due by taking L^* as the characteristic length to which fix our synodic reference system. The general expression for $\boldsymbol{r}$, and for the consequent $\boldsymbol{r}_1$ and $\boldsymbol{r}_2$ would be:

$$\boldsymbol{r} = \boldsymbol{x}\hat{x} + \boldsymbol{y}\hat{y} + \boldsymbol{z}\hat{z}$$

$$\left(1 - \mu\right) M^* \boldsymbol{d}_1 = \mu M^* (x - \boldsymbol{d}_1) \quad \rightarrow \quad M^* \boldsymbol{d}_1 - \mu M^* \boldsymbol{d}_1 = \mu M^* x - \mu M^* \boldsymbol{d}_1 \tag{2.3}$$

$$\Rightarrow \boldsymbol{d}_1 = \mu x$$

$$\begin{cases} \boldsymbol{d}_1 + \boldsymbol{d}_2 = 1 \\ \boldsymbol{d}_1 = \mu x \\ \boldsymbol{d}_2 = \left(1 - \mu\right) x \end{cases}$$

$$\begin{cases} \boldsymbol{r} = \boldsymbol{r}_1 + \boldsymbol{d}_1 \rightarrow \boldsymbol{r}_1 = \boldsymbol{r} - \boldsymbol{d}_1 = \left(x + \mu\right)\hat{x} + y\hat{y} + z\hat{z} \\ \boldsymbol{r} = \boldsymbol{r}_2 + \boldsymbol{d}_2 \rightarrow \boldsymbol{r}_2 = \boldsymbol{r} - \boldsymbol{d}_2 = \left(x + \mu - 1\right)\hat{x} + y\hat{y} + z\hat{z} \end{cases}$$

$$\|r_1\| = \sqrt{(x+\mu)^2 + y^2 + z^2}$$
$$\|r_2\| = \sqrt{(x+\mu-1)^2 + y^2 + z^2}$$

The angular velocity $\boldsymbol{\omega}$ is defined by its unique z-component, on the grounds of the terrestrial rotational axis position cutting both the poles and assuming to have a Keplerian motion, it could be possible to define:

$$\boldsymbol{\omega} = \left\{ \begin{array}{c} 0 \\ 0 \\ \omega_z \end{array} \right\}$$

We may need to consider both the centrifugal and Coriolis forces acting on a desired rotating synodic reference frame. These two terms figure on the final equation of motion, as treated in **[17]**, yields to:

$$\frac{d^2\boldsymbol{r}}{dt^2} + \boldsymbol{\omega} \wedge (\boldsymbol{\omega} \wedge \boldsymbol{r}) + 2\boldsymbol{\omega} \wedge \dot{\boldsymbol{r}} = -\frac{1-\mu}{\|r_1\|^3}\boldsymbol{r}_1 - \frac{\mu}{\|r_2\|^3}\boldsymbol{r}_2$$

$$\boldsymbol{\omega} \wedge \boldsymbol{r} = \begin{vmatrix} \hat{i} & \hat{j} & \hat{k} \\ 0 & 0 & \omega_z \\ x & y & z \end{vmatrix} = (-\omega y)\,\hat{i} - (-\omega x)\,\hat{j} + (0)\,\hat{k} = \begin{pmatrix} 0 & -\omega y & 0 \\ \omega x & 0 & 0 \\ 0 & 0 & 0 \end{pmatrix} \begin{pmatrix} \hat{i} \\ \hat{j} \\ \hat{k} \end{pmatrix}$$

$$\boldsymbol{\omega} \wedge (\boldsymbol{\omega} \wedge \boldsymbol{r}) = \begin{vmatrix} \hat{i} & \hat{j} & \hat{k} \\ 0 & 0 & \omega_z \\ -\omega y & \omega x & 0 \end{vmatrix} = \left(-\omega^2 x\right)\hat{i} - \left(+\omega^2 y\right)\hat{j} + (0)\,\hat{k} = \begin{pmatrix} -\omega^2 x & 0 & 0 \\ 0 & -\omega^2 y & 0 \\ 0 & 0 & 0 \end{pmatrix} \begin{pmatrix} \hat{i} \\ \hat{j} \\ \hat{k} \end{pmatrix}$$

$$2\boldsymbol{\omega} \wedge \dot{\boldsymbol{r}} = \begin{vmatrix} \hat{i} & \hat{j} & \hat{k} \\ 0 & 0 & 2\omega_z \\ \dot{x} & \dot{y} & \dot{z} \end{vmatrix} = (-2\omega\dot{y})\,\hat{i} - (-2\omega\dot{x})\,\hat{j} + (0)\,\hat{k} = \begin{pmatrix} 0 & -2\omega\dot{y} & 0 \\ 2\omega\dot{x} & 0 & 0 \\ 0 & 0 & 0 \end{pmatrix} \begin{pmatrix} \hat{i} \\ \hat{j} \\ \hat{k} \end{pmatrix}$$

The final equation of motion resumes together the Centrifugal, Coriolis and Gravitational dimensionless accelerations through-out 6 *IC*s, which comprehend 3 positions and 3 velocities paired to the gravitational parameter μ and to the main bodies' radius vectors $\boldsymbol{r}_i$. The actual potential function, **figure 2.2**, is definable as:

$$\mathcal{U} = \frac{1-\mu}{\|r_1\|} + \frac{\mu}{\|r_2\|} + \frac{x^2+y^2}{2} \tag{2.4}$$

Final equations of dynamics could be written down yielding:

$$\begin{aligned} \ddot{x} - x - 2\dot{y} &= -\frac{(1-\mu)}{\|r_1\|^3}(x+\mu) - \frac{\mu}{\|r_2\|^3}(x+\mu-1) \\ \ddot{y} - y + 2\dot{x} &= -\frac{(1-\mu)}{\|r_1\|^3}y - \frac{\mu}{\|r_2\|^3}y \\ \ddot{z} &= -\frac{(1-\mu)}{\|r_1\|^3}z - \frac{\mu}{\|r_2\|^3}z \end{aligned} \tag{2.5}$$

2.1.1 Libration Equilibrium Points

The restricted problem was been deeply worked, for the first time, by two famous scientists named Lagrange, lived in the 18^{th} century and Poincare in the 19^{th} century, [**18**].

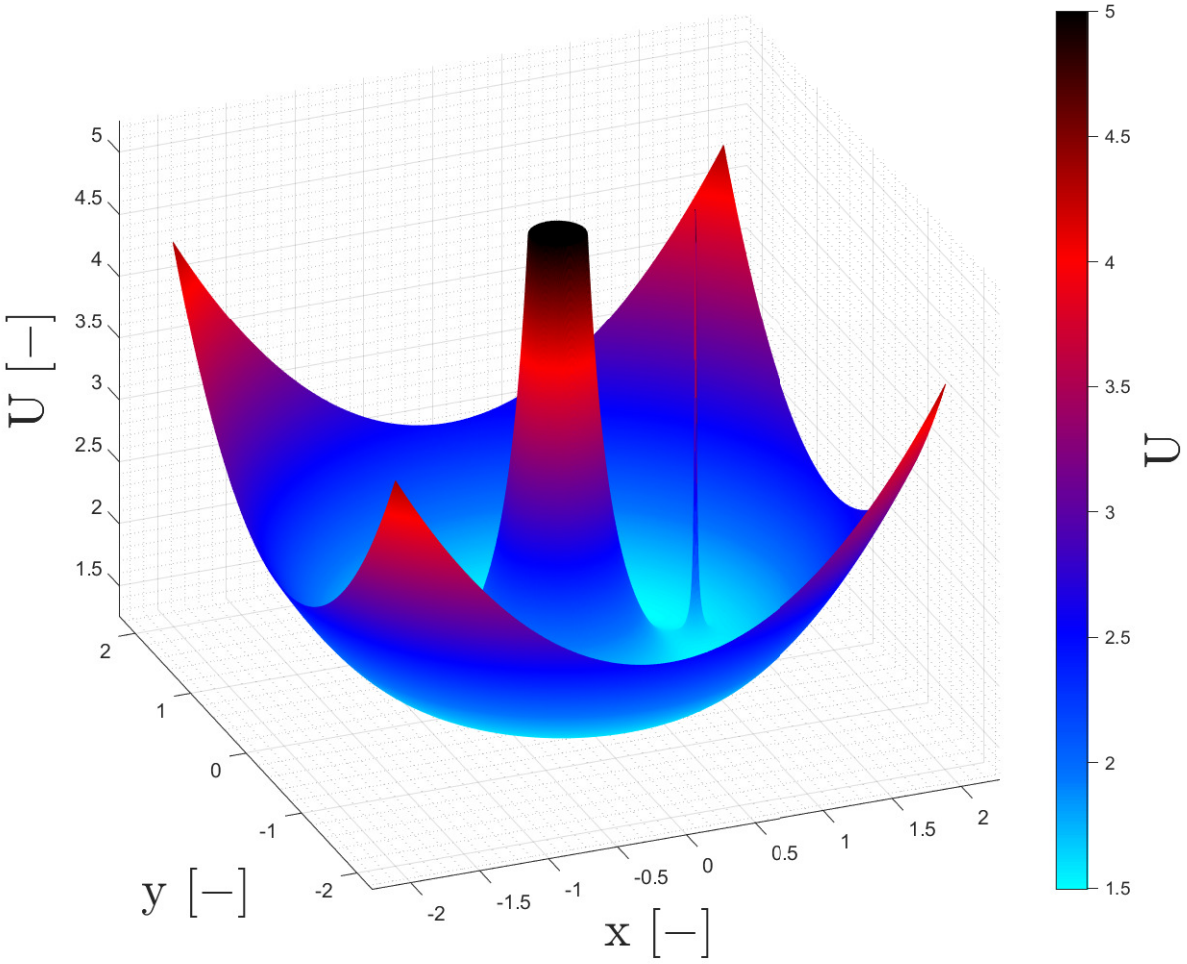

Figure 2.2: ***Potential function $\mathcal{U}$ for CR3BP.***

Despite this problem can't be solved by formulating a mathematical law being able to predict its chaotic behavior, there could be formulated several approximate and particular solutions adopting, for example, both series expansion and numerical methods. If trying to solve the equation of dynamics it could be possible to look for 5 particular solutions called *Lagrangian points* [**19**] [**20**], well-known also as

libration points, **figure 2.3**, to whose a small body, that can easily be designing precursor mission, could stay in proximity to them and comprehended between both the primary bodies involved.

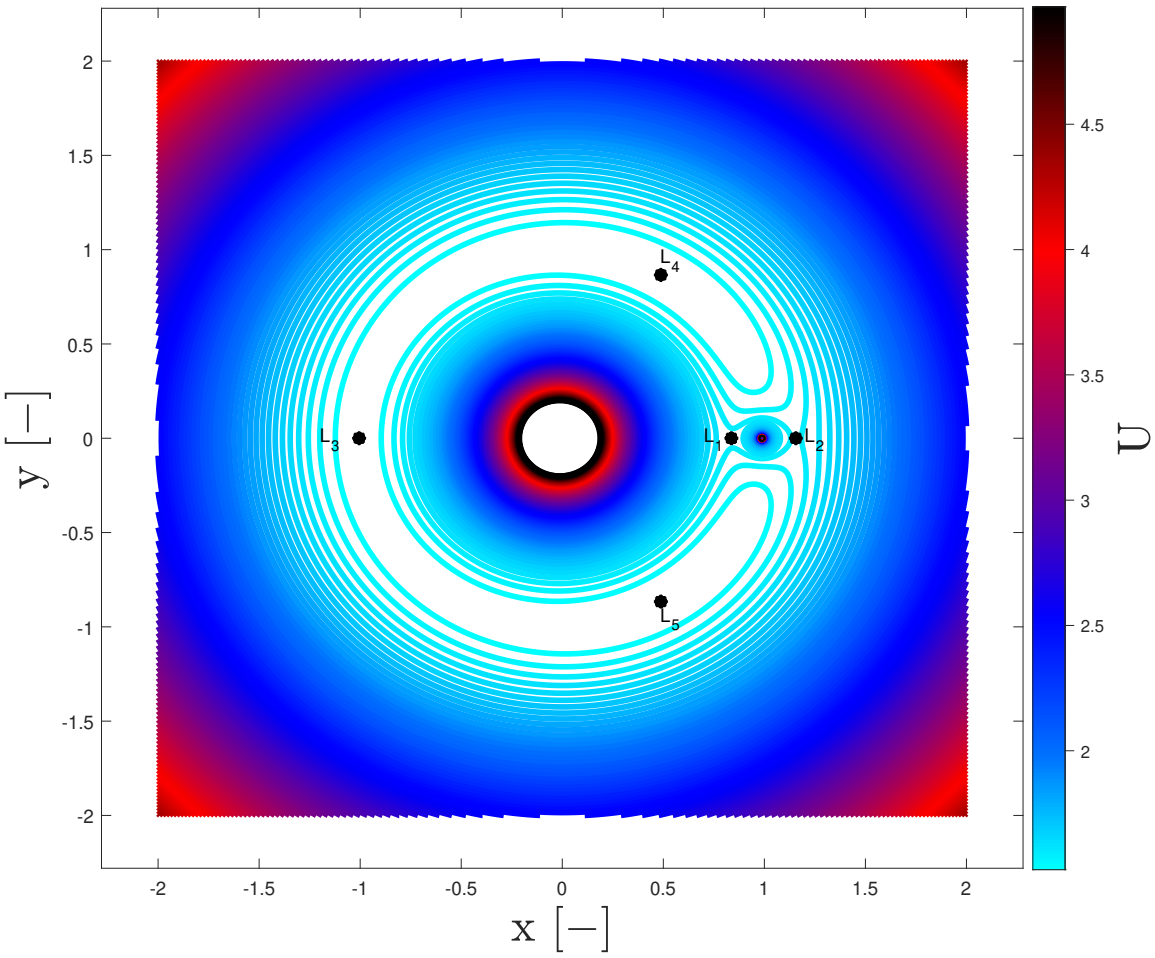

Figure 2.3: ***Libration points on*** xy ***orbital plane.***

Nowadays, lagrangian points are very used for locating space telescopes and other space science missions. Despite these should provide an ideal equilibrium source by only analyzing the gravitational potentials' interacting with the solar-sail, these are also useful to comprehend which could be a possible suiting position between the Earth and Moon for letting the sail staying for long time. There would be found five equilibrium solutions named L_1, L_2, L_3, L_4 and L_5 in which masses M_T and M_S would be that associated to Earth and Moon primary bodies respectively. The

lowest lagrangian point that could be reached for a lower potential energy is L_1, the same that will be taken as reference for this thesis, trying to learn what could change when adding more external disturbances inside the same modeling to its exact estimated position. In general, a third body characterized by a negligible mass should conserve its relative position w.r.t. L_1 (nothing else than the first of three *collinear points*). The typical characteristic of L_1, if taking into account a rotating synodic reference system, should be that of realizing an equilibrium balance between the primary bodies' gravitational fields and centrifugal forces. The static condition that must be satisfied from system of dynamics has to be:

$$\dot{x} = \ddot{x} = \dot{y} = \ddot{y} = \dot{z} = \ddot{z} = 0 \tag{2.6}$$

and substituting inside **equation 2.5** to declare the equilibrium condition:

$$\frac{\partial \mathcal{U}}{\partial x} = \frac{\partial \mathcal{U}}{\partial y} = \frac{\partial \mathcal{U}}{\partial z} = 0 \quad \rightarrow \quad \nabla \mathcal{U} = 0 \tag{2.7}$$

obtained by fixing $z = 0$, hence considering the xy reference plane.

2.1.2 HALO Orbits around Libration Points

Most used orbits exhibit a certain periodicity, as observed in [**21**], and are typically characterized by highly eccentric trajectories coupled with broad stabilizing motions. These orbits are commonly called *HALO*s. *HALO* orbits are three-dimensional, periodic trajectories that could be used close to Lagrangian points. These orbits are useful in systems where a smaller body, such as a spacecraft, orbits in the gravitational field of two primary bodies.

In order to deny these orbits would intersect, it is necessary to impose their angular velocities' components equal for both lateral and out-of-plane ones, hence $\omega_y = \omega_z$. Those periodic solutions usually associated to Lissajous Orbits, which represent one of the most general forms of non-periodic trajectories. These orbits are typically observed in systems around collinear equilibrium points, as discussed in [**22**]. When considering cases in which both primary bodies involved have zero orbital eccentricities, it becomes possible to speak about periodic trajectories. Otherwise, the resulting orbits are often quasi-periodic, forming a particular shape known as *"aureola"*, as illustrated in [**23**]. These quasi-periodic trajectories don't describe perfectly close paths over successive orbits, indicating a slight deviation from perfect periodicity. In systems like Sun-Earth or Earth-Moon orbital planes, these quasi-periodic orbits are crucial for placing space observatories and communication satellites in advantageous locations where they can remain in a stable configuration, while maintaining visibility on targeted regions and granting minimal fuel consumptions.

Historically speaking, the first space-vehicle capable to reach a quasi-periodical orbit around a libration point was been a scientific satellite named ***ISEE-3***, introduced in [**21**], after have been successfully launched in 1978 by using a Delta rocket. The interested collinear-point was that L_1 in the Earth-Sun reference plane and defining an *HALO*, characterized by a huge out-of-plane amplitude coefficient for avoiding solar communications mismatch. In 1982 this probe was repurposed and renamed for flying through the comet *21P/Giacobini-Zinner* plasma tail and then joined several other satellites to study *1P/Halley's comet*.
Continuing this examples' collection, in [**25**] and [**26**] is introduced ***Euclid spacecraft***, a wide-angle space-telescope *("M-Class")* launched on 1 July 2023, reaching an approximate *HALO* orbit around the Earth-Sun gravitational equilibrium-point L_2, gone to join the James Webb and Gaia missions ahead. Euclid aims to better understand both the dark energy and matter in the universe by accurately measuring the accelerating its expansion. It's expected that this mission would last at least six years observing a third of the extragalactic-sky (the bend facing away from the Milky Way). Moreover in [**27**], a space-mission referring to the Earth-Moon

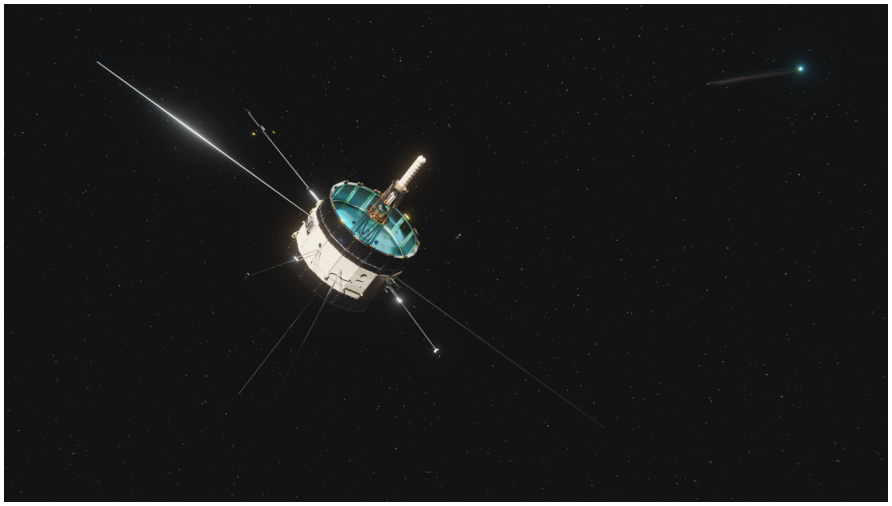

Figure 2.4: ***ISEE-3 and Giacobini-Zinner's comet [24].***

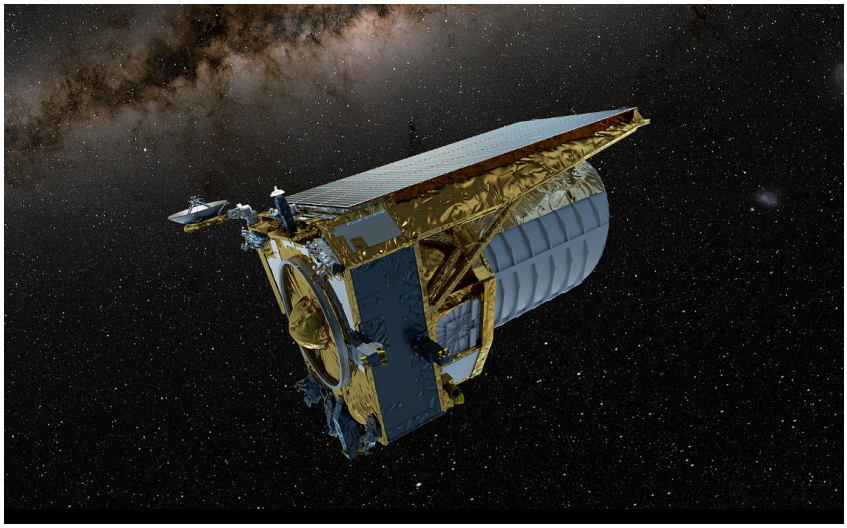

Figure 2.5: ***Euclid's full-operative state [26].***

lagrangian L_1 could be ***THEMIS***, whose operations began in February 2007 as a constellation of five *NASA* satellites for studying magnetosphere releasing effects, well known as substorms. It performed two lunar flybys and an Earth one before describing the insertion into a *Lissajous orbit* around the first gravitational equilibrium point L_1. On the opposite side, as seen in **[29]** and **[30]**, an equivalent Sun-Earth application, always referred to its L_1 equilibrium positioning, should be that named ***LISA Pathfinder*** (***SMART-2***), developed by *ESA*, scientifically started on 8 March 2016 and lasted sixteen months.

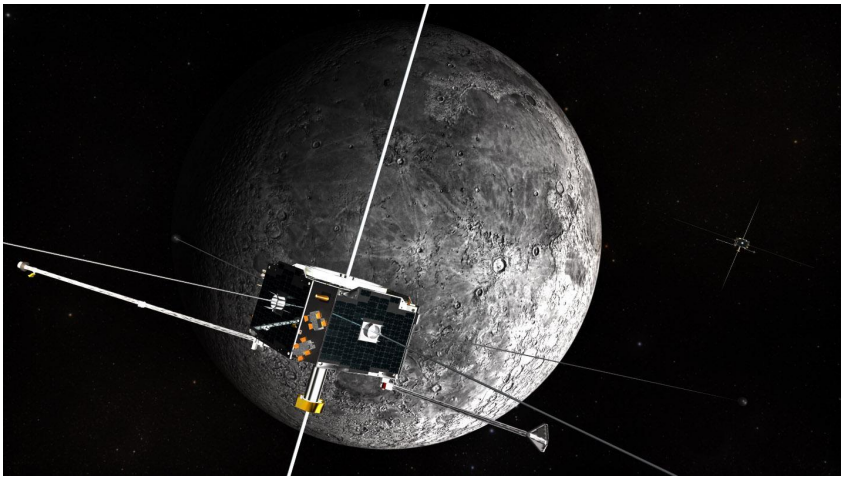

Figure 2.6: ***Lunar-orbiting Themis constellation [28].***

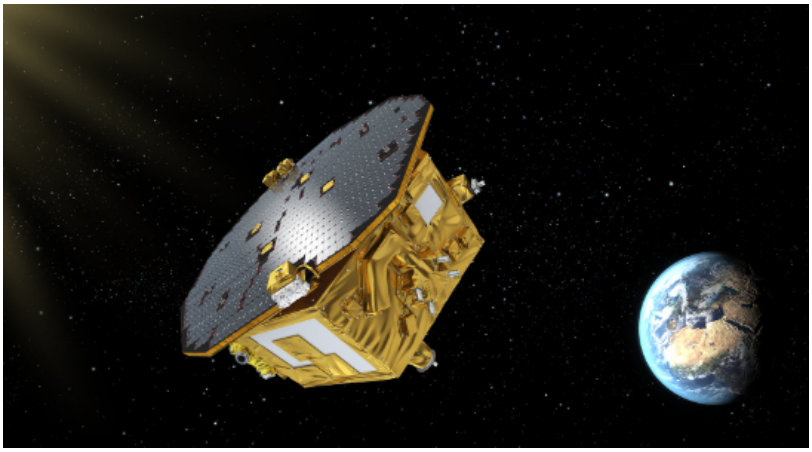

Figure 2.7: ***Pathfinder Probe detecting gravitational waves [30].***

The intent was to demonstrate that two masses (the second was a 2 Kilos testing cube inside the probe) could fly and maintain their relative positions through a nearly perfect gravitational free-fall effect and measuring deviations from geodesic motion, that coming from black-holes and other exotic violent high energy events. The system was successfully brought to an *HALO* around the Earth-Sun L_1 after several short burns from an initial *LEO* parking orbit.
The ***James Webb space telescope***, designed for conducting infrared astronomy after have been launched on 25 December 2021 (considered the successor of Hubble), delved in **[32]** and **[31]**, on an Ariane 5 rocket from Kourou, stands for a great example for L_2 libration point's application in the Earth-Sun reference plane. Webb is actually working on an HALO orbit, circling around this L_2 for approximately

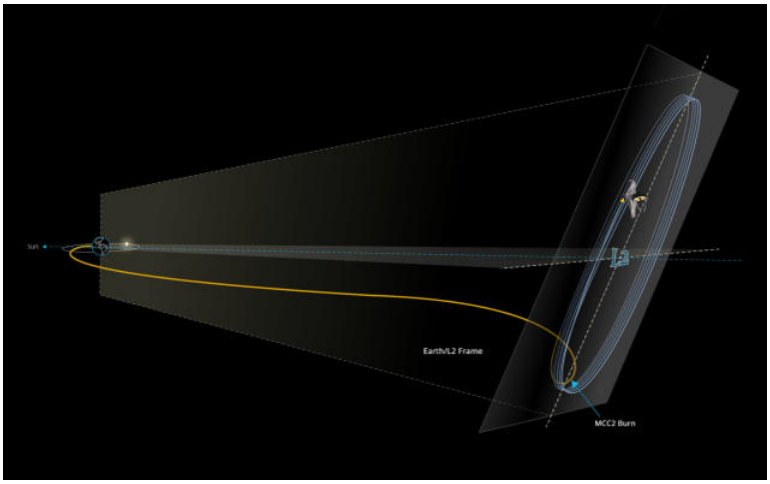

Figure 2.8: ***JWST trajectory reaching*** L_2 ***[31].***

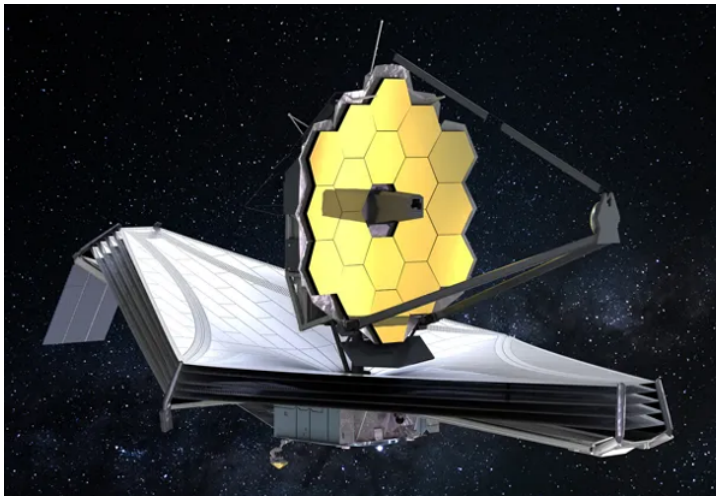

Figure 2.9: ***Fully-deployed JWST, [31].***

1,500,000 Km, thus beyond the Earth's *SOI*. A great advantage for this positioning is that the telescope could block the incoming heat and light from all the primary bodies involved, maintaining uninterrupted both the solar source and terrestrial communications.

2.2 Bi-Circular Restricted Four Body Problem

Afterwords the *CR3BP* introduction, it's been demonstrated what's needed to fulfill the solar sail's motion to the involved primary bodies by considering as the origin of our synodic reference frame $\mathcal{B}_1$, conceptually defined in the same way of $\mathcal{O}$, but retrieved and drawn to the Earth-Moon orbital plane, **figure 2.10**. The general equations of motions could be expressed as:

$$\begin{aligned} \ddot{x} - 2\dot{y} - \frac{\partial \mathcal{U}^*}{\partial x} &= a_x \\ \ddot{y} + 2\dot{x} - \frac{\partial \mathcal{U}^*}{\partial y} &= a_y \\ \ddot{z} - \frac{\partial \mathcal{U}^*}{\partial z} &= a_z \end{aligned} \tag{2.8}$$

This equations' system is Time Variant, hence non autonomous, because the impacting *SRP* depends on the rotating Sun's distinguished motion, as described for a general point P (the solar sail in this way) moving on a generic trajectory [**33**]. It's been assumed that all primary bodies' orbital planes would coincide, hence for example avoiding the 5° angle normally comprehended between Earth and Moon. The required angular velocity $\omega_\odot$ depends on selected reference system and, in this situation, characterized by the sum of two different contributes: ω_M is relative to the Earth-Moon synodic period T_{syn}, whereas $\omega_\oplus$ to Earth's revolution time $T_\oplus$ w.r.t. the Sun:

$$\theta = \omega_\odot t = (\omega_M + \omega_\oplus)\, t = \left(\frac{2\pi}{T_{syn}} + \frac{2\pi}{T_\oplus} \right) t \tag{2.9}$$

The generic triad of axis defined by $(\hat{x}, \hat{y}, \hat{z})$ would be that associated to the synodic reference frame centre position, in which $(\hat{x}, \hat{y})$ have been applied to the motion plane, hence $\hat{z}$ completes the ortho-normal vectorial composition, associated to the exchanged out-of-plane angular momentum. The easiest imagined geometrical visualization of the $[\phi, \epsilon, \tau]$ triad of angles could imagine to take them by applying cosine directors to xyz through dot products, **figure 2.11**, in which there will be coupled the three main radius vectors $r_{k,3}$ (with k = (1,2,4)). These will go to define the connection upon three primary bodies (E, M and S) to the sail's unit vector $\hat{n}$. Moreover, its been decided to define the first three solar sail's position components w.r.t. the Sun's described circular motion w.r.t. the synodic reference frame $\mathcal{B}_1$ center position, definable as:

$$\boldsymbol{r}_{13} = [+x + \mu, +y, +z] \qquad \text{and} \qquad \boldsymbol{r}_{23} = [+x + \mu - 1, +y, +z] \tag{2.10}$$

The modified Sun's gravitational potential $\mathcal{U}^*$, **equation 2.12**, could be written as described in [**34**]. It unifies the primary bodies gravitational accelerations into

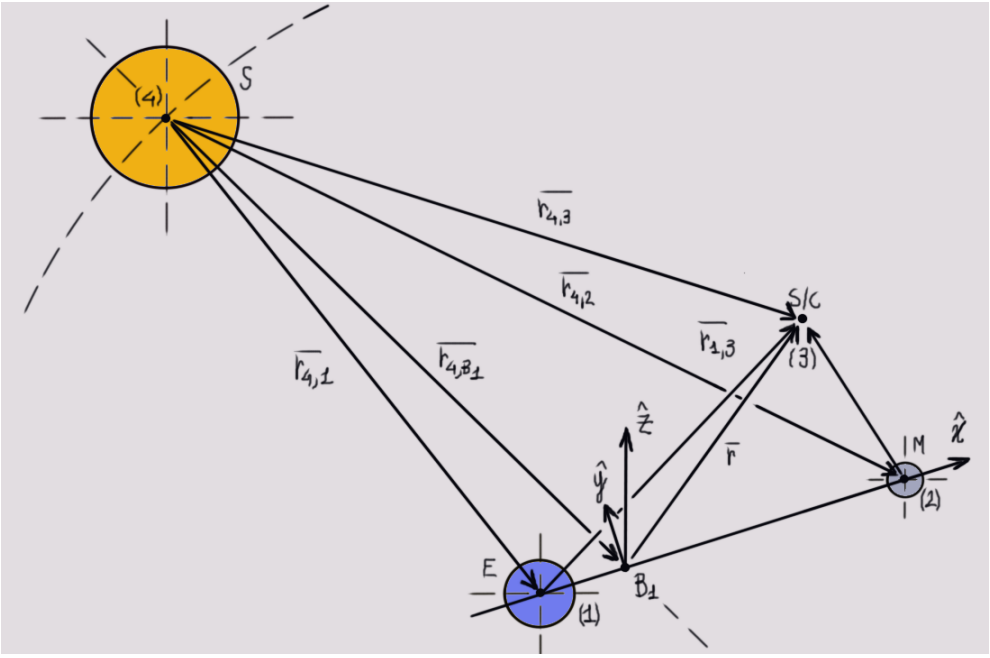

Figure 2.10: ***Radius vectors' schematization.***

a single model w.r.t. the Earth-Moon synodic reference frame. It's important to notice the second term associated to $\mathcal{U}^*$, which reflects the Sun-contribute, defined by the magnitude radius $\|r_S\|$, and its gravitational parameter μ^*:

$$\mu^* = \frac{M_S}{(M_T + M_L)} = \frac{M_S}{M^*} \qquad \rightarrow \qquad M_S = \mu^* M^* \tag{2.11}$$

The above-introduced modified potential function figures as:

$$\mathcal{U}^* = \mathcal{U} + \mathcal{U}_\odot = \left(\frac{1-\mu}{\|r_{13}\|} + \frac{\mu}{\|r_{23}\|} + \frac{x^2+y^2}{2} \right) + \epsilon \left[\frac{\mu^*}{\|r_{34}\|} - \frac{\mu^*}{\|r_S\|^3} \left(x_i x + y_i y + z_i z \right) \right] \tag{2.12}$$

in which the (x_i, y_i, z_i) components are relative to P_i's position (that of the sail). We'll denote as $\|r_{34}\|$ the radius vector magnitude in the opposite direction going from solar sail to Sun, hence opposite sense components' if paired to that used for the solar radiation pressure modeling:

$$\boldsymbol{r}_{34} = -\boldsymbol{r}_{43} = \left[-x + r_0 \cos(\theta), -y + r_0 \cos(\theta), +z \right] \tag{2.13}$$

$$\boldsymbol{r}_{B14} = -\boldsymbol{r}_S = \left[+r_0 \cos(\theta), +r_0 \cos(\theta), 0 \right] \tag{2.14}$$

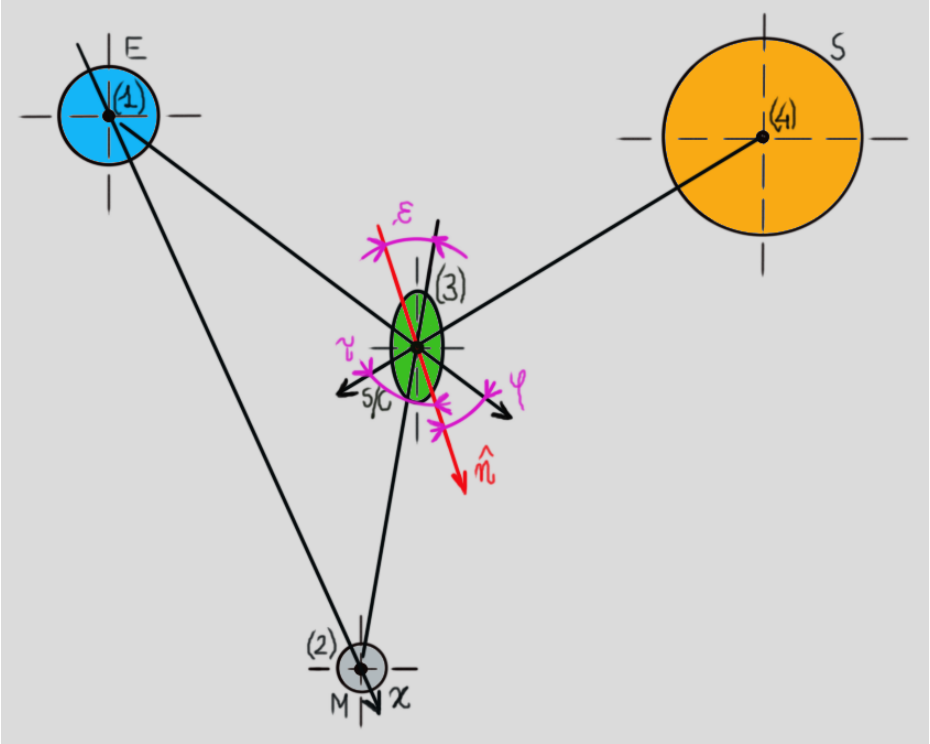

Figure 2.11: ***Radiation's hitting radius vectors and matching angles.***

These radius vectors have been defined by retrieving the relation-ship between accelerations and gravitational potentials.

$$\nabla \mathcal{U}_{\odot} = \left(\frac{\partial \mathcal{U}_{\odot}}{\partial x}, \frac{\partial \mathcal{U}_{\odot}}{\partial y}, \frac{\partial \mathcal{U}_{\odot}}{\partial z} \right) \tag{2.15}$$

$$\frac{\partial \mathcal{U}_{\odot}}{\partial x} = \epsilon \left(-\frac{\mu^*}{\|r_{34}\|^{\frac{3}{2}}} \left[x - r_0 \cos(\theta) \right] - \frac{\mu^*}{\|r_S\|^3} r_0 \cos(\theta) \right) \tag{2.16}$$

$$\frac{\partial \mathcal{U}_{\odot}}{\partial y} = \epsilon \left(-\frac{\mu^*}{\|r_{34}\|^{\frac{3}{2}}} \left[y - r_0 \cos(\theta) \right] - \frac{\mu^*}{\|r_S\|^3} r_0 \sin(\theta) \right) \tag{2.17}$$

$$\frac{\partial \mathcal{U}_{\odot}}{\partial z} = \epsilon \left(-\frac{\mu^* z}{\|r_{34}\|^{\frac{3}{2}}} \right) \tag{2.18}$$

Finally, the ϵ parameter is taken equal to 1 in order to take into account the expected solar-gravitational potential, hence if it was been assumed null, this would have meant analyzing classical *CR3BP* treatment.

2.2.1 $[\phi, \epsilon, \tau]$ Angles Description

We can identify as Ω our triad of space-time variation angles, as shown in **figure 2.11**:

$$\Omega = [\phi, \epsilon, \tau] \tag{2.19}$$

Taking as reference the index k, which stands for the k^{th} starting radius vector's point, in this case having $k = (1,2,4)$. The consequent analytical passages, regarding image shown in **figure 2.10**, would lead to:

$$\hat{n} \cdot \boldsymbol{r}_{k3} = \|n\| \|r_{k3}\| \cos(\Omega) \tag{2.20}$$

$$\hat{n} = \begin{bmatrix} \hat{n}_x \\ \hat{n}_y \\ \hat{n}_z \end{bmatrix} = \begin{bmatrix} \hat{n}\cos(\alpha) \\ \hat{n}\sin(\alpha)\cos(\delta) \\ \hat{n}\sin(\alpha)\sin(\delta) \end{bmatrix} \qquad \text{and} \qquad \boldsymbol{r}_{k3} = \begin{bmatrix} r_{k3}^x \\ r_{k3}^y \\ r_{k3}^z \end{bmatrix} \tag{2.21}$$

in which the three components r_{k3}^x, r_{k3}^y and r_{k3}^z depends on P_j position considered for the relative motion. At this time it was necessary to establish how these angles ϕ and ϵ could vary in time for learning the way these external radiations should hit the designing sail. For instance, as regarded and cited in **[35]**, to notice the existence of two distinguishable angles, α and δ, it's necessary to pair $\hat{n}$ components of solar sail's main axis of reference to those referred to radius vectors'. For instance, it's been initially decided to fix, both α and δ and trying to compute the previous set of equations of motions, concerning the *BCR4BP*, modifying only the 6 *IC*s for testing the solver's capability on drawing the external disturbances and avoiding to determine how the sail would adapt to them. On the grounds of the scalar product definition, these passages would let us to define the radiation pressure coupling to the sail's attitude by the presence of ϕ, ϵ and τ. By following the treatment above-discussed, the radiation pressure will vary to the sail's orbital achieved positions, thanks to this particular set of attitude angles.

2.3 Solar Radiation Pressure

One of the most important environmental effects is that of the photons exchanging their Moment of Momentum to the solar sail, whose electromagnetic properties may influence its time-space attitude and motion. Regarding discussion in **[16]**, we can specifically assign to this external disturbance the following mathematical definition:

$$\mathbf{F}_S = M_{S/C}\ddot{\mathbf{r}}_i = \beta G \frac{M_S M_{S/C}}{\|R_i\|^2} \left(\hat{n} \cdot \hat{R}_i\right)^2 \hat{n} \tag{2.22}$$

The required radius vector to describe all *SRP* summing effects are:

$$\boldsymbol{r}_{43} = [+x - r_0 \cos(\theta), +y - r_0 \cos(\theta), +z] \tag{2.23}$$

The general expression, as deeply described in **[36]**, relative to the *SRP* force is:

$$\ddot{\mathbf{r}}_{\odot} = \beta \frac{\mu^*}{\|r_{43}\|^2} \left(\hat{n} \cdot \hat{r}_{43}\right)^2 \hat{n} \tag{2.24}$$

β stands for the lightness factor, which is, as the reference example, index of the *SRP* effects to those of solar gravity, expressed as a dimensionless ratio. As usual, the lightness factor depends on the emitting solar radiation's luminosity $L_{\odot}$, its gravitational parameter $\mu_{\odot}$, the speed of light c, to the critical loading parameter σ^* and to an optical/structural property parameter called Q, depending on both chosen materials and optical reflecting properties.

$$\beta = \sigma^* \frac{A_d}{M_d} = \frac{L_{\odot} Q}{2\pi \mu_{\odot} c} \frac{A_d}{M_d} \tag{2.25}$$

The choice of Q may highlight the capability of the *SRP* to exchange efficiently the *MoM* to the application of a sail's control law. Moreover, it's been adopted a conservative approach by putting an higher value of Q, hence looking for an higher lightness parameter β for involved mission desinging parameters.

2.4 Terrestrial and Lunar Radiation Pressure

The involved process aims to establish in which way the radiation pressure reflected by Earth and Moon could modify the sail's motion and how to pair it to solar contribute, this to provide a better awareness of their intensities. These reflective contributes should take into account the medium surface-atmosphere properties of light, considering that it comes only from Sun and neglecting the Galactic Cosmic Rays *GCR* coming from the outside of Solar system. The initial *SRP*s should be associated to the Solar Particle Events *SPE*s due to solar-flares irradiated by the Sun's magnetic field. The required radius vectors for defining these planetary reflected accelerations hitting the solar sail can be written as:

$$\boldsymbol{r}_{42} = \begin{cases} [+x - r_0 \cos(\theta)] - (x + \mu - 1) = 1 - [\mu + r_0 \cos(\theta)] \\ [+y - r_0 \sin(\theta)] - y = -r_0 \sin(\theta) \\ +z - z = 0 \end{cases} \tag{2.26}$$

$$\boldsymbol{r}_{41} = \begin{cases} [+x - r_0 \cos(\theta)] - (x + \mu) = -[\mu + r_0 \cos(\theta)] \\ [+y - r_0 \sin(\theta)] - y = -r_0 \sin(\theta) \\ +z - z = 0 \end{cases} \tag{2.27}$$

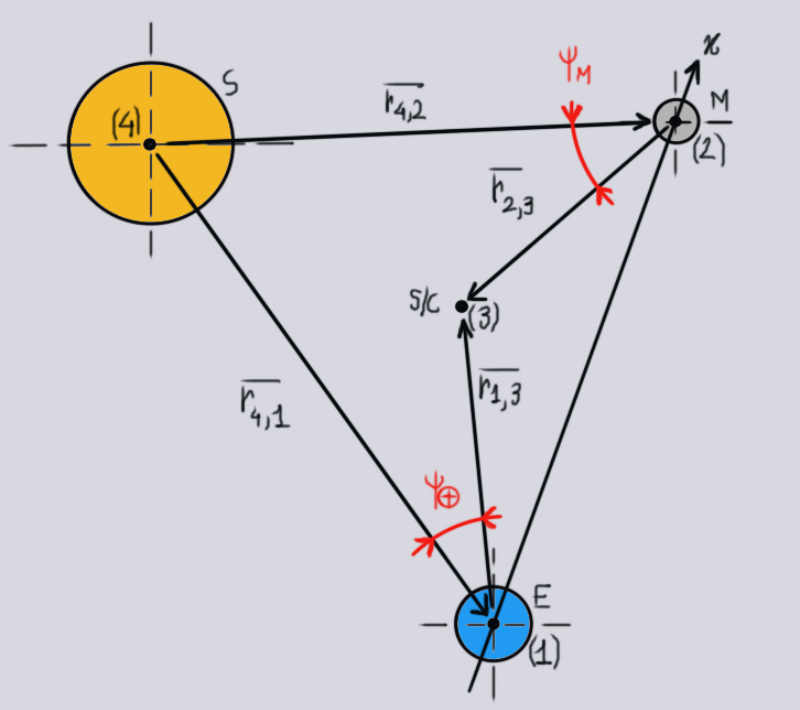

Figure 2.12: ***Albedo coupling angles.***

These set of radius vectors' components are used to establish the variable SRP w.r.t. AU distance from Sun.

$$\Delta_{S/E} = \frac{S_0}{\|r_{41}\|^2} \qquad \text{and} \qquad \Delta_{S/M} = \frac{S_0}{\|r_{42}\|^2} \tag{2.28}$$

$$\text{with} \qquad S_0 = 1367.5 \frac{W}{m^2} \tag{2.29}$$

S_0 stands for Solar Constant, whereas $\Delta_{S/E}$ and $\Delta_{S/M}$ the radiation variations brought by the Sun on Earth and Moon respectively. This treatment could be looked in [**37**], in which it was needed to establish the depending angular rate comprehended between two different radius vectors w.r.t. each of the primary bodies involved in the interaction. These ones should be $\boldsymbol{r}_{41}$ and $\boldsymbol{r}_{42}$, relatively distinguished to the $\boldsymbol{r}_{13}$ and $\boldsymbol{r}_{23}$ radius vectors respectively. By applying the usual dot-product, it could be possible to derive:

$$\boldsymbol{r}_{4t} \cdot \boldsymbol{r}_{t3} = \|r_{4t}\|\|r_{t3}\| \cos\Psi \quad \rightarrow \quad \Psi = [\Psi_M, \Psi_\oplus] \tag{2.30}$$

Moreover, to generalize as more this treatment, it's been assigned to 't' the meaning of both accelerations' contributes coming from Earth and Moon, concerning $t = [1,2]$.

Referring to [**38**], it's been found a general equation that states for the total energy brought up by reflected electromagnetic waves. It will depend on Ψ_i, the solar sail's distance h (which is equal to $\boldsymbol{r}_{t3}$, thereby depending on the primary body choice) to each of the primary bodies' *COM*, to the Albedo coefficients a_p, to the unit vectors $\boldsymbol{r}_{t3}$ and to **equation 2.19**. Below it's been shown the mathematical assessment of this treatment:

$$E_S\left(\Psi_i, h, \Omega, a_p\right) = \tag{2.31}$$

$$= \frac{A_i \Delta_{S/i}}{\left(R_i + r_{t3}\right)^2} \left\{ \frac{2a_p}{3\pi^2} \left[(\pi - \Psi_i)\cos(\Psi_i) + \sin(\Psi_i) \right] + \frac{1 - a_p}{4\pi} \right\} \hat{n} \quad \left[\frac{W}{m^2}\right] \tag{2.32}$$

We are interested to look for the accelerations that will be inserted in the Solar-sail orbital motion dynamics. As described in [**17**], it's possible to write the expression of albedo's p_R taking, as a known coefficient, the total energy $E_S\left(\Psi_i, h, \Omega, a_p\right)$ and dividing it by the speed of light c:

$$p_R = \frac{E_S}{c} \qquad \left[\frac{Kg}{ms^2}\right] \tag{2.33}$$

Applying the Newton's second law of dynamics it could be possible to obtain the accelerations' expression in a closed form as:

$$2p_R A_{SS} \left(\hat{r}_{t3} \cdot \hat{n}\right)^2 \hat{n} = M_{SS} a_i \qquad \rightarrow \qquad a_i = \frac{2p_R A_{SS}}{M_{SS}} \left(\hat{r}_{t3} \cdot \hat{n}\right)^2 \hat{n} \quad \left[\frac{m}{s^2}\right] \tag{2.34}$$

Angles Ψ_i denote several oscillating solutions depending on the sail's actual distance to each of the primary bodies. It's been already assumed, as for simplicity, accounting the two primary bodies a perfect spherical shape and a uniform solar radiation pressure hitting their inner and outer atmosphere layers. For simplicity, onto these models haven't been put eclipse conditions, which would be found whenever the Moon or Earth should be located in the mid-extension binding the Sun to the sail itself.

2.5 Radius-Mass Optimization Process

In this section the purpose is to verify, by adopting both analytical and numerical passages, which could be a possible optimized solar sail's radius and mass in two specific orbital planes, taken as the Sun-Earth and then the Earth-Moon one. For this latter solution there will be analyzed the path described by L_1^* and varying the lightness factor to retrieve the best suiting designing parameters needed for the active control system and deployment mechanism sizing.

2.5.1 Solar Sail Missions' Sizing Literature review

Results validation require an approach investigating upon several space missions' typical radius and masses concerning to deploy solar sails from CubeSats.

Space mission	***Class***	***Area*** $[m^2]$	***Mass*** $[Kg]$	$\boldsymbol{\beta}$ $[-]$
IKAROS	*Interplanetary Solar sail mission*	196	310.072	0.001
InflateSail	*3U CubeSat demonstr. in LEO orbit*	10	3.2	*N/A*
NanoSail-D2	*3U CubeSat demonstr. for sail's deploy*	10	4.2	0.004
COSMOS-1	*Earth's orbital Solar sail demonstrator*	600	100.2	0.009
LightSail-1	*3U CubeSat demonstr. for sail's deploy*	32	4.928	0.010
NEA Scout	*6U CubeSat demonstr. for sail's deploy*	86	12.04	0.011
SunJammer	*solar sail demonstrator in LEO*	1200	32.04	0.057
Halley's Comet	*Helio-gyro Solar sail demonstrator*	576000	4377.6	0.207
CubeSail	*3U CubeSat demonstr. for sail's deploy*	25	3	*N/A*
Lunar Flashlight	*6U CubeSat demonstr. for sail's deploy*	80	13.6	*N/A*

Table 2.1: ***Sail's typical masses and volumes, source [39] and [40]***

These lasts are enhancing human capabilities to give more comfortable and suitable solutions to higher technologies problems, in this case literally by launching more satellites at once, arranging them to the final orbital trajectory and then assembling

and deploying their stowed sails for obtaining a shading device. Historical space-missions provides several examples, **table 2.1**, at these purposes, both for huge and smaller deploying systems, whose generalities will be paired to optimized solutions found afterwords. Analyzing this researched data-set, CubeSat and solar sail's applications differ significantly in both areas and masses and these may highlight, as a consequence for it, the difficulty of launching bigger and heavier systems than smaller and lighter ones.

2.5.2 Planetary Sunshade Design in Sun-Earth Orbital Plane

The Planetary Sunshade has been initially discussed relatively to Sun-Earth orbital plane, imaging to place it in proximity of cis-solar gravitational equilibrium point L_1. This design concerns about to define both optimized orbital radius and mass needed by entire program to reflect radiation that would inevitably hit Earth, increasing *GHG* issues. For instance, this section pursues to introduce the mathematical modeling as starting approach to precursor mission preliminary sizing. Following the treatment given by state-of-art, the Sun-Earth modeling foresee to explain the existence of a designing parameter named *Terrestrial Insulation reduction* $\left(\frac{\partial Q}{Q}\right)$ normally addressed to Planetary Sunshade's radiation capability of reducing incoming radiation. It can be easily replaced by the generic change in flux $\left(\frac{\partial F}{F}\right)$ as imposing:

$$\frac{\partial Q}{Q} = \frac{\partial F}{F} = 1.75\% \tag{2.35}$$

It's been chosen this specific value, as delved in [**7**], based on climate-change mitigation solutions for reducing global increasing temperatures by the application of imagined Planetary Sunshade. By reducing the solar radiation hitting the Sun by this factor it can be denied the terrestrial over-heating effect and letting global temperatures to not stabilize over than 1.5°, as imposed by international climate conferences. It's necessary to define the optimum Area-to-Mass ratio for the time-cost estimation process, by taking as true the initial supposed and estimated CO_2 increasing pollutant assuming valid their actual concentrations levels. Mathematically speaking, $\frac{\partial Q}{Q}$ can be expressed equal to the fraction of two different solid angles: the first one is relative to that of the solar sail and the second to that of radiation pressure source, which is the Sun. As deeply described in [**41**], each of them contribute as:

$$d\Omega = \frac{d\Sigma \cdot \hat{u_r} \cdot \hat{u_n}}{r^2} = \frac{d\Sigma}{r^2} \tag{2.36}$$

Σ stands for the effective sail's oriented surface, whereas $\hat{u_r}$ and $\hat{u_n}$ the unit vectors for the radial and normal directions in space. Eventually, r the relative distance

between the sail's *COM* and the external radiation source. As described in [**42**], this framework yields:

$$\left(\frac{\partial Q}{Q}\right) = \frac{d\Omega_S}{d\Omega_\odot} = \frac{\pi R_S^2}{r_s^2}\frac{r_0^2}{\pi R_\odot^2} = \left(\frac{R_S}{R_\odot}\right)^2 \left(\frac{r_0}{r_s}\right)^2 \tag{2.37}$$

r_0 is the Astronomical unit AU, R_S the solar sail radius and $R_\odot$ the Sun radius.

$$\Rightarrow R_S = R_\odot \sqrt{\frac{\partial Q}{Q}}\frac{r_s}{r_0} \tag{2.38}$$

It's been taken a varying r_s upon an initial expected existence range, this to look for which could be the best coupling Area-to-Mass ratios. On the other side, accelerations a_s could be found by the energy conservation law, regarding $\omega_\oplus$ as the Earth's angular velocity w.r.t. the Sun and gravitational parameters $\mu_\odot$ and $\mu_\oplus$:

$$\omega_\oplus{}^2 (r_0 - r_s) + \frac{\mu_\odot}{(r_0 - r_s)^2} = a_s + \frac{\mu_\odot}{r_s^2} \qquad \text{with} \qquad \omega_\oplus = \sqrt{\frac{\mu_\oplus}{r_0^3}} \tag{2.39}$$

$$\Rightarrow a_s = \omega_\oplus{}^2 (r_0 - r_s) + \frac{\mu_\odot}{(r_0 - r_s)^2} - \frac{\mu_\odot}{r_s^2} \tag{2.40}$$

The generic expression for the solar sail's acceleration a_s, evaluated to shading disc's optical properties k and to the system's overall mass M_S, results to be:

$$a_s = \frac{2kP_E A_S}{M_S}\left(\frac{r_0}{r_0 - r_s}\right)^2 \qquad \text{with} \qquad P_E = \frac{I}{c} = \frac{\Delta_S}{c}\left(\frac{r_0}{r_0 - r_s}\right)^2 \tag{2.41}$$

in which this expression pair together the solar sail area A_S, its mass M_S and radiation pressure P_E. Δ_S would be equal to 1367.5 $\frac{W}{m^2}$, taken as the mean incident flux hitting Earth paired to dimensionless AU^2. Sail's optical constraints, that figure in k, have been thought imaging to assure a perfectly reflective surface.

$$\Rightarrow R_S = \left(\frac{r_0 - r_s}{r_0}\right)\sqrt{\frac{a_s M_S}{2\pi k P_E}} \tag{2.42}$$

The solar sail's Radius R_S will be given by the chosen Mass M_S and to the previous varying r_s:

$$\Rightarrow M_S = \frac{2\pi k P_E}{a_S} R_\odot^2 \left(\frac{r_s}{r_0 - r_s}\right)^2 \left(\frac{\partial Q}{Q}\right) \tag{2.43}$$

In figure **figure 2.13**, it's been demonstrated a chart showing, at first, a decreasing and finally an increasing Mass, if paired to r_s going out from the Earth and

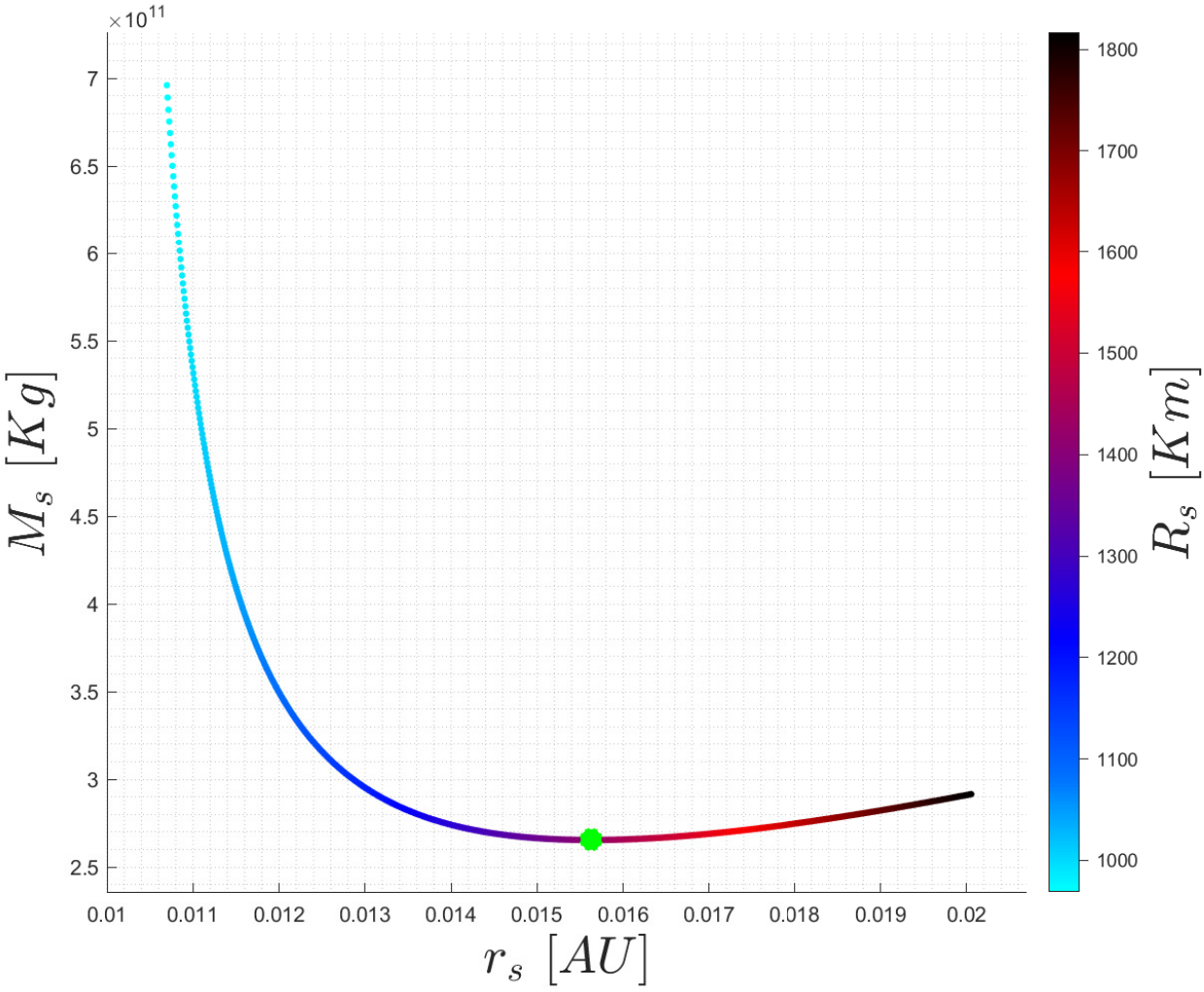

Figure 2.13: ***Radius-Mass optimizing chart.***

connecting both the primary bodies in the gravitational interaction. Final solutions could be summarized as:

$$\begin{cases} M_{S_{opt}} = 2.67 \cdot 10^{11} \quad [Kg] \\ R_{S_{opt}} = 1419.14 \quad [Km] \\ r_{s_{opt}} = 2.34 \cdot 10^{6} \quad [Km] \end{cases} \tag{2.44}$$

2.5.3 Precursor Mission in Earth-Moon Orbital Plane

In the Earth-Moon orbital plane context, the condition $\boldsymbol{a} = -\nabla\mathcal{U}^*$ is introduced into **equations 2.8** whenever doing a qualitative analysis of photo-gravitational instantaneous points, **subsection 2.1.1**. L_1^* has been analyzed for the Earth-Moon orbital plane by solving a system of three, time-varying, non-linear equations and adapting them w.r.t. sail's typical lightness factors and sizing features taken from **table 2.1** and **2.2**. This system is solved using *"fsolve"* and choosing as initial

Feature	**3U**	**6U**	**12U**
Total mass $[Kg]$	$3.5 \div 8$ *typical: 4*	$12 \div 17$ *typical: 14*	*typical: 25*
Payload mass $[Kg]$	$1 \div 4$ *typical: 2.5*	$5 \div 12$ *typical: 6*	$11 \div 13$ *typical: 12*
Payload volume $[U]$	$1 \div 2$ *typical: 1.5*	$2.5 \div 5$ *typical: 3*	*typical: 10*

Table 2.2: ***CubeSat sizing categories [43].***

iteration condition $b_0 = [0.8363,0,0]$, hence the exact estimated position of L_1 for speeding up numerical simulation, expecting to look for solutions close to it. The final solar sail's orbital radius is found as re-adapting **equation 2.38** and writing it as:

$$r_S = R_M \frac{r_0 - \bar{x}}{r_0} \sqrt{\frac{\partial Q}{Q}} \tag{2.45}$$

in which $\bar{x}$ stands for the mean distance of x found by the propagation cycle w.r.t. Earth's COM, $r_0 = AU$, R_M the Moon radius and $\frac{\partial Q}{Q}$ taken as that one seen for Sun-Earth modeling. Imaging to take the deployed sail as circular-shape, the consequent mass will be found from **equation 2.25**:

$$M_S = \sigma^* \frac{A_S}{\beta} \tag{2.46}$$

It was expected to find an approximation trend similar to that found in Sun-Earth modeling. This couldn't be achieved for limited radius and masses inserted into numerical simulations because strictly depending on both literature analysis and actual technological developments, whose typical ranges could be found by bibliography **table 2.1** and **2.2**. This technique could let to obtain the sail's optimized

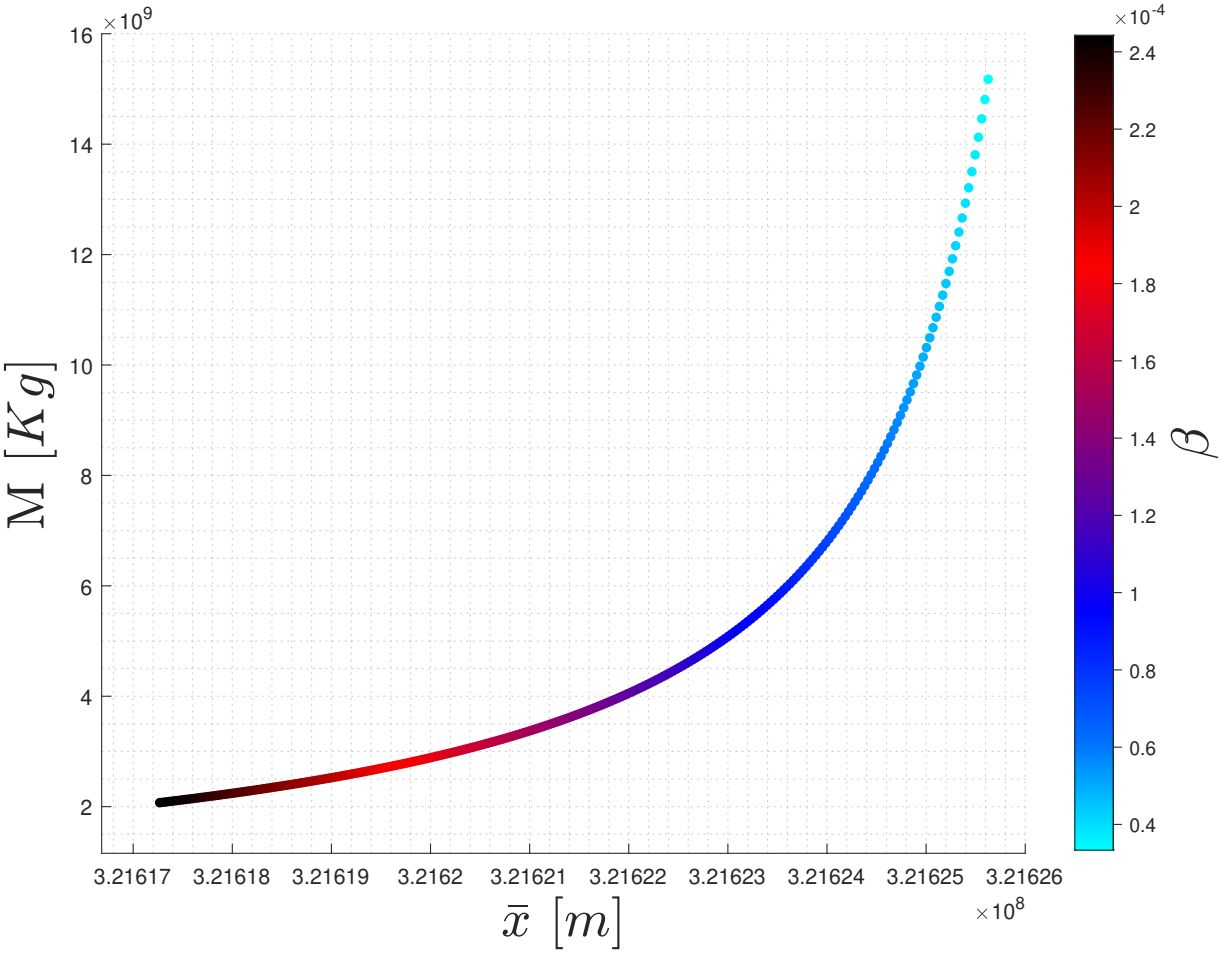

Figure 2.14: ***β-Mass optimizing chart.***

radius, mass and lightness factor by simply using a *"colormap"* putting into evidence L_1^* w.r.t. β. It could be observed that L_1^* would always describe closed paths on the xy orbital plane, providing null contributes upon z-axis, despite there would exist an asymmetric distribution for x and a symmetric one for y. This could be derived from *BCR4BP* adopted architecture in which Mass differences, relatively to primary bodies, may attract the solar sail mainly to positive x, whereas this doesn't affect those upon y-axis.

These last would be characterized by symmetric radius vectors between the solar sail and primary bodies in synodic reference frame, hence allowing a certain symmetric behavior. Mass differences would highlight 1-period symmetric instantaneous L_1^*

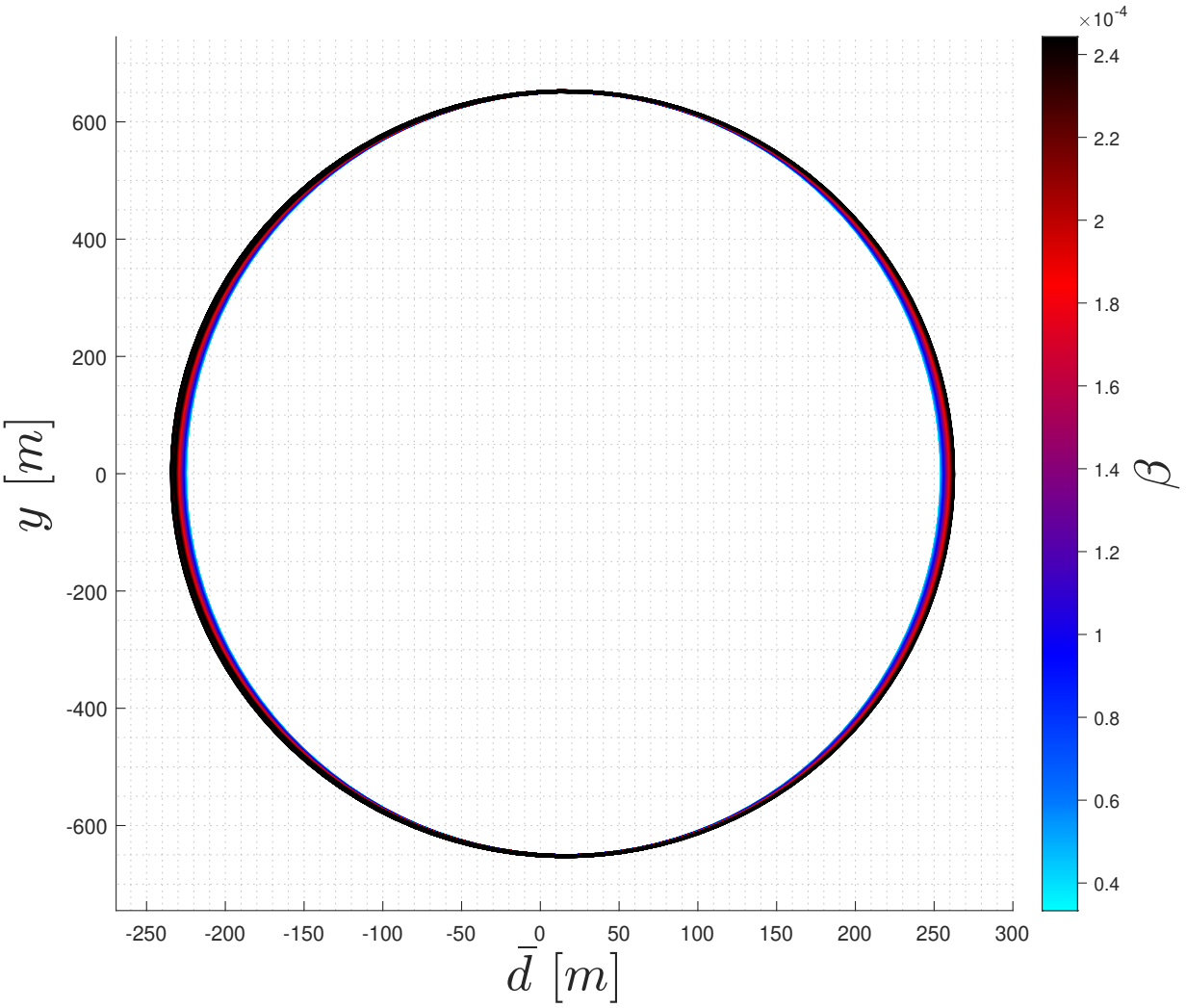

Figure 2.15: ***Instantaneous*** L_1^* ***points w.r.t*** L_1**.**

points instead of choosing an half-one. This is due to masses concerning both Earth and Moon, going to influence differently the solar sail itself. The best fitting lightness factor will be that associated to lowest sail's mass values, observing that when the first of these increase, the second would decrease and vice versa.

It's well observable how both x and y-axis oscillate between positive and negative values, with kind-regard to $\bar{d} = x - \bar{x}$, in which x stands for L_1^* dummy positions.

Moreover, these results have been found by fixing the sail's cone angles α equal to 0° and +180° respectively when assuming to put the Sun in opposition to the Moon and then next to it, hence when expected to have minimum and maximum shading conditions, this to let δ's choice negligible.

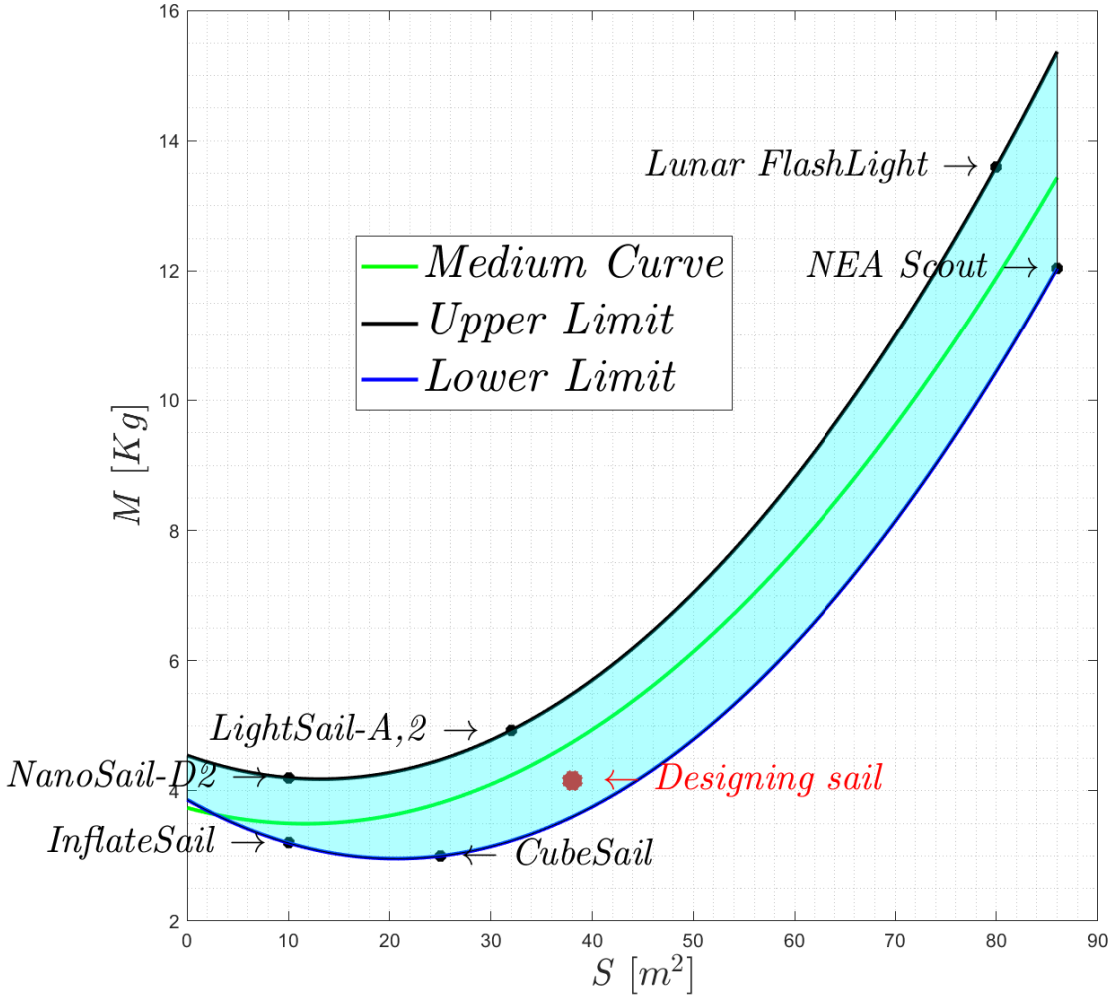

Figure 2.16: ***Cloud of points for several led space-missions.***

Precursor mission design regards taking into account β_{opt}, $r_{S_{opt}}$ and $m_{S_{opt}}$, which deeply depend on actual technological limitations. Its preliminary sizing is given by choosing $\frac{\partial Q}{Q} = 1.498 \cdot 10^{-8}\%$, to look for suitable radius-mass couplings, finally approved by drawing a Validation-map chart able to group literature solar sail

missions to that designed in this project.

$$\begin{cases} \beta_{opt} = 0.00024 \\ r_{S_{opt}} = 3.48 \quad [m] \quad \rightarrow \quad A_{S_{opt}} = \pi r_{S_{opt}}^2 = 38.046 \quad [m^2] \\ m_{S_{opt}} = 4.16 \quad [Kg] \end{cases} \tag{2.47}$$

This preliminary sizing reflects how the solar sail would belong to a typical *3U* Cubesat platform, **table 2.2**, on the grounds of total masses reached for involved process. Payload masses and volumes will be served as an additional step for structural deployments and actuation devices' sizing.

Eventually, as anticipated just before, it's been depicted a validation map, **figure 2.16**, in order to grant a preliminary effectiveness of designed parameters. The cyan depicted region reflects the most common and acceptable combinations between deployed surface and Mass ranges used for solar sailing missions, the red-bolded point stands for the optimized solution just found in **solutions 2.47**, whereas black-ones to leaded space-missions.

The interpolation of these catalog-points is achieved by adopting a quadratic approximation and putting into evidence the highest and lowest black and blue-bold curves, ideally identifying the best fitting region selectable in the chart. Drawing the validation-map, system's design will satisfy it close to lower-bold curve, hence it would be necessary to reduce only the deploying surface and maintaining the same Mass, or keeping the same surface but increasing the overall mass, this to let the project-point closer to the green-medium approximation.

Moreover, the designing lightness factor β reflects the common values in **table 2.1** and, as an operative decision, that chart doesn't consider the presence of bigger systems like *SunJammer* and *COSMOS-1* space missions, to focus only on *LightSail* applications. Whenever it was decided to put them inside the same chart, the green-interpolating curve may differ significantly, bringing to a worse distinguishable cloud of points, justifying the operative choice for avoiding them.

2.5.4 Solar Sail's Shadow Cone

Eventually, this section may complete concerning the evaluation of projected shadow cones, obtained imaging the precursor mission being able to reflect a portion of radiation, analyzing covered cone's heights through geometrical considerations.

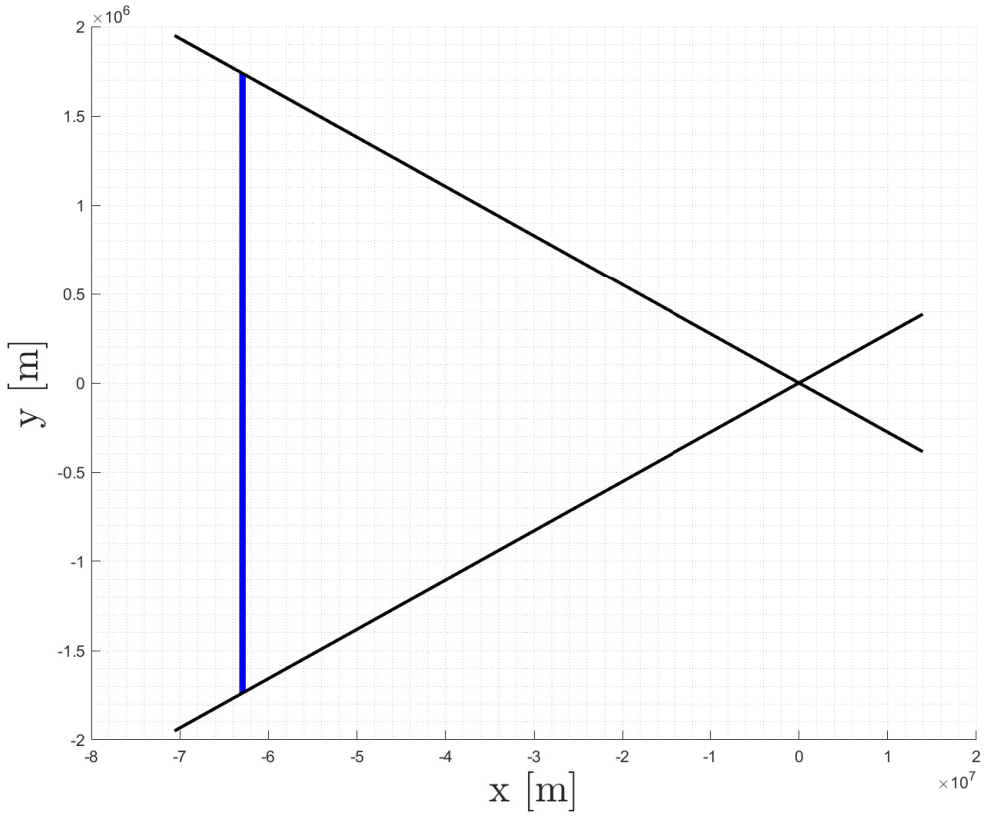

Figure 2.17: ***Tangent lines connecting the Moon to the solar sail.***

Moreover, it's assumed to take the sizing parameter $r_{S_{opt}}$ as valid and studying consequent shadows w.r.t. $\bar{d} = [0, -234.5, +262.68]\ m$. These $\bar{d}$ values are chosen from instantaneous L_1^* points on x-axis, standing for their mean, lowest and highest achieved values respectively. The code executes all needed radius vectors granting the tangent condition between the solar sail and the Moon.
For instance, it's necessary to solve a system concerning the Moon second-order circumference equation and generic tangent straight-lines passing through solar sail's border points, whose coordinates are defined as $\left(0, \pm r_{S_{opt}}\right)$. Final tangent straight-lines are referenced w.r.t. cislunar L_1 position, **figure 2.17**. The required

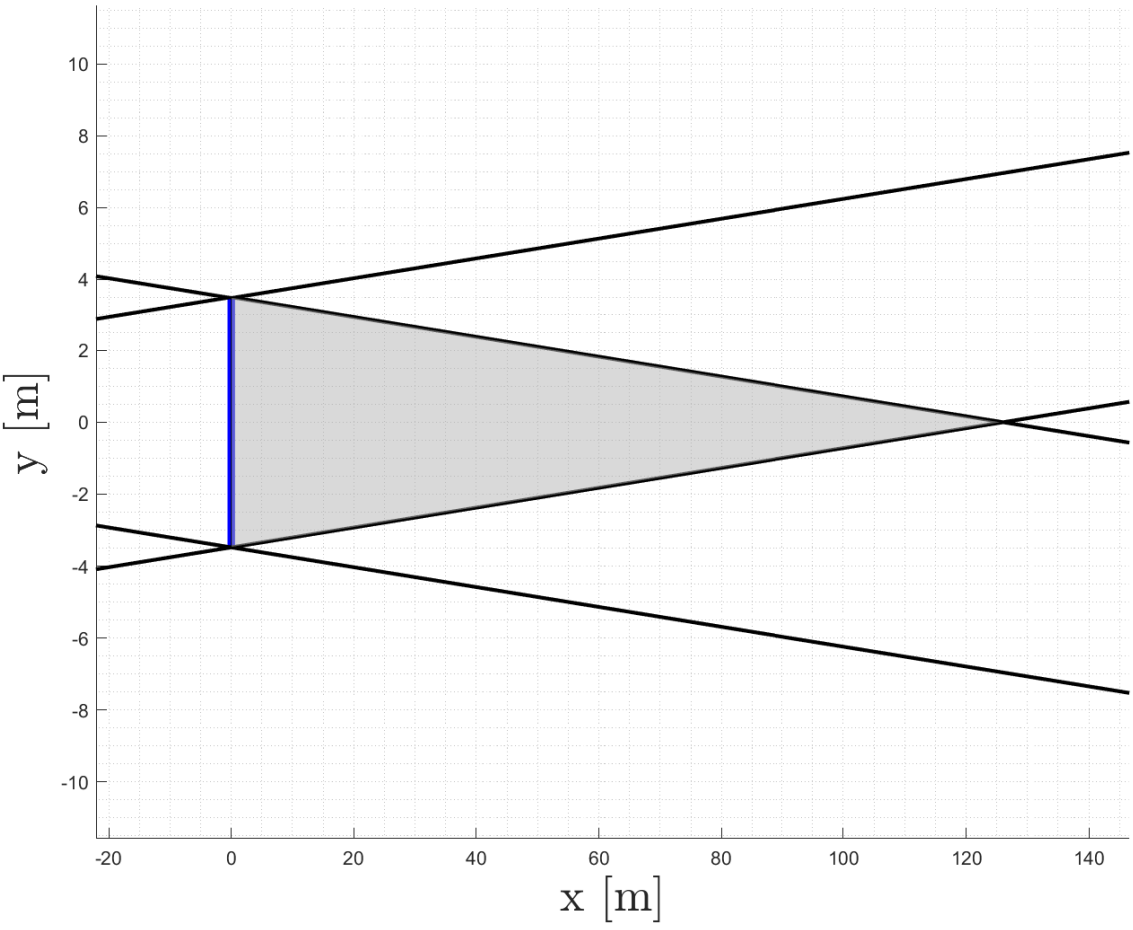

Figure 2.18: ***Shadow cone relative to*** $\bar{d} = 0$***.***

condition to be mathematically applied, after have substituted the generic straight-line equation inside the circumference one, is:

$$\begin{cases} x^2 + y^2 = R_M^2 \\ y = m\left[x - (1 - x_{L_1})\right] \pm r_{S_{opt}} \end{cases} \tag{2.48}$$

$$\Delta = 0 \tag{2.49}$$

with m standing for straight-line generic angular coefficient. $\Delta = 0$ represents the tangent condition to be applied to solve second order equation in x to find $\pm m$. Both blue-colored Vertical segments illustrates the Moon and the solar sail depicted along the xy orbital plane. From delved analysis, the height of shadow cones related

to $\bar{d} = 0$, **figure 2.18**, is approximately 125.6 meters. When $\bar{d} = -234.5$ meters, the shadow cone height reduces by 22 cm, while for $\bar{d} = 262.68$ meters, there is an increase of 30 cm. Based on preliminary analysis, the vertex angle between radius vectors, both tangent to the Moon, is approximately 3.98°.

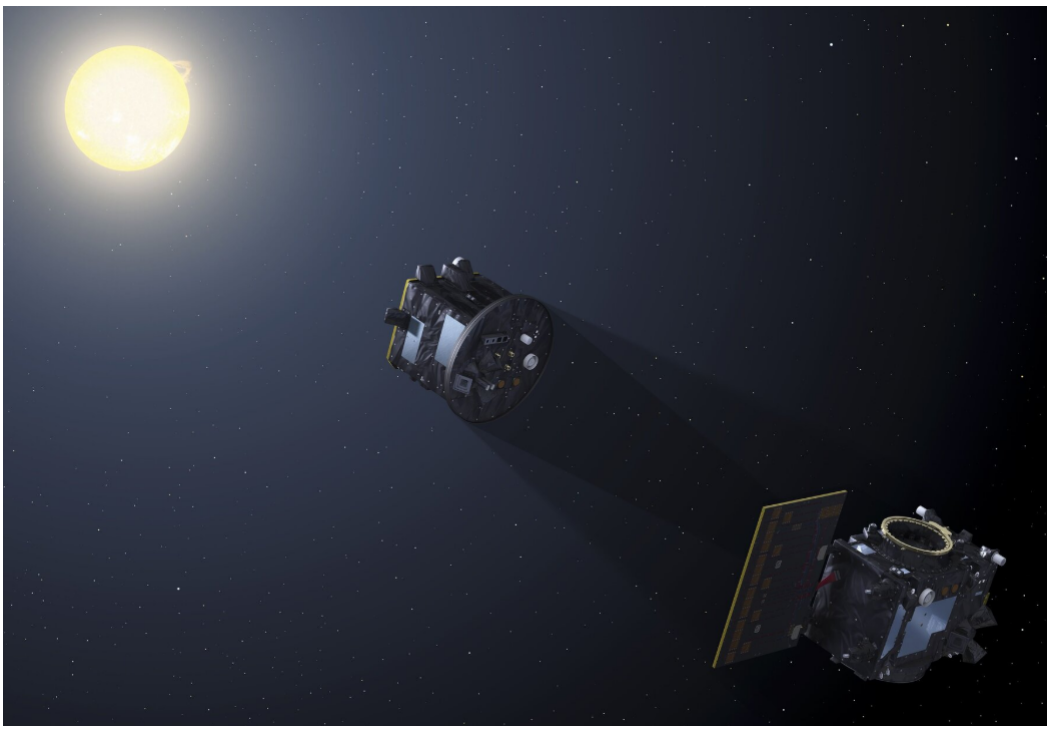

Figure 2.19: ***PROBA-3 space mission, source [44].***

In addition, it can be useful to compare the shadow cones' height generated in this precursor mission to that designed in other space missions to evaluate the reliability of the results for upcoming mission phases. As support to acquired analysis, *PROBA-3* space-mission, [**44**] and [**45**], intends to position two satellites, *Occulter* and *Coronagraph* in the Sun-Earth orbital plane, separated by a distance of 150 meters, to produce an artificial solar eclipse. Achieved shadow cones from designed precursor mission appear acceptable if paired to that of *PROBA-3* one, despite its positioning in a different orbital plane. As conclusion, these analysis put the fundamentals as proceeding to discuss about internal subsystems, in particular the deployment mechanism, whose assembly requires the knowledge of solar sail's treated sizing.

Chapter 3

Attitude Control System

The attitude and orbital motion of the sail are explored by selecting appropriate initial conditions *IC*s and boundary conditions *BC*s for active stabilization techniques. This approach enables an analysis of how the sail adjusts its configuration in response to external disturbances, leveraging optimized sizing solutions from precursor mission studies **subsection 2.47**.

The following section provides a comprehensive overview of the Attitude Control System *ACS*, focusing on solar radiation pressure and ideal control devices required to manage the solar sail's orientation. Additionally, the sail's performance will be evaluated by simulating several periodic orbits and choosing the best fitting to mission's design scenario.

This process involves assessing effects of external disturbances, such as solar radiation pressure and gravitational forces, to achieve the solar sail's optimal control over time. Furthermore, the mission analysis will evaluate the system's robustness by accounting for both torques and forces acting on the sail, whose sizing orders will be significant to delve on deployment phase.

3.1 Attitude Control Techniques

The primary focus of *ACS* design is to learn both the solar sail arrangement to solar radiation pressure and the development of a control algorithm capable of positioning the sail near L_1^*. The first involves to solve one non-linear equation derived from Bi-Circular Restricted Four-Body Problem framework, allowing for an analysis of how the sail's attitude angles α and δ respond to acting external forces. The second propose to study the sail's attitude stabilization and, approaching the method described in [**46**] and [**47**], it's necessary to establish which could be the ideal control to be applied by actuation devices for granting the correct solar sail's attitude w.r.t. α and δ. The attitude control law can be divided into two different approaches:

- The ***radiation pressure control law*** proposes to analyze in which way the solar radiation pressure may interact with the solar sail to adapt this last's cone and clock angles. Therefore, by introducing a technique being able to solve the resulting non-linear equation $\mathcal{F}_1^*$, the solver will execute it for different kind of periodical orbital motions. The just announced law reclaims only an attitude dynamic control without considering an on-board software, whose primary effect would be that of using actuators for feedback-control applications. On this grounds, this first approach focuses on analyzing in which way an ideal controller may work to control the solar sail's attitude w.r.t. external radiation pressure.

$$\mathcal{F}_1^* \quad \rightarrow \quad \sin^2(\alpha)\cos^4(\tau) = \frac{\|r_{43}\|^4}{(\beta\mu^*)^2}\left[a_y^2(t) + a_z^2(t)\right] \tag{3.1}$$

- The ***actuation devices control law*** approach proposes to develop an on-board software looking for ideal attitude angles by imposing different feedback controllers. Moreover, this approach needs a sophisticate software for respecting the imagined system's final conditions, activating the actuation devices provided by reasonable Volume and performances' numerical designing choices. These lasts depend not only on masses and geometries, but also on sail's actual and desired-state. The consequent command-action need to be analyzed by both kinematics and dynamic equations of motion, obtaining the system's response, referable as the solar sail's actual-state.

3.2 Radiation Pressure Attitude Control

The purpose of this section is to define the mathematical modeling at the core of the sail's active stabilization. By following the first approach introduced before, the problem statement will be framed within the Boundary Value Problem *BVP* analysis, where the method involves using *bvp4c* only to the first differential equation in x by adopting the *BCR4BP*. Specifically, equations in the y and z will be replaced by trigonometric expressions in *sine* and *cosine*. These periodic functions correspond to four different classes of *HALO* orbits [**36**], whose fundamentals are explained in **subsection 1.3**. Boundary Conditions *BC*s play a crucial role in determining the types of solutions that can be obtained. In this case, the objective is to develop a numerical model able to identify a periodic path confined within boundaries located between Earth and Moon. These *BC*s are set for both positions and velocities as imposing the following periodicity conditions onto x-axis:

$$\begin{cases} x(t_i) = x(t_i + T) \\ \dot{x}(t_i) = \dot{x}(t_i + T) \end{cases} \tag{3.2}$$

These would allow the system to explore orbits given by these exact constraints. Required initial conditions *IC*s b_0, needed for the *BVP*'s initial setting, are written as $[x_{L_1}, 0]$, with $x_{L_1} = 0.836$, imaging to look for periodical solutions close to L_1, where it's needed as the starting point for system's numerical integration. Moreover, the vector's mesh *"xmesh"*, needed by *bvp4c* to define the numerical time-working domain, has been defined between $t_i = 0 \div T$ and characterized by 13,000 points, with relative and absolute tolerances both imposed to 10^{-13}, as [**36**]. In this case T would be equal to $\frac{2\pi}{\omega_\odot}$, with dimensionless Sun's angular velocity $\omega_\odot$ mathematically obtained following the *BCR4BP* approach. The periodic path could be only attempted as inserting this specific $\omega_\odot$ to execute the numerical method, regarding that the Sun will last T to describe a complete rotation around the synodic reference frame center position $\mathcal{B}_1$. The Boundary Value Problem *BVP* supports the development of differential equations, crucial in applied mathematics and physics. Its fundamentals begin from the 18^{th} century with contributions from mathematicians like *Leonhard Euler* and *Joseph-Louis Lagrange*, who studied solutions in mechanics and fluid dynamics. The ***Boundary Value Problem*** formulation results being key to this process, as it requires solving the solar sail's trajectory under several constraints. The aim is to match initial/final positions and velocities in such a way that the resulting orbit is stable and repeats itself continuously over time. The inclusion of trigonometric expressions for y and z accelerations allows the model to incorporate the inherent periodic nature of *HALO* orbits, which are essential for maintaining the system in a stable trajectory between Earth and Moon and close to L_1, demonstrating how Boundary Value Problems are applied to complex space dynamics.

3.2.1 Solar Radiation Pressure Control Law

The procedure aims to look for an expression of α and δ in function of the solar radiation pressure for granting periodic trajectories by specifying y and z-axis trend through trigonometric functions. Moreover, it's necessary to establish, at each time-instance, external accelerations' $a_y(t)$ and $a_z(t)$, found from **equations 2.8**, and then solving leaded obtained non-linear equation [**36**]. As introduced at first, it's necessary to recall the most general expressions of external accelerations, yielding:

$$a_x(t) = \beta \frac{\mu^*}{\|r_{43}\|^2} \left(\hat{n} \cdot \hat{r}_{43}\right)^2 \hat{n}_x = \beta \frac{\mu^*}{\|r_{43}\|^2} \cos(\tau)^2 \cos(\alpha) \tag{3.3}$$

$$a_y(t) = \beta \frac{\mu^*}{\|r_{43}\|^2} \left(\hat{n} \cdot \hat{r}_{43}\right)^2 \hat{n}_y = \beta \frac{\mu^*}{\|r_{43}\|^2} \cos(\tau)^2 \sin(\alpha) \cos(\delta) \tag{3.4}$$

$$a_z(t) = \beta \frac{\mu^*}{\|r_{43}\|^2} \left(\hat{n} \cdot \hat{r}_{43}\right)^2 \hat{n}_z = \beta \frac{\mu^*}{\|r_{43}\|^2} \cos(\tau)^2 \sin(\alpha) \sin(\delta) \tag{3.5}$$

By dividing $a_z(t)$ to $a_y(t)$, it could be possible to look for δ variations:

$$\frac{a_z(t)}{a_y(t)} = \left(\frac{\sin(\delta)}{\cos(\delta)}\right) \tag{3.6}$$

$$\delta = \arctan\left(\frac{a_z(t)}{a_y(t)}\right) \tag{3.7}$$

The general expressions of α and δ could be derived as yielded:

$$\mathcal{A} = \left(\frac{r_{43_x}}{r_{43}}\right) \qquad \text{and} \qquad \mathcal{B} = \left(\frac{r_{43_y}}{r_{43}} \cos(\delta) + \frac{r_{43_z}}{r_{43}} \sin(\delta)\right) \tag{3.8}$$

$$\begin{aligned} \cos(\tau) = \frac{\hat{n}_x r_{43_x}}{\|r_{43}\|} + \frac{\hat{n}_y r_{43_y}}{\|r_{43}\|} + \frac{\hat{n}_z r_{43_z}}{\|r_{43}\|} = \left(\frac{r_{43_x}}{r_{43}}\right) \cos(\alpha) + \\ + \left(\frac{r_{43_y}}{r_{43}} \cos(\delta) + \frac{r_{43_z}}{r_{43}} \sin(\delta)\right) \sin(\alpha) = \mathcal{A} \cos(\alpha) + \mathcal{B} \sin(\alpha) \end{aligned} \tag{3.9}$$

$$a_y(t) \quad \rightarrow \quad \cos(\delta) = \frac{\|r_{43}\|^2}{\beta \mu^*} \frac{a_y(t)}{\sin(\alpha) \cos^2(\tau)} \tag{3.10}$$

$$a_z(t) \quad \rightarrow \quad \sin(\delta) = \frac{\|r_{43}\|^2}{\beta \mu^*} \frac{a_z(t)}{\sin(\alpha) \cos^2(\tau)} \tag{3.11}$$

$$\sin^2(\delta) + \cos^2(\delta) = 1 \qquad \rightarrow \qquad \frac{\|r_{43}\|^4}{\left(\beta \mu^*\right)^2} \frac{1}{\sin^2(\alpha) \cos^4(\tau)} \left[a_y^2(t) + a_z^2(t)\right] = 1 \tag{3.12}$$

This non-linear equation specify the dependency of two different contributes: the first is the usual squared-sine of α, whereas τ by its fourth-cosine one.

The higher complexity is carried-out by this last's term, once characterized by multiple trigonometric functions paired one another. It's necessary to solve $\mathcal{F}_1^*$ by isolating attitude angles and then solving them numerically.

$$\mathcal{F}_1^* \qquad \Rightarrow \qquad \sin^2(\alpha)\cos^4(\tau) = \frac{\|r_{43}\|^4}{(\beta\mu^*)^2}\left[a_y^2(t) + a_z^2(t)\right] \tag{3.13}$$

Numerical method has been thought by solving first **equation 3.7** and then **3.13** through *"fzero" MATLAB* function to find δ and α respectively, choosing as initial guess $x_0 = 0$ because looking for cone angles varying around $0°$.

3.2.2 Mission Trajectory Design

The mission scenario is focused on applying a periodic trajectory upon the Earth-Moon conjunction-line and coincident to x-axis. On this way, one reasonable choice is given by the following set of equations:

$$\begin{cases} y(t) = 0 \\ z(t) = 0 \end{cases} \tag{3.14}$$

The main purpose of trajectory design to assure the solar sail could remain in proximity to L_1 and verifying attitude angles may grant the x-motion respecting all previously defined boundary conditions. It's imagined to address it as a *"linear path"* fixing y and z-axis imposed at each time instance, **figure 3.1a**.

Cone angles exhibit an alternate behavior, describing periodic oscillations between $-7.4° \div +18.3°$. This attitude angle is that one actuation devices would need to apply to keep the solar sail aligned to the Sun. It is evident that applying needed variations in α at each time instance t_i would pose quite significant challenges to these devices to let the solar sail being properly controlled. Based on the approximate trend of α, a totally different behavior can be inferred for δ, whose solutions remain distinct and periodic.

From *BCR4BP* modeling and regarding the Sun's distinguished motion around the solar sail, it's possible to discuss cone angles' trend for all four Cartesian quadrants (recognizable once imaging the solar sail from an higher point of view). It's demonstrated to have positive α for the second and third quadrant, whereas negative for the last two remaining. For the first two, x-axis is always directed to the Moon and the solar sail describes positive α rotations around $+z$. This means that the solar sail need to assume a counterclockwise orientation w.r.t. z-axis to align its unit vector $\hat{n}$ to $\boldsymbol{r}_{43}$, and finally bringing the system aligning to the Sun. The opposite happens to the first and fourth quadrants, in which the solar sail may

rotate negatively describing a clockwise rotation w.r.t. $+z$-axis, **figure 3.1b**.

What about clock angles δ, these oscillates between $0°$ and $+180°$, and vice versa, throughout the entire orbital period T. Physically, this represents the solar sail continuously adjusting its attitude, with the y-axis oscillating between positive and negative orientations within the Earth-Moon orbital plane. Moreover, the z-axis alternates from an upward to downward orientation, and vice versa, to complete the orthonormal body-axis triad. Consequently, the range of values for δ can be interpreted as the sail tilting to always form a supplementary angle, **figure 3.2a**.

Finally, τ angles comprehended between $\boldsymbol{r}_{43}$ and the solar sail's unit vector $\hat{n}$ are analyzed. Their general trend looks periodic upon T, whereas are noticeable differences located in proximity to both α and δ variations approximately comprehended in $t_i = 149 \div 161$ and $t_i = 496 \div 507$ hours. Angle τ exhibits both left and right shifted trends depending on attitude angles' variations, **figure 3.2b**. As imagined, its working co-domain ranges in $0° \div +90°$, similar to a symmetric *"Sawtooth pattern"* repeating regularly at each half-period.

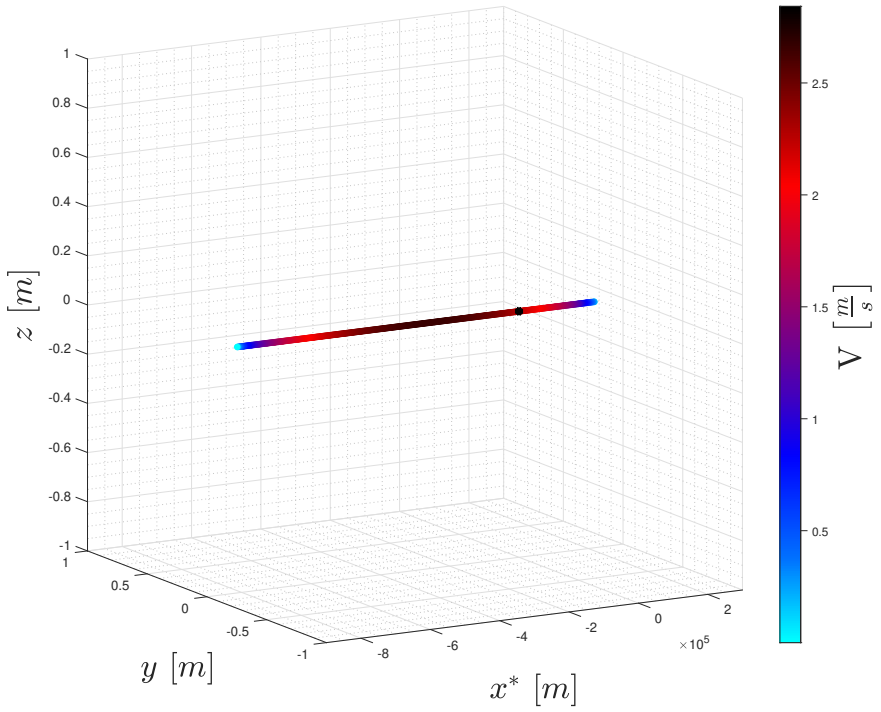

(a) ***Orbital trajectory.***

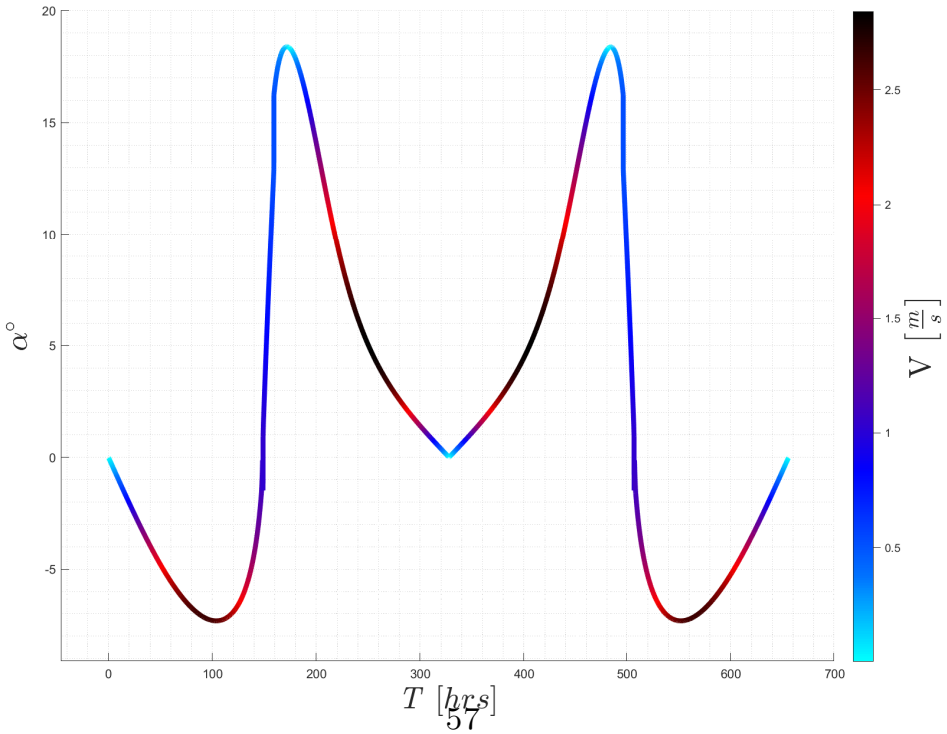

(b) ***Cone angles*** α***.***

Figure 3.1: ***Orbital trajectory and cone angle*** α***.***

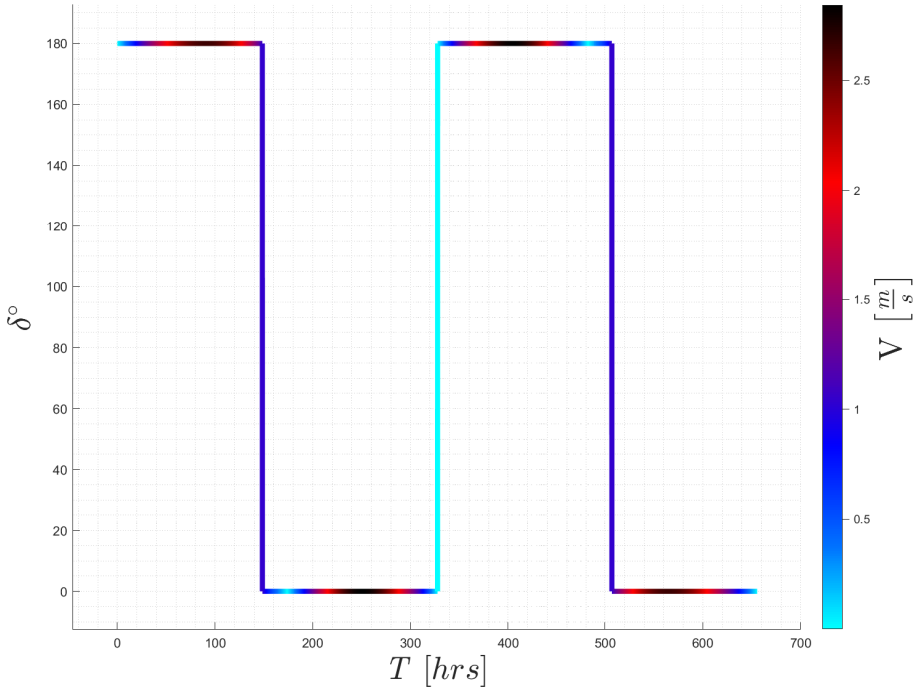

(a) ***Clock angles*** δ**.**

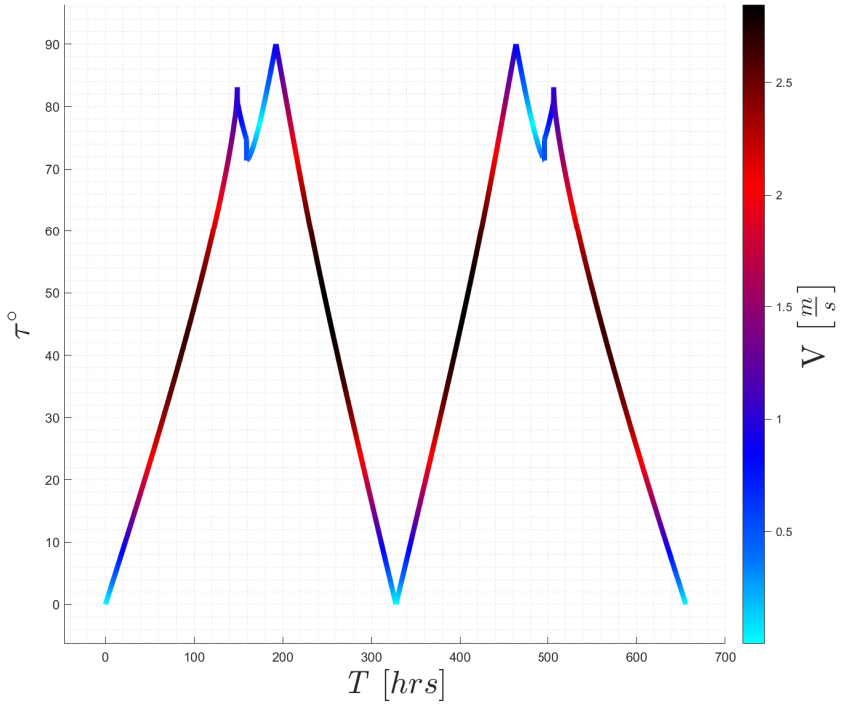

(b) τ ***angles.***

Figure 3.2: ***Clock angle*** δ ***and*** τ**.**

3.2.3 *HALO* Families Equations of Dynamics

In addition to proposed mission trajectory design, this project aims to discuss different trajectories referred to Planetary Sunshade modeling, this to describe both solar sail's periodic path and attitude angles around L_1. Referring to *HALO* families, delved in [**36**], these are considered inside the Earth-Moon orbital plane and can be divides as:

- The ***first HALO's family***, granting an *"horizontal-coverage"*, could be written as:
$$\begin{cases} y(t) = \mathcal{A}_y \sin(\omega t) = \sqrt{r^2 - \mathcal{A}_z^2}\sin(\omega t) \\ z(t) = \mathcal{A}_z \quad [-r, +r] \end{cases} \tag{3.15}$$
We'll denote as $\mathcal{A}_z$ the $\mathcal{Z}$*-quote family index*. All calculations foresee to put $A_z = 0$, thereby considering the intermediate case suggesting this family class.

- The ***second HALOs' family***, granting the *"vertical coverage"*, can be written as:
$$\begin{cases} y(t) = \mathcal{A}_y \quad [-r, +r] \\ z(t) = \mathcal{A}_z \sin(\omega t) = \sqrt{r^2 - \mathcal{A}_y^2}\sin(\omega t) \end{cases} \tag{3.16}$$
Consequently, $\mathcal{A}_y$ is definable as the $\mathcal{Y}$*-quote family index*. Similarly to the first family, here $\mathcal{A}_y = 0$.

- The ***third HALOs' family***, granting the *"oblique coverage"*, may let to have:
$$\begin{cases} y(t) = \mathcal{A}_y \sin(\omega t) + q_y \\ z(t) = \mathcal{A}_z(t) y(t) + q_z \end{cases} \tag{3.17}$$
$$q_z = \left[-\frac{r}{\cos(\epsilon)}, +\frac{r}{\cos(\epsilon)} \right], \quad q_y = -\frac{q_z}{\tan\epsilon + \tan\left(\frac{\pi}{2} - \epsilon\right)} \tag{3.18}$$
$$\mathcal{A}_z = \tan(\epsilon), \quad \mathcal{A}_y = \left| \frac{-\mathcal{A}_z q_z + \sqrt{r^2\left(1 + \mathcal{A}_z^2\right) - q_z^2}}{1 + \mathcal{A}_z^2} - q_y \right| \tag{3.19}$$
We'll denote q_z as the $\mathcal{Q}_z$ *family index*. This parameter has been set to zero, whereas the orbital tilted-plane ϵ equal to $+45°$.

- The ***fourth HALOs' family***, granting a *"circular coverage"*, could be written as:
$$\begin{cases} y(t) = \mathcal{A}_y \sin(\omega t) \\ z(t) = \mathcal{A}_z \cos(\omega t) \quad \text{with} \quad \mathcal{A}_y = \mathcal{A}_z = r \in [0, +r] \end{cases} \tag{3.20}$$
Eventually, $\mathcal{A}_y = \mathcal{A}_z$ as the *Radius family index*.

Most critical trade-offs concern how fixing each orbital amplitude $\mathcal{A}_y$ and $\mathcal{A}_z$ w.r.t. chosen ω. Solar sail's angles α and δ will deeply depend on selected amplitude values, regarding to look for both orbital and attitude periodical solutions. This process is investigated upon several numerical executions by fixing $\frac{\partial Q}{Q}$ and $r_{S_{opt}}$ to those designed parameters found in precursor mission preliminary sizing. Moreover, each *HALO* family's angular velocity ω has been exactly fixed to $\omega_\odot$ for simplicity. The x-axis of final *HALO* orbital trajectories have been scaled with respect to the approximated position of L_1, denoted as x_{L_1}. This scaling was achieved by introducing $x^* = x - x_{L_1}$ to determine the best-fitting amplitude for each involved family. The same family indices were chosen to observe differences in the responses of the attitude angles α and δ. This section desires to discuss and introduce encountered numerical issues both given by chosen amplitudes and numerical limitations due to solving $\mathcal{F}_1^*$.

The ***SRP Control Law*** is performed to control both attitude angles and trajectories simultaneously, ensuring the desired periodic behavior by specifying $\omega_\odot$ for calculating the dimensionless simulation period T. Several values of r are tested in *bvp4c* for each family index, but $r = 200 r_{S_{opt}}$ was ultimately selected. Each periodic trajectory is traced, where the solar sail ranges from $-80 \div +25$ Km relatively to L_1 (black-dot point) along the x-axis, while $y-$ and $z-$axis to $-800 \div +800$ m contribute minimally as direct result of chosen r. Regarding velocities, **figure 3.3** and **3.4**, these range from $0 \div 2.8$ $\frac{m}{s}$, with maximum and minimum values occurring at midpoints on x^* and at the outer boundaries, respectively.

Family indices r are selected by obtaining a unique solution from $\mathcal{F}_1^*$, letting to achieve continuous and periodic attitude angles. Whenever choosing higher $\mathcal{A}_y$ and $\mathcal{A}_z$ amplitudes, the solver isn't able to look for α cause by both non-existing solutions and encountered Jacobian singularities, hence function evaluations not converging to real zeros. In particular, by choosing higher amplitudes, consequent accelerations a_y and a_z would be too high and $\mathcal{F}_1^*$ non-linear equation never nullify. In this way, *MATLAB* function *fzero* will either return an empty-vector or error, interrupting the code's execution and bringing to unsolvable simulations. In this way, reasonable periodical trajectories can be achieved choosing r as above-discussed, hence neither too high or low, in order to provide physical admissible paths.

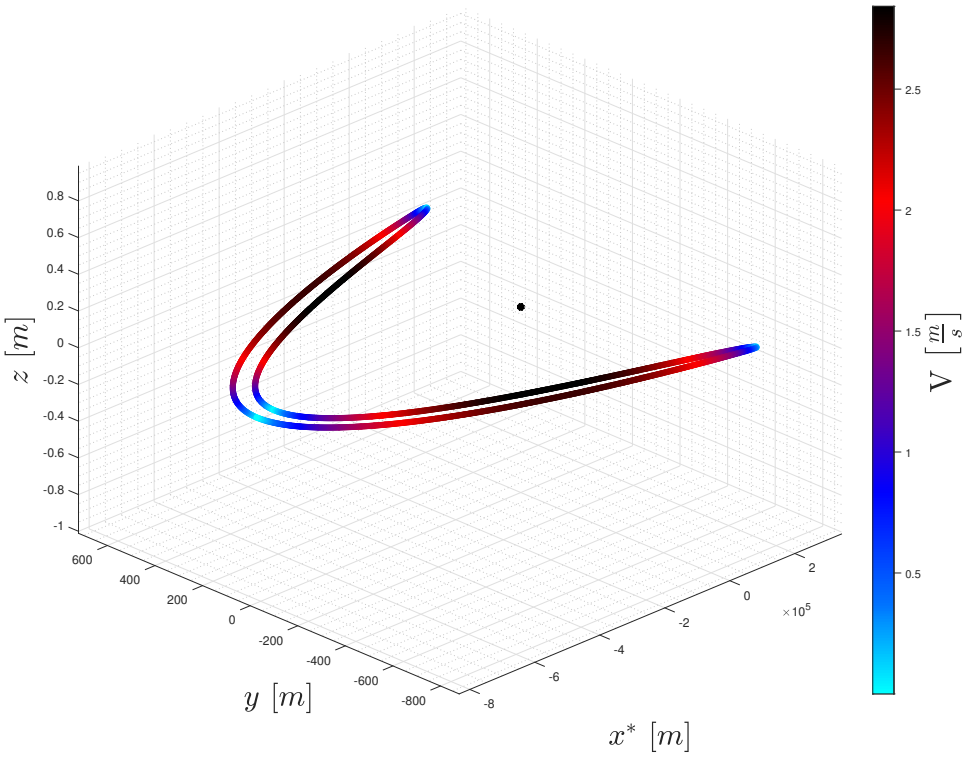

(a) ***First HALO family.***

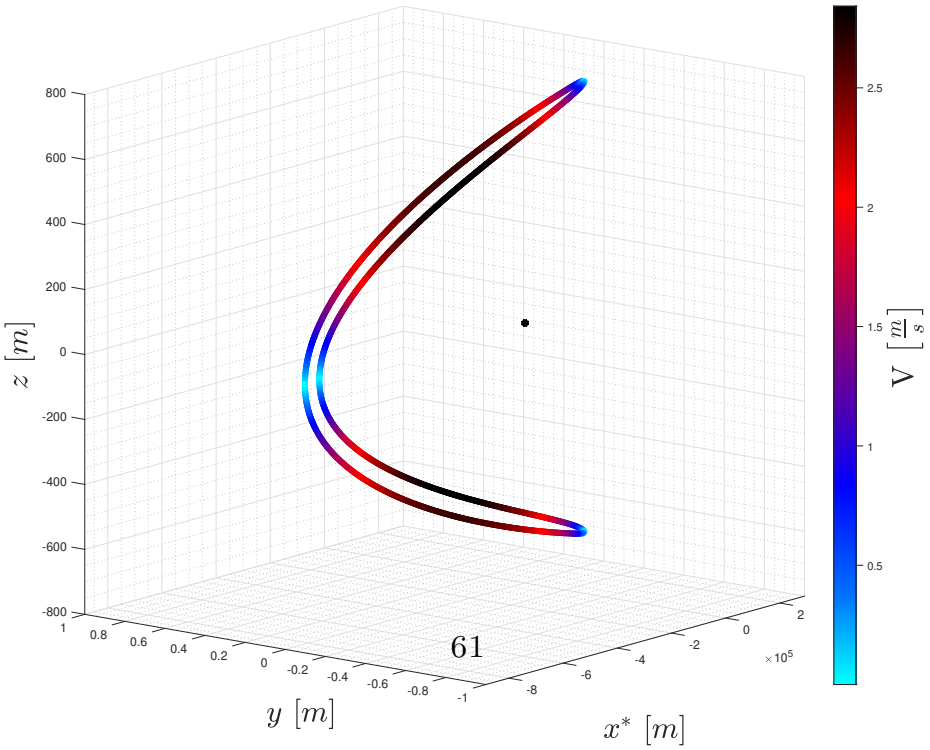

(b) ***Second HALO family.***

Figure 3.3: ***Horizontal and vertical coverages.***

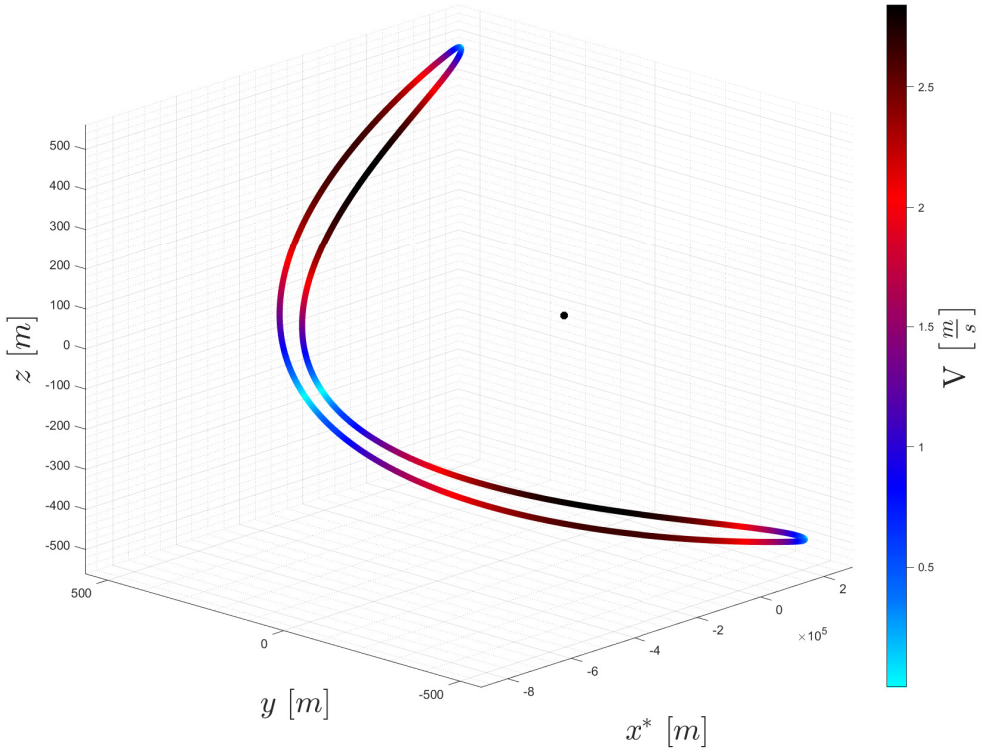

(a) ***Third HALO family.***

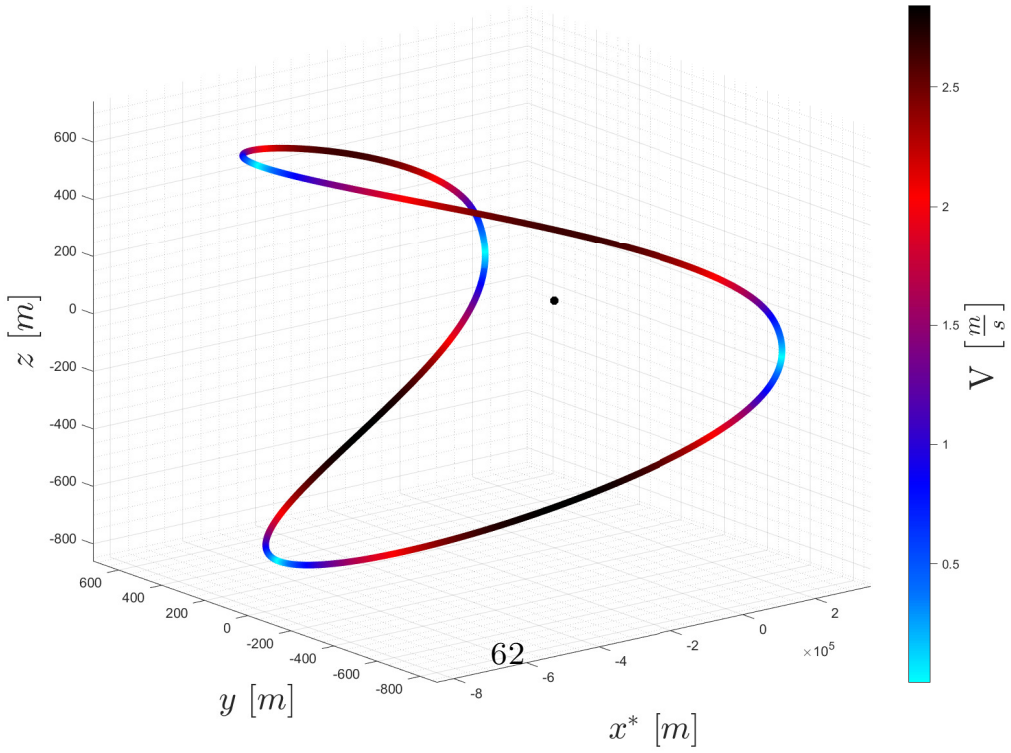

(b) ***Fourth HALO family.***

Figure 3.4: ***Oblique and circular coverages.***

3.2.4 Solar Radiation Pressure and Albedo

Solar radiation force can be easily obtained by applying the Newton's second law of dynamics:

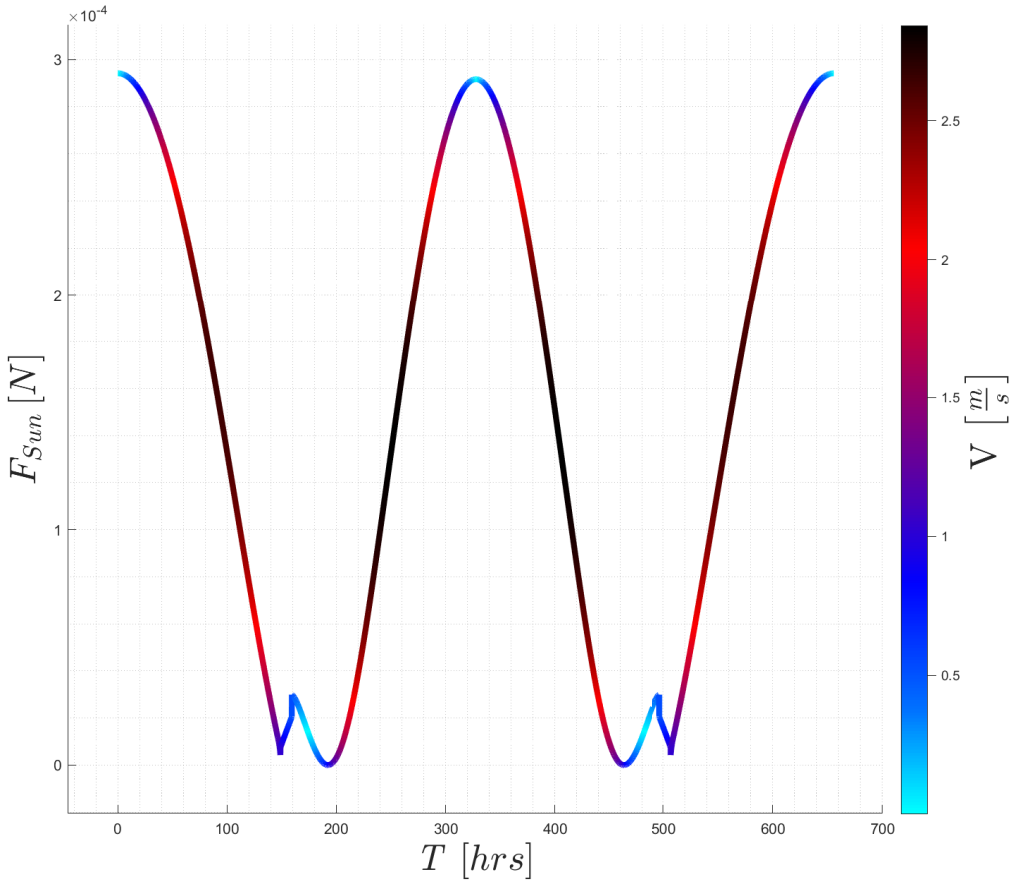

Figure 3.5: ***Solar radiation forces.***

It results comprehended between $0 \div 2.95 \cdot 10^{-4}$ N and its general trend can be paired to achieved τ angles. The left and right shifts are similar to that found for τ and local minima are achieved in proximity of attitude angles' discontinuities. Local maxima are retrievable when τ reduces to 0°, in which the solar sail's maximum exposition is granted. Moreover, the effective projected solar sail's area is the highest w.r.t. solar radiation pressure and this would mean to have $\boldsymbol{r}_{43}$ going to be parallel to $\hat{n}$, hence reducing incident transverse force components hitting the sail.

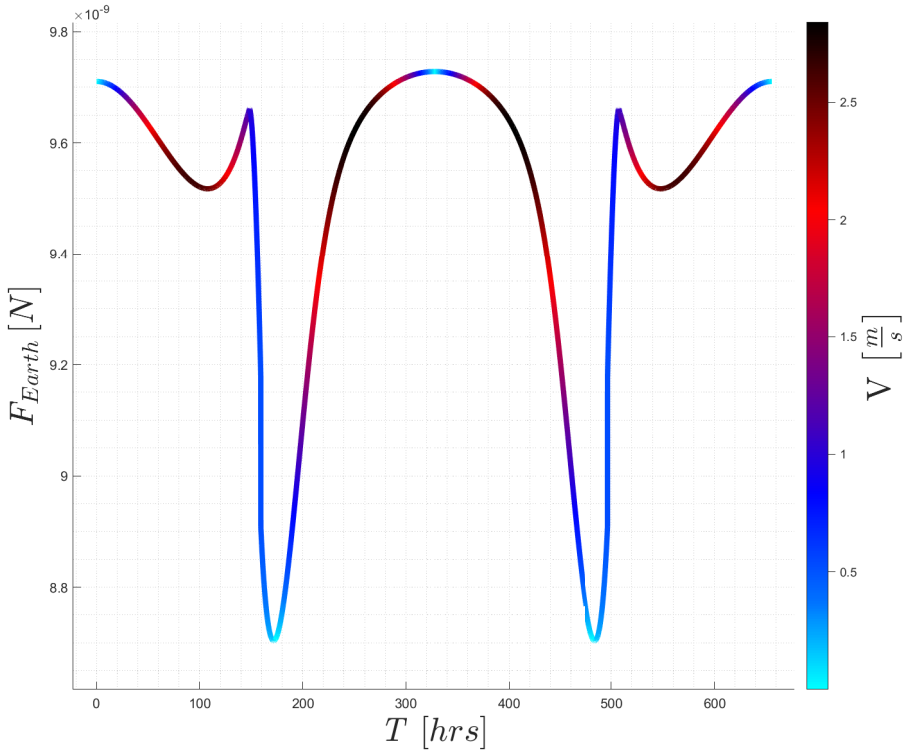

(a) ***Terrestrial reflected radiation forces.***

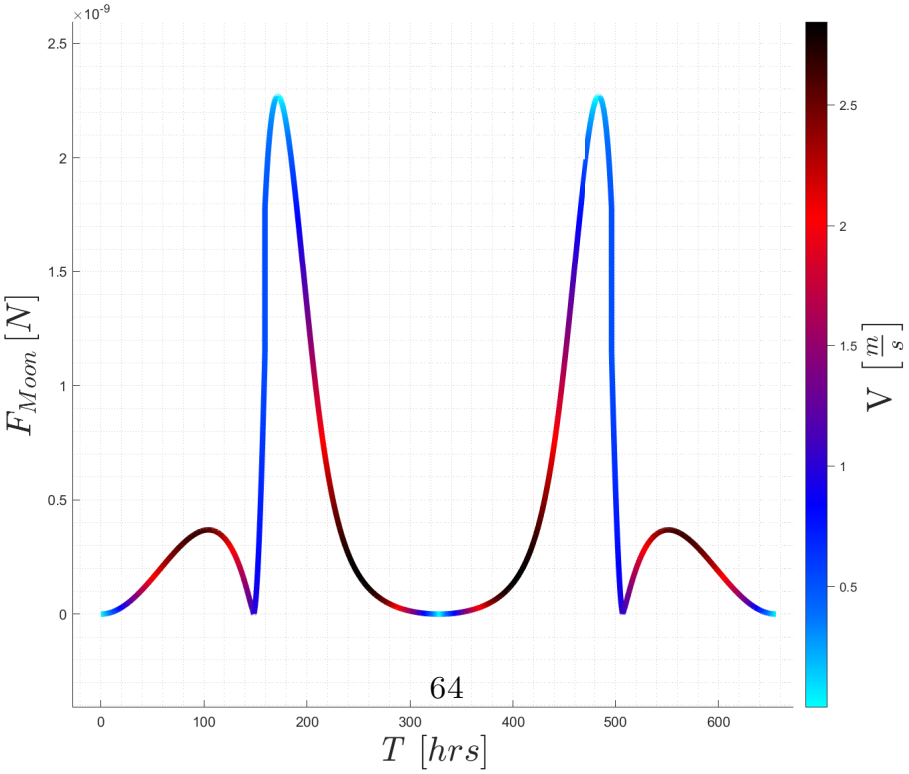

(b) ***Lunar reflected radiation forces.***

Figure 3.6: ***Primary bodies' reflected forces.***

Finally, reflected radiation forces due by Earth and Moon are discussed. Involved sizing orders are 10^{-8} and 10^{-9} N respectively, exhibiting opposite but similar trends over simulation period T. These external forces result negligible on the grounds of obtained sizing orders, hence it's possible to leave out them from both translational and rotational dynamics. Both these charts are depicted using colormaps, **figure 3.6**, for highlighting solar sail's orbital velocities at each time instance, in order to let their pair to both attitude angles and periodic trajectories easier to inspect.

3.3 Ideal Attitude Control

This section addresses the problem of studying the ideal control law to achieve designed attitude by following cone and clock angles found in **subsection 3.2.2**. As for simplicity, there will be considered the solar sail as a *"Rigid-Body satellite"*, denoted as $\mathcal{B}$. The goal of this section could be resumed by the following mission statement:

"Developing an ideal attitude control method to optimally control the solar sail's cone and clock angles achieved from gained periodic trajectories."

3.3.1 Inertia Matrix in Sail's Body Frame

Involved Rigid Body $\mathcal{B}$ requires to be defined by Inertia matrix, as in [**46**]:

$$\mathbf{I} = \begin{bmatrix} I_x & -I_{xy} & -I_{xz} \\ -I_{xy} & I_y & -I_{yz} \\ -I_{xz} & -I_{yz} & I_z \end{bmatrix} \tag{3.21}$$

$$I_x = \int_{\mathcal{B}} \left(y^2 + z^2\right) \partial m \tag{3.22}$$

$$I_y = \int_{\mathcal{B}} \left(x^2 + z^2\right) \partial m \tag{3.23}$$

$$I_z = \int_{\mathcal{B}} \left(x^2 + y^2\right) \partial m \tag{3.24}$$

$$I_{xy} = \int_{\mathcal{B}} xy \partial m \quad , \quad I_{xz} = \int_{\mathcal{B}} xz \partial m \quad , \quad I_{yz} = \int_{\mathcal{B}} yz \partial m \tag{3.25}$$

The ***Huygens-Steiner theorem*** is necessary to study $\mathcal{B}$ w.r.t. the solar sail's *COM*. Results may confirm the x axis would be the major one, y the intermediate, and z the minor one. Although the overall dynamics were been explained through the active control system, controlling the solar sail along this specific axis may grant

significant resistance to lateral deviations caused by external disturbances. This stabilization can be considered the initial attitude phase, allowing the system to continuously align to mission's uplink commands. The slew maneuver assumes that CubeSat structure, the sail and booms' masses stay constant. For these lasts, their geometric properties are defined by their internal and external radius, meaning they are treated as hollow structures with a non-zero thickness.

3.3.2 External Torques

Introducing the body reference frame $\mathcal{F}_{\mathcal{B}}$, resulting external torque effects acting on the solar sail would be truly relevant for defining the consequent angular velocities variations. In this way, it's necessary to define the mismatching between two different $\mathcal{B}$ operative points, the first is the usual *COM*, whereas the second is the Center of Pressure *CP*. Their relative distance $\mathbf{r}_{CP}$ between solar sail's foci and its *COM*, expressed as $\mathcal{G}$, has been fixed to the 30% of the maximum system's orthonormal plane of x, containing yz. The general expression needed to define the external torques' effects depend on external radiation forces $\mathbf{F}$ and it's applicable as:

$$\mathcal{T}_i = \mathbf{r}_{CP} \times \mathbf{F} = \begin{vmatrix} \hat{i} & \hat{j} & \hat{k} \\ 0 & r_{CP_y} & r_{CP_z} \\ F_x & F_y & F_z \end{vmatrix} \tag{3.26}$$

3.3.3 Euler and Kinematic Equations of Dynamics

Designed Precursor mission is thought attached to a body-fixed reference frame $\mathcal{F}_{\mathcal{B}}$ and rotating with angular velocity $\boldsymbol{\omega}_{\mathcal{B}} \in \mathbb{R}^3$, The attitude dynamics pursues to establish the relationship between solar sail's inertia momenta, external disturbances and actuation devices' desired angular velocities, this to verify these lasts periodicity over simulation period T. The most general expression, retrievable in [**46**], for describing the solar sail's attitude control system would be:

$$\begin{pmatrix} \mathcal{L} \\ \mathcal{M} \\ \mathcal{N} \end{pmatrix} = \left(\frac{d\mathbf{H}}{dt} \right)_{\mathcal{B}} + \boldsymbol{\omega}_{\mathcal{B}} \times \mathbf{H} \tag{3.27}$$

The previous expression can be significantly simplified to determine the general angular velocities expression w.r.t. $\mathcal{B}$.

$$\mathbf{I}\dot{\boldsymbol{\omega}}_{\mathcal{B}} + \boldsymbol{\omega}_{\mathcal{B}} \times (\mathbf{I}\boldsymbol{\omega}_{\mathcal{B}}) = \mathbf{M}_{\mathcal{B}} \tag{3.28}$$

$$\Rightarrow \qquad \dot{\boldsymbol{\omega}}_{\mathcal{B}} = \mathbf{I}^{-1} \left(\mathbf{M}_{\mathcal{B}} - \boldsymbol{\omega}_{\mathcal{B}} \times (\mathbf{I}\boldsymbol{\omega}_{\mathcal{B}}) \right) \tag{3.29}$$

in which $\mathbf{M}_{\mathcal{B}}$ stands for all torques acting on the solar sail. $\mathcal{T}_i$ contribute figures inside $\mathbf{M}_{\mathcal{B}}$ when calculating Euler equations of dynamics. The resulting first-order

differential equation allows us to determine the time history of the angular velocity components, which are essential for calculating consequent quaternions.

3.3.4 Angular Momentum

The general expression of angular momenta belonging to a rigid body's element ∂m, expressed using the notation shown in **[46]**, and then referred to the entire system, is:

$$\partial \boldsymbol{h}_{\mathcal{B}} = \boldsymbol{r} \times (\partial m \boldsymbol{v}) \tag{3.30}$$

in which $\boldsymbol{v}$ stands for the mass element velocity, whereas $\boldsymbol{r}$ to its position vector. Once extending this expression to a rigid-body, total angular momentum can be given by:

$$\boldsymbol{h}_{\mathcal{B}} = \int_{\mathcal{B}} (\boldsymbol{r} \times \boldsymbol{v}) \, \partial m \tag{3.31}$$

It's possible to express the body's rotation by highlighting the angular velocity $\boldsymbol{\omega}_{\mathcal{B}}$, around its center of mass COM, related to the consequent radius vector $\boldsymbol{r}$ as:

$$\boldsymbol{h}_{\mathcal{B}} = \int_{\mathcal{B}} [\boldsymbol{r} \times (\boldsymbol{\omega}_{\mathcal{B}} \times \boldsymbol{r})] \, \partial m \tag{3.32}$$

Regarding all previous definitions given by the angular velocity $\boldsymbol{\omega}_{\mathcal{B}}$ and $\boldsymbol{r}$ as the radius going from the sail's COM to the mass-element ∂m_i, by applying the cross-vector product it is possible to define the relationship between $\boldsymbol{h}_{\mathcal{B}}$ and $\boldsymbol{\omega}_{\mathcal{B}}$:

$$\boldsymbol{h}_{\mathcal{B}} = \boldsymbol{I}\boldsymbol{\omega}_{\boldsymbol{\mathcal{B}}} = \begin{bmatrix} I_x & -I_{xy} & -I_{xz} \\ -I_{xy} & I_y & -I_{yz} \\ -I_{xz} & -I_{yz} & I_z \end{bmatrix} \begin{pmatrix} \omega_{\mathcal{B}}^x \\ \omega_{\mathcal{B}}^y \\ \omega_{\mathcal{B}}^z \end{pmatrix} \tag{3.33}$$

3.3.5 Ideal Angular Velocities

On the other side, it can be useful to establish which would be ideal angular velocities that actuation devices may provide to assure the solar sail describing desired both attitude angles α and δ.

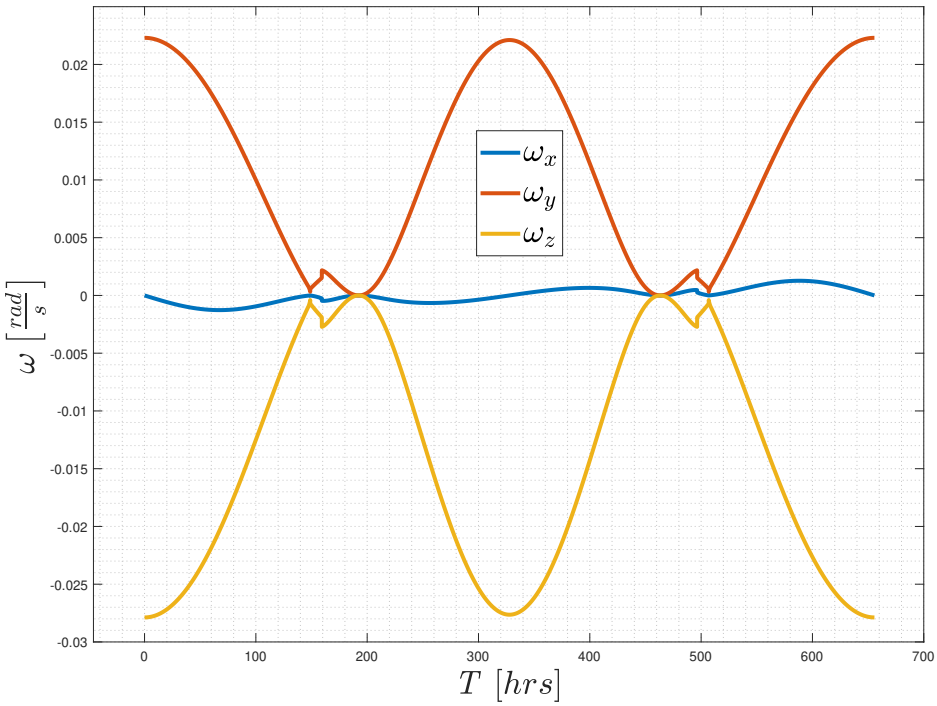

Figure 3.7: ***Ideal actuation angular velocities.***

It's expected to look for periodic solutions throughout the entire orbital period. Most significant contributes regard those in y and z coordinates, whereas negligible for x-axis ones.

Chapter 4

Deployment Mechanism

The solar sail deployment mechanism, based on both trajectory and attitude analysis, is definable as that subsystem needed to unfold an initial stowed, and very thin, high-tech light membrane to solve specific functional operations, including reflecting a portion of external radiations and dissipate incoming heat out-in-space. This project aims to specialize on reflective capabilities oriented to facilitate space-based deployment systems' efforts aimed at mitigating climate change on Earth, drawing insights from the leaded precursor mission to refine the subsystem's effectiveness and future implementation to the Planetary Sunshade mission.

4.1 Introduction and Purposes

This system can strategically be placed close to L_1^*, creating a reflective shield that reduces the amount of solar radiation hitting Earth. The proposed preliminary design must conform to both volume and mass constraints typically found in CubeSat applications, particularly those in the 3U category, ensuring that the mission is feasible within the limits of small satellite technologies.
The main objective of this project is to identify a suitable deployment mechanism that will enable the solar sail to unfold properly and remain horizontally oriented relative to the yz orbital plane, **figure 4.1**. Proper deployment is essential for ensuring a uniform distribution of radiation pressure, which is critical to achieving the desired effects on the Earth-Moon system. In the first part of this chapter, the selection of materials that would be best suited for the precursor mission deployment phase is explored. This involves a thorough analysis of both static and dynamic responses of components needed to comprehend most critical loads acting during the deployment phase. Understanding how these materials behave under various conditions, including vibration and stress, is critical to ensuring the success of the mission. We evaluated the trade-offs between material strength, flexibility,

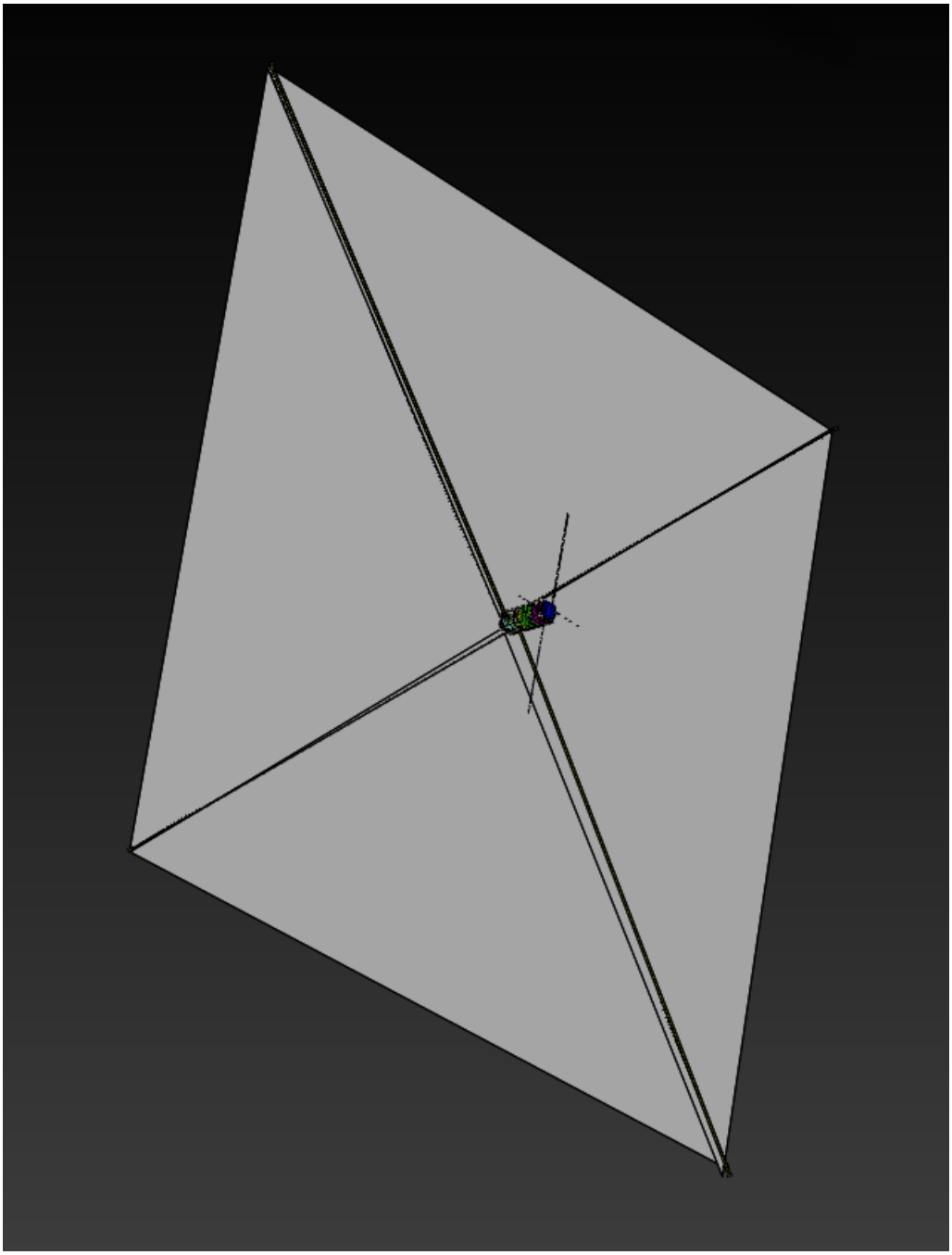

Figure 4.1: ***3U+ CubeSat and square-deployed solar sail.***

and lightweight properties. The second part of the project focuses on the physical design of the solar sail itself. This includes a detailed examination of the required

electronics, the types of electric motors suitable for controlling the deployment process, and the challenges associated with scaling up the technology for the next large-scale industrial prototyping.
Solar sail systems require precise control mechanisms to ensure that they unfold correctly and maintain the desired orientation throughout their operation. The electric motor must provide sufficient torque while remaining energy-efficient. In addition, challenges associated with the transition from prototype to large-scale production are also considered, especially given the novel nature of solar sail technology and the complexities of manufacturing components that need to perform in an extreme environment of space.
This part of the project has been developed in collaboration with the *NOTTSPACE* group, who have provided invaluable guidance in space systems engineering. Their contributions have helped refine the approach to work on the deployment mechanism and overall design of the entire solar sail, proposing a newer model that can be technically feasible and adaptable to future space missions.

4.2 Literature Review

As support for the preliminary design of the mechanism, this chapter aims to catalog both the deployment and the properties of the material to try to estimate an initial size of the entire system. Numerous studies have been conducted on both

Space mission	***Booms mass*** $[g]$	***Booms length*** $[mm]$	***Booms tipology***
"InflateSail"	*4 X 125*	*35 ÷ 90*	*Inflatable Cylindrical BRC CFRP booms*
"LightSail-A"	*4 X 110.25*	20	*Elgiloy stainless steel metallic TRAC booms*
"NEA Scout"	*4 X 250*	60	*Stainless steel TRAC booms*
"NanoSail-D2"	*2 X 110*	34	*Elgiloy stainless steel metallic TRAC booms*
"CubeSail"	*4 X 162*	32	*BeCu tape spring and carbon composite booms*

Table 4.1: ***Booms' properties.***

technical characteristics and solar sail deployment strategies, **table 4.1**, **table 4.2** and **4.3**, exploring potential configurations for both stowed and fully deployed architectures. The intended mechanism is thought as imposing a radial booms'

Space mission	***Material***	***Density*** $\left[\frac{g}{m^2}\right]$	***Thickness*** $[\mu m]$
"InflateSail"	*Aluminized-Kapton laminate (PEN)*	*15*	*12*
"LightSail-A"	*Seamed Aluminized-Mylar*	7	4.5
"NEA Scout"	*Aluminized Polyimide CP-1 substrate*	41.86	2.5
"NanoSail-D2"	*Ultra-phin Aluminized Polymer CP-1*	50	7.5
"CubeSail"	*Aluminized-Kapton*	12	6.2

Table 4.2: ***Solar sail sizing features.***

deploy technique, letting them to achieve the final unfolded configuration, from an initial critical stowing CubeSat empty volume, sized as desired from precursor mission orbital design.

That volume left free by other similar solar sailing conducted space missions would highlight that there may be required 2U to let developing a deployment mechanism, **figure 4.2**. For instance, imagined mechanism is provided by four distinguished measuring tapes wrapped to a central rotating spindle, in which each couple of tapes goes to describe a differently oriented plane intersecting that of the sail w.r.t. their ending hooks. Moreover, structurally speaking, proposed mechanism is completely comprehended between four distinguished CubeSat's structural rods and inner ribs, reducing as more its total length, width and mass, but also capable to suffer higher loads, as introduced in [**48**].

The primary objective is to maximize the structural masses, thus increasing the available free volume to accommodate internal electronics and stowed booms. By optimizing this parameter, the design can ensure that more space is allocated for critical components, improving the integration of the system while respecting volume and mass constraints. This comparative tables, referenced in [**49**], [**50**], [**51**], [**52**],

Space mission	***Deploy method***	***Sail masses*** $[g]$	***Structural mass*** $[Kg]$
"InflateSail"	*Origami Pattern inflated by CGGs*	150	*3.7002*
"LightSail-A"	*Z-folding technique*	224	3.6852
"NEA Scout"	*Non-rigid gossamar system*	3600	0.2502
"NanoSail-D2"	*P-POD technique*	500	3.5202
"CubeSail"	*P-POD technique*	300	3.4022

Table 4.3: ***Solar sail deploying methods and masses.***

[53], **[54]**, **[55]**, **[56]**, **[57]**, **[58]**, **[59]** and **[60]**, highlight the critical importance of the precursor mission preliminary sizing, demonstrating how significant the impact of early design decisions and assumptions can be on overall final performances.

4.3 Deployment Mechanism Details

The material's choice may respect several requirements including optical, mechanical, and thermal features. Several Decision matrices are needed to complete this first task:

Property	***Value***
Poor	(1)
Below average	(2)
Average	(3)
Above average	(4)
Excellent	(5)

Table 4.4: ***Decision matrix property values.***

Type	***Reflectivity [%]***	***Width*** $[\mu m]$
Mylar	95 ÷ 98 (5)	2 ÷ 10 (5)
Kapton	90 ÷ 95 (4)	2 ÷ 12.5 (4)
Lexan	90 ÷ 95 (4)	5 ÷ 10 (5)
CFRP	80 ÷ 95 (3)	100 ÷ 500 (2)
Nylon 6.6	85 ÷ 95 (4)	12 ÷ 50 (3)

Table 4.5: ***Materials' properties decision matrix, [61], [62].***

Density $\left[\frac{g}{cm^3}\right]$	***Price*** $\left[\frac{£}{m^2}\right]$	***Melting point*** $[K]$
1.39 (4)	5 ÷ 10 (5)	438 ÷ 523 (3)
1.42 (3)	10 ÷ 100 (4)	773 (5)
1.20 (5)	15 ÷ 150 (2)	493 ÷ 503 (3)
1.50 ÷ 1.60 (1)	20 ÷ 200 (2)	423 ÷ 473 (2)
1.13 ÷ 1.15 (5)	20 ÷ 100 (2)	493 ÷ 528 (3)

Table 4.6: ***Materials' functional decision matrix.***

Material	*Performing features' decision matrix*
Mylar	This material behaves pretty good for space-propulsion pursues due to its high reflective optical properties, UV and extreme higher temperatures' resistance. It's characterized by easier deploying ways. It could be capable to reflect a slight radiance heat, used as stabilizing material for satellite's internal subsystems, flexible and tensile inextensible, tears and impacts too, inert, it provides also an high electrical insulation, very light and tough. This material is widely retrievable on global marketplace mainly as sheets and foils. (5)
Kapton	Characterized by exceptional thermal properties, highly flexible, suitable inside aggressive chemical environments, very high mechanical resistance. It's nowadays very used in those space-missions that require higher thermal stabilities, characterized by a good tensile strength and tears. This material could be bought on marketplaces as rolls and adhesive tapes. (3)
Lexan	It behaves well to external impacts, noticibly to its light weight, flexible, solar radiations strength to direct exposures and good thermal stabilities. It's transparent, tensile strength, good electrical insulation material, higher chemical inertia, ease of processing, used also for structural and electronic applications. It's widely available for both industrial and technological applications. (2)
CFRP	High rigidity for shape and integrity, primarily used for the frame and deployment arms, excellent resistance to extreme temperatures. The solar sail would be able to effectively withstand the state of tension during deployment without breaking, with a high elastic modulus, resistance to corrosion, UV radiation, and cosmic radiation. This is enough available on global marketplace but quite expensive. (1)
Nylon 6.6	One of the lightest materials among those proposed, highly reflective, very flexible, low thermal emissivity, sensitive to UV degradation with prolonged exposure, early aging under stress, prone to oxidation. Widely available on marketplaces. (4)

The choice of Mylar film (leading with 27 points from Decision matrices) appears as the best suiting for reflecting incoming radiation as more. The sail must reflect at least the 95% of that radiation, in synergy with the investigation of trade-offs regarding the availability and costs of the materials. It's imagined that once the system would result fully deployed in space, the final unfold need to be achieved by using an enough powerful electric motor, in which it will be selected afterwords have paired its sizing to those of the electronics, wires and deploying booms' required torques.

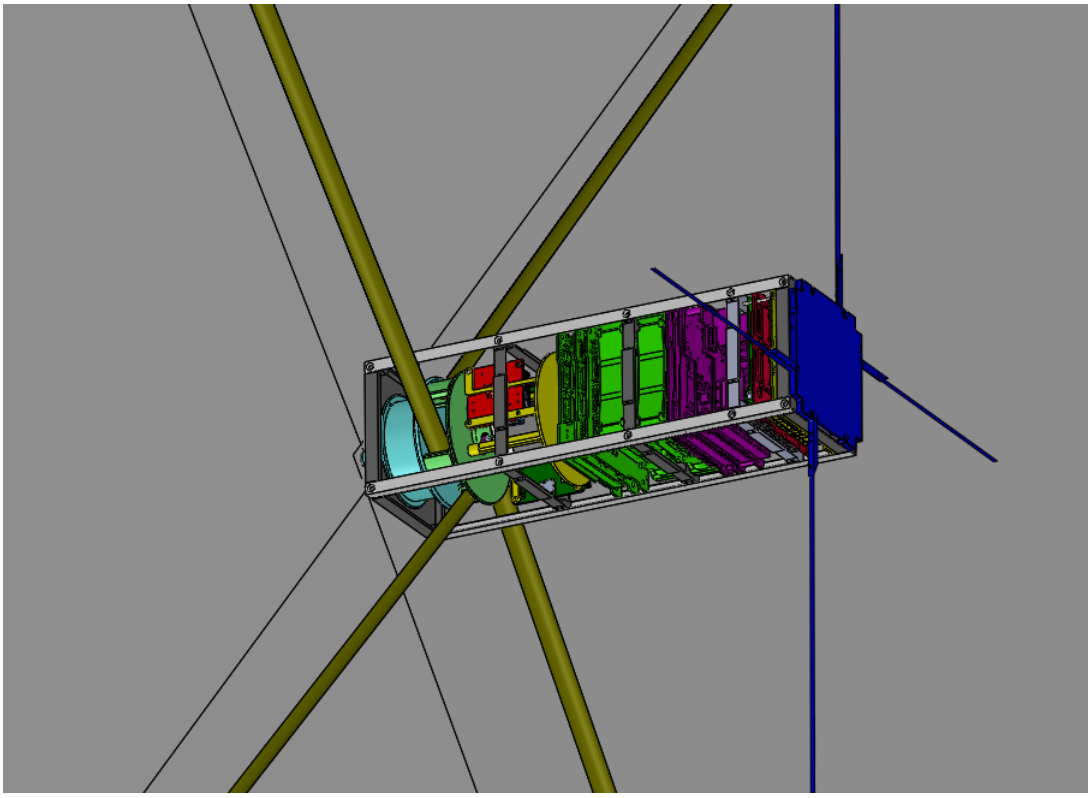

Figure 4.2: ***Final assembly with EPS (green), ACS (violet), OBC (red) and COMMSYS (blue) subsystems.***

Nominal Voltage related to the electric motor shall be comprehended between 5 and 12 V, as the consequent needed power should be strictly lower than of that supplied by solar-panels and absorbed by batteries, in which the first need to be located efficiently to both counteract the *COM* variation moving towards the sail and booms' disposal, but also for efficiently absorbing incoming radiation.

Each of the booms have been wrapped around the electric motor's rotating shaft following a counterclockwise orientation and then following a specified half-spiral

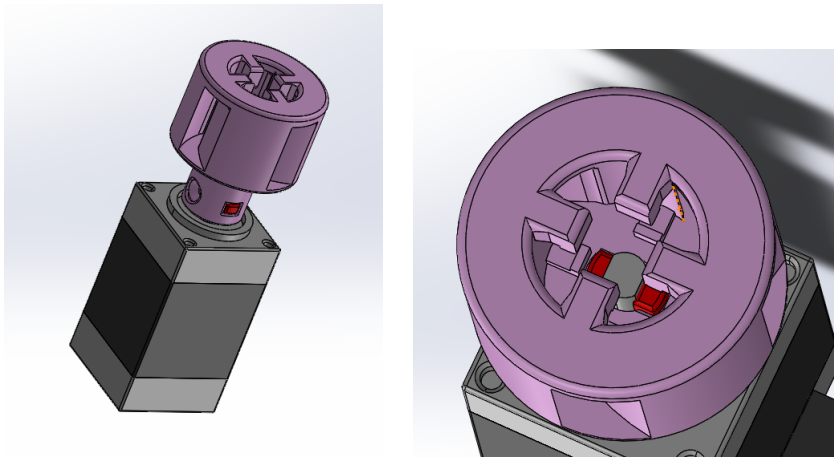

(a) *Lateral point of view, vertical-matching feather-key.*

(b) *Higher point of view, horizontal-matching feather-keys.*

Figure 4.3: ***Electric motor and spindle assembly.***

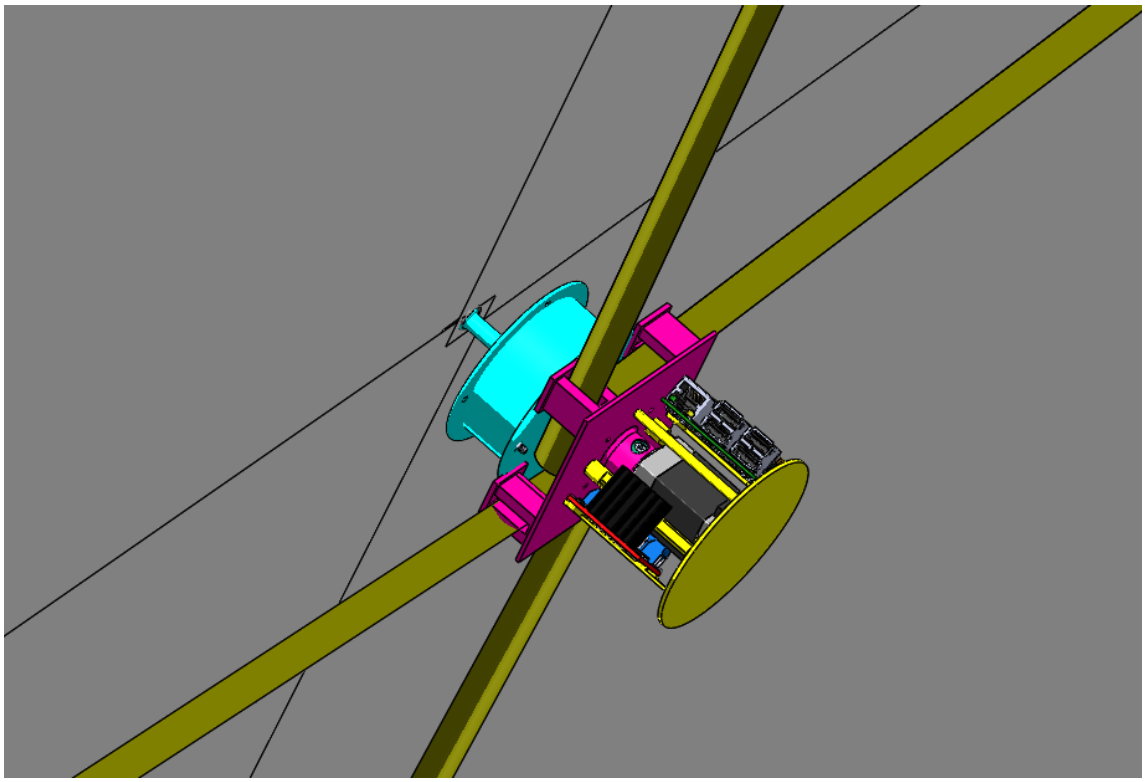

Figure 4.4: ***Deployed α-tilted booms and electronics in detail.***

folding until reaching each of the four perpendicular rectangular holes belonging to the upper plate support (purple-colored). These may act as O-shaped channel directors in section describing a not-perfect horizontally planned path, but instead a tilted one by $\alpha = 1.3849°$, towards the upper sail's stowing component (cyan-colored), depicted in **figure 4.4**. Each of the booms have been characterized by one hook, each of them pulling two vertices of a single triangular-shaped foil, whose entire assembly should be taken squared and divided into four symmetrical sections. All these will have in common their *Master* and *Slave rings*, one and eight respectively located on the x-axis and on the yz lateral-plane, depicted once thinking to the CubeSat 3U+ final assembly **figure 4.2**. The *Master ring* would connect together each of the four cut sections w.r.t. the vertical shaft belonging to that component concerning the sail's stowing support. The mechanism works through the mini-hybrid *ASTROSYN-MY5002* stepper motor, whose torque provides a sufficient contribute to its rotating spindle, to which have been mounted all measuring tapes to fulfill a fully operative articulated mechanism, although characterized by a single-point failure design. This spindle and the electric motor's shaft, **figure 4.3**, have been rigidly fixed using two radial M3X3 screws and three feather keys inserted into the rotating component, this for assuring both horizontal and vertical booms' coupling.

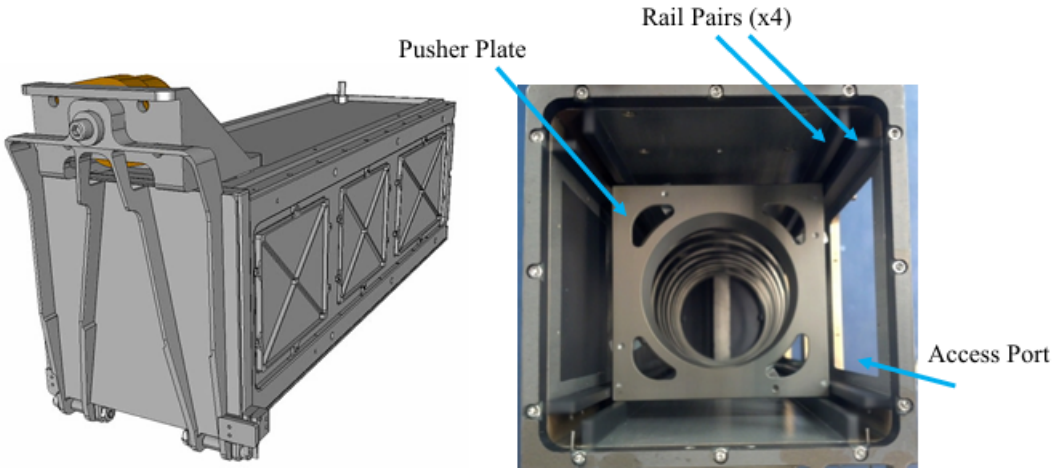

Figure 4.5: ***P-POD dispenser unit.***

What about four foots, **figure 4.6**, applied on the final plate, these are needed for being coupled to the P-POD dispenser, **figure 4.5**, through which the CubeSat 3U+ will be ejected by the pushing plate, strictly following the railway system and eventually reaching the space by using an ending access port [**48**]. It's been decided to leave an half-mil in width between the rotating spindle and the boom's support plate, this for avoiding the friction occurring between both. Once these

booms have been completely stowed, they would be less than 2 cm as radial length from the spindle's vertical main axis, letting to develop a specific support plate accounting them without any interference. The measuring tape's elastic return, due

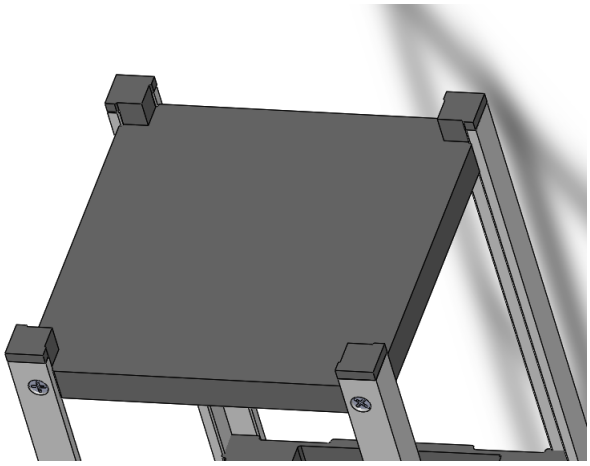

Figure 4.6: ***CubeSat ending foots in details.***

to its inner metallic stiffness, has been mitigated by inserting it from the outside of the boom's support plate and forcing the terminal hook to not physically pass through O-shaped channel directors.

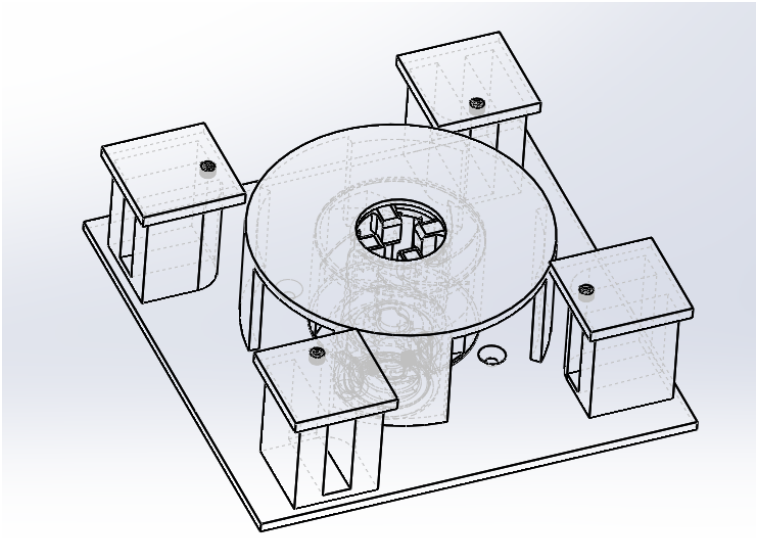

Figure 4.7: ***Booms' plate assembly higher point of view.***

In this way, each boom will strictly follow the counterclockwise rotating shaft

completing the kinematic chain as imagined. On the foreground, the measuring tapes have been solidly attached to the rotating spindle after having simply cut their borders giving them a 'tooth-shape', literally provoking a strong interference like they were welded.

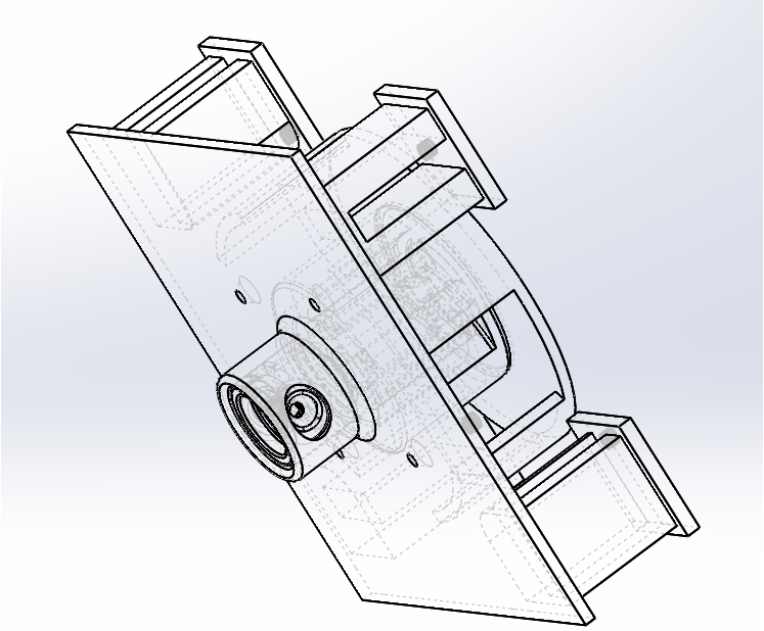

Figure 4.8: ***Booms' plate assembly lateral point of view.***

This solution was preferred for avoiding any pins, screws and unnecessary welded connections that would inevitably lead to structural plastic responses instead of elastic ones and for granting easier inspections and substitutions. On the other hand, it's necessary to realize four carvings inside the spindle for obtaining the desired 90° tapes' angulation for supporting the out-of-plane designing angle α. M3 screws have been selected looking for higher threads' diameters and reducing as more their length, despite these may require more sophisticated analysis for letting them confirm or not. In **figure 4.7** and **4.8**, it's been detailed-down the boom's support plate paired with the rotating spindle and its topping component. This last should be necessary for compacting the wrapped tapes for granting an initial electric motor test, hence not needed to further simulations. The lower sail's plate role will be not only working as stowing something but also letting the booms deploying externally with the desired angular rate α.

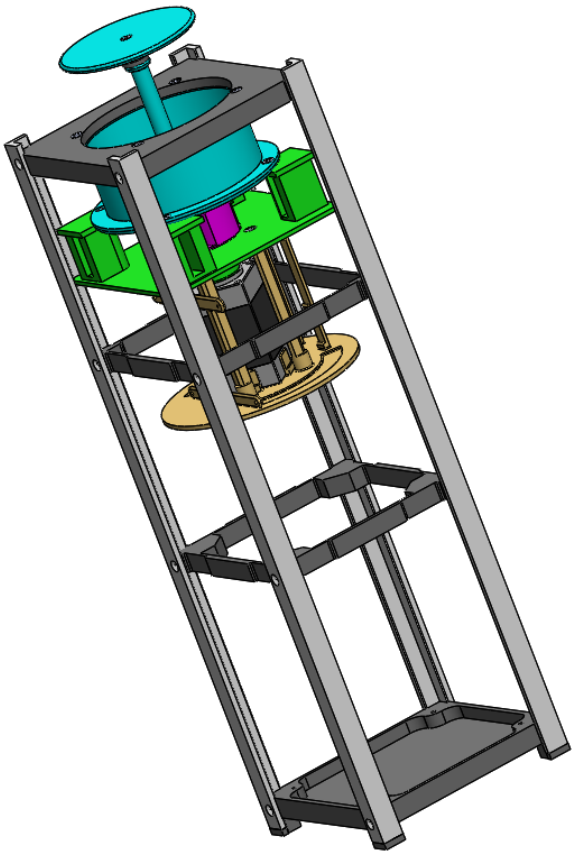

(a) ***CubeSat frontal point of view.***

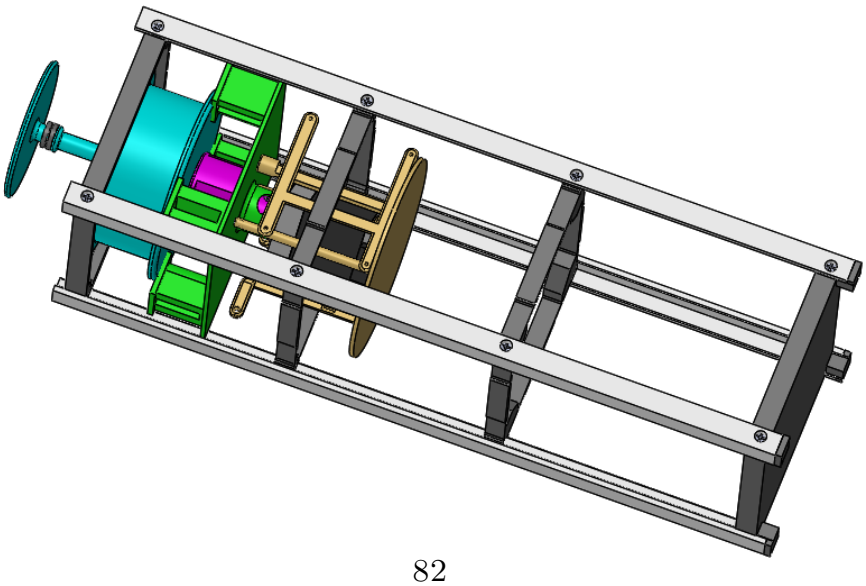

(b) ***CubeSat lateral point of view.***

Figure 4.9: ***CubeSat's 3U+ frame with deployment mechanism.***

One of the most crucial aspects to consider for granting the best fitting booms' folding would be that of defining in which way each measuring tape had to be wrapped and enveloped w.r.t. the central rotating spindle, [**63**]. There were been designed two different versions of the same component to determine the best suiting one.

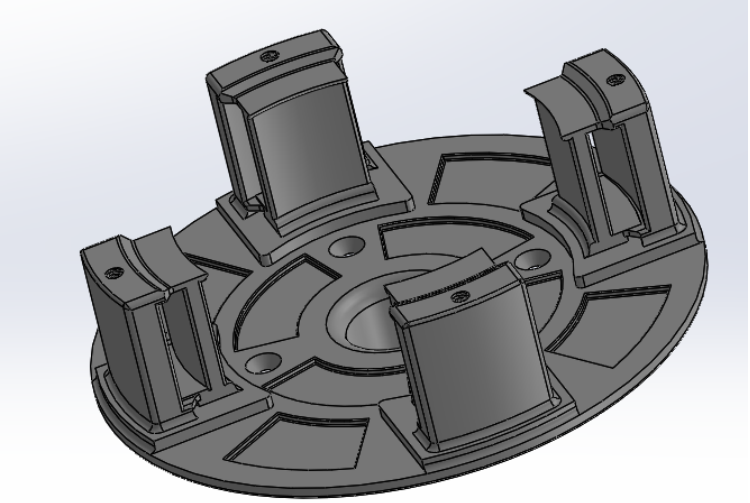

Figure 4.10: ***Booms' plate first modeling version.***

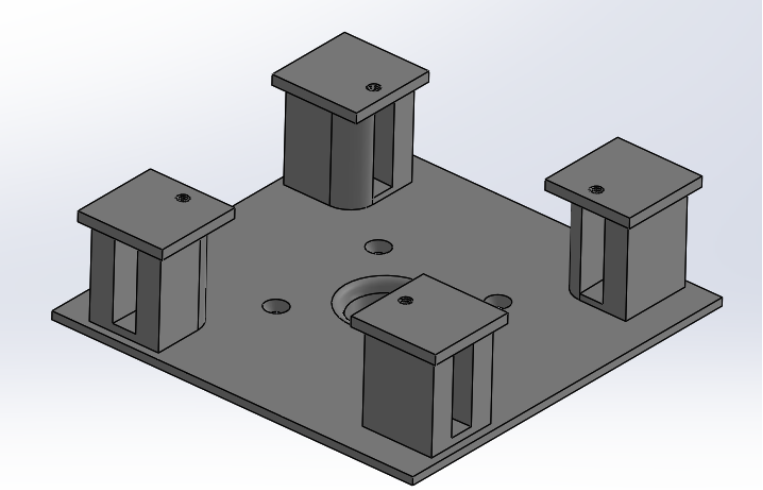

Figure 4.11: ***Booms' latest and updated plate version.***

Both components are thought by realizing a single rotating shaft, letting the tapes to unwrap as counterclockwise and surrounding their deploy through four,

symmetrically applied, vertical supports. It was put into evidence symmetrical holes' position w.r.t. the motor's shaft, binding this plate to the upper and lower ones, hence to that of the sail's stowage and electronics. Although both should be theoretically applied to this project, the first, **figure 4.10**, has the critical issue of bringing an higher tape's torsion and, if thinking to the consequent higher inner stiffness, this wouldn't let them to deploy as desired and expected. Measuring tapes will be folded with too many difficulties in a very small available volume.

These problems are solved as seen for the space mission cited at first, hence granting a truly lower tape's rotational angle once reducing the electric motor's provided torque. Moreover, it's still necessary to not have empty spaces between each of the tapes wrapped one another. In this way the entire mechanism will work with the desired α inclination for granting the sail's final oriented configuration. For these motifs, verified only by mounting the entire mechanism, the choice was fallen to the second architecture, **figure 4.11**. Plates' masses will result to be very similar, despite the difference was made by the only testing issues just described.

4.3.1 Spindle and Booms' Plate Static Analysis

The deployment mechanism's static response method needs to identify the most relevant involved forces and torques, learning the maximum and minimum stresses, but also strains. It's been imagined to use an higher and finer mesh for all the components involved, adopting the *IMS* and eventually simulating the loaded structure.

For instance, the choice of needed constraints may strictly depend on which way the plates would be bound one another using both mechanical (like feather keys) and rigid connections (like screws), as most closed to concrete applications. The main goal is to identify the shaft's highest and lowest displacement amplitudes in the worst conditions ever, supposing to fix the shaft to its ground and leaving free the higher surface edge, this reflecting the first rotation from an initial stationary condition.

Finally, by applying a torque of 9 Ncm (from selected eletric motor, analyzed in next sections) on its lateral cylindrical surface, simulate the modeling to learn what could be obtained in terms of magnitudes.In **figure 4.13**, the maximum displacement amplitude is reached on the highest section and it is 5.4 μm in magnitude, whereas the lowest on its ground.

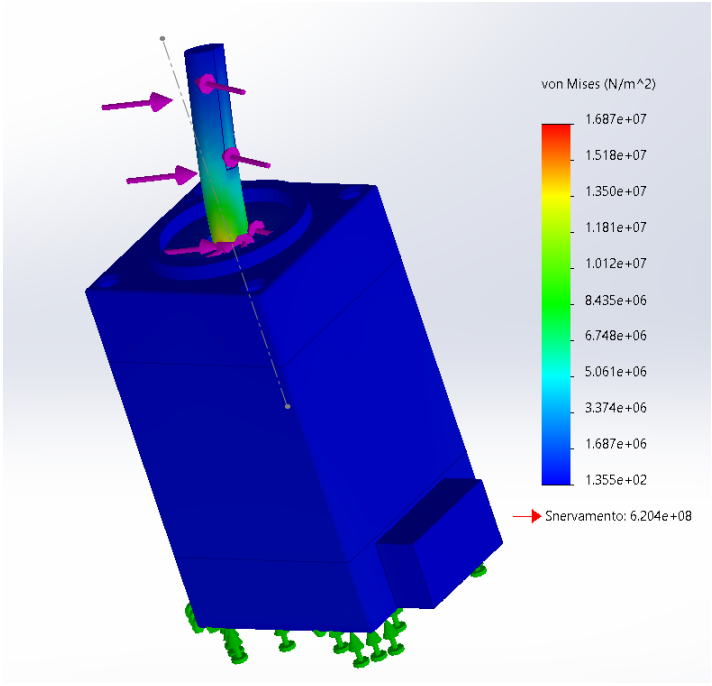

Figure 4.12: ***Electric motor shaft's strains.***

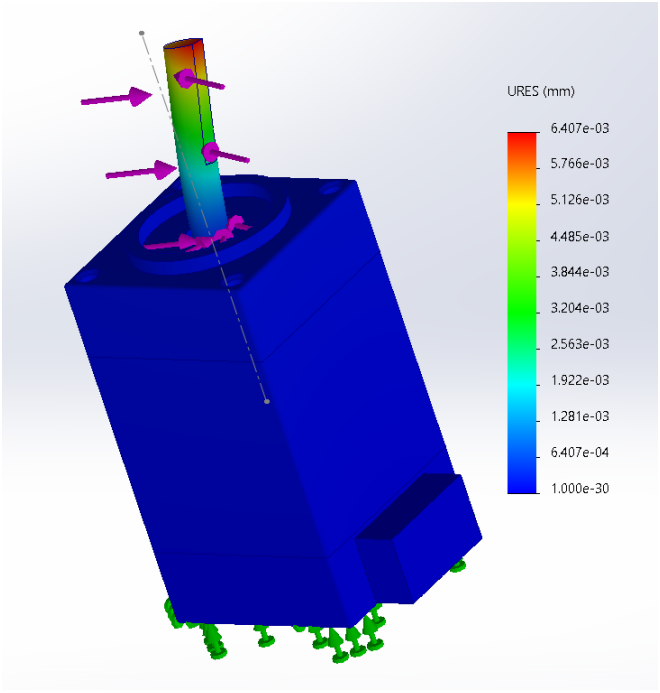

Figure 4.13: ***Electric motor shaft's displacements.***

These lateral variations will result negligible whenever thinking to couple the electric motor and matching feather-keys to central rotating spindle. Stresses, in **figure 4.12**, have been delved by choosing von-Mises criteria, achieving the critical yielding point in $5.2 \cdot 10^8 \frac{N}{m^2}$, depicting the maximum intensities on those elements connected to the higher electric motor plate, whose magnitude should be $1.7 \cdot 10^7 \frac{N}{m^2}$. Only afterwords have been evaluated booms' plates behavior to those forces and torques, it is possible to identify most critical nodes subjected to leaded stresses and strains. Thus, going to remark both the spindle and supports' sizing loads, the consequent meshes have been retrieved:

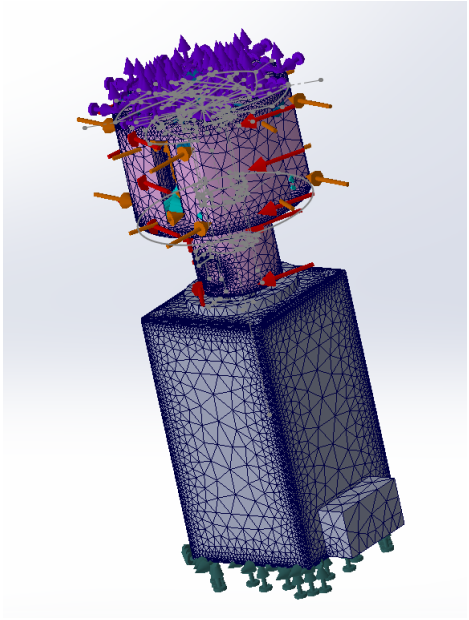

Figure 4.14: ***Spindle and electric motor meshes and loads.***

On the usual rotating spindle, shown in **figure 4.14**, is applied an external torque of 9 Ncm in magnitude, eight 1 N loads on the internal lateral tooth-shaped sections and equivalently other eight 0.01 N instead on the internal higher and lower surfaces. These would aim to replace each measuring-tape's clamp interference w.r.t. the rotating spindle's, letting the mechanism to work as desired. Eventually there were been applied two equally defined clamps to the spindle's top and bottom surfaces for simulating the worst possible conditions ever obtainable. What about booms' support plates, **figure 4.15**, there were thought two clamps (violet-colored), four distributed 10 N forces acting on the internal contact between the vertical supports and measuring-tapes and four distinguished 1300 N forces replacing screws' rigid connections (average value for M3X3 type). Eventually a topping 0.4 N one replacing the weight due to the lower electronics' plate (if simulated on a

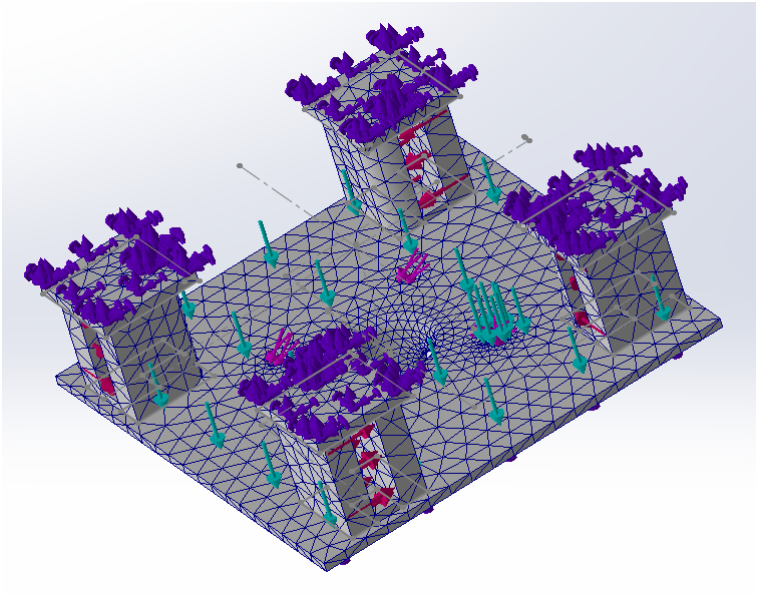

Figure 4.15: ***Higher booms' plate mesh and loads.***

gravity attraction modeling). This last force would be negligible for both higher **figure 4.16** and global **figure 4.17** meshing simulations.

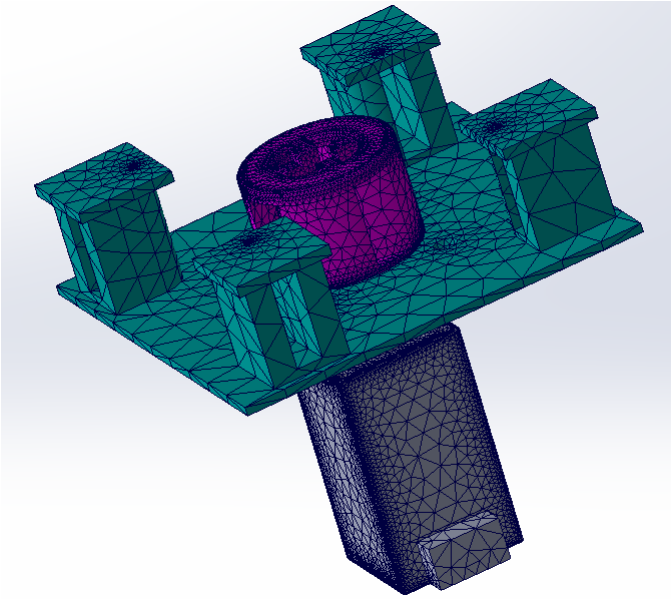

Figure 4.16: ***Higher meshed assembly, frontal view.***

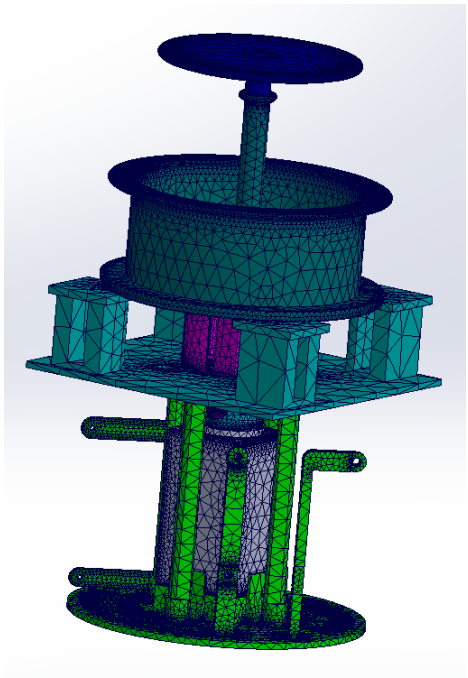

Figure 4.17: ***Frame's global meshing assembly, main view.***

Executing *Solidworks* simulation run, there could be achieved the following results: maximum spindle displacements', **figure 4.18**, amplitudes are obtained in the lowest section, equal to 2.58 μm, whereas most stressed elements, **figure 4.19**, to $2.4 \cdot 10^6 \frac{N}{m^2}$ in magnitude, those related to internal section's tooth-shaped supports. It's remarked that there aren't any contacts between booms' plate and rotating spindle, hence this analysis can be studied as decoupled as initial hypothesis. Delving onto booms' contact point, the highest strained nodes will be that externally compressed by wrapped tapes around the spindle, **figure 4.22**. Highest achieved displacements occur as 0.1 μm in magnitude. These results are symmetrically obtained w.r.t. the spindle and plates' main axis, as certainly expected if trying to simulate the mechanism. On this right, it's shown each *M3X3* screw blockage to the lower electronics' plate, depicting an extended strained region for each placed hole. As already seen for the spindle, it can be useful to learn more about von-Mises strains, also that ones maximized to the internal vertical supports' edge, achieving an averaged value, **figure 4.20**, and this is approximately $1.2 \cdot 10^4 \cdot \frac{N}{m^2}$. *M3* screws, **figure 4.21**, provide a bit more than $5.6 \cdot 10^7 \frac{N}{m^2}$, regarding the consequent higher force strength they may provide. Therefore, all these components have been analyzed in the worst-case scenario, mainly adopting clamped surfaces and avoiding considering the external incoming radiation hitting them externally for simplicity.

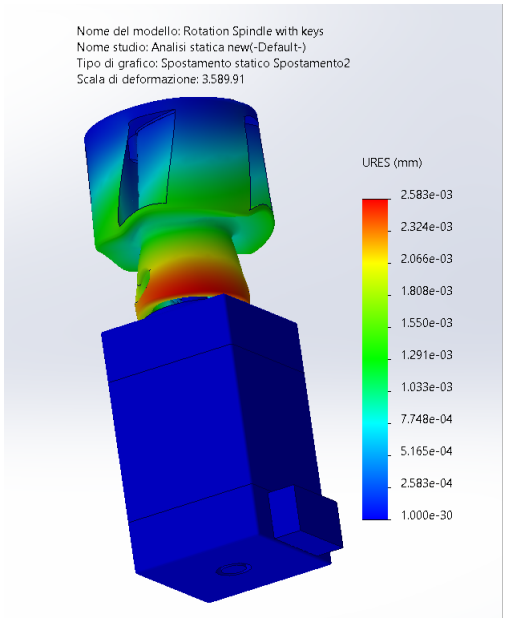

Figure 4.18: ***Spindle and electric motor equivalent displacements.***

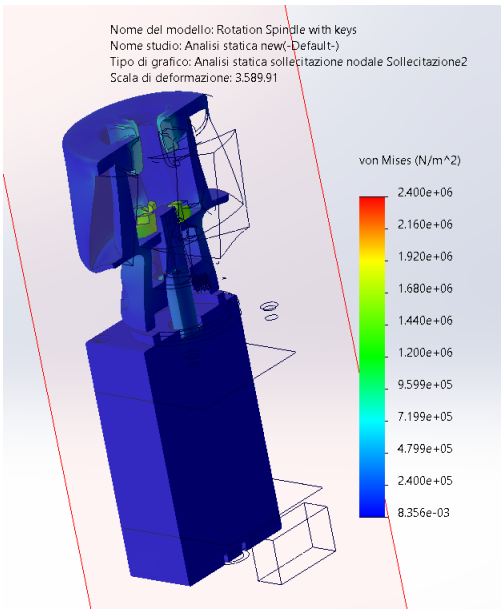

Figure 4.19: ***Spindle and electric motor von-Mises strains.***

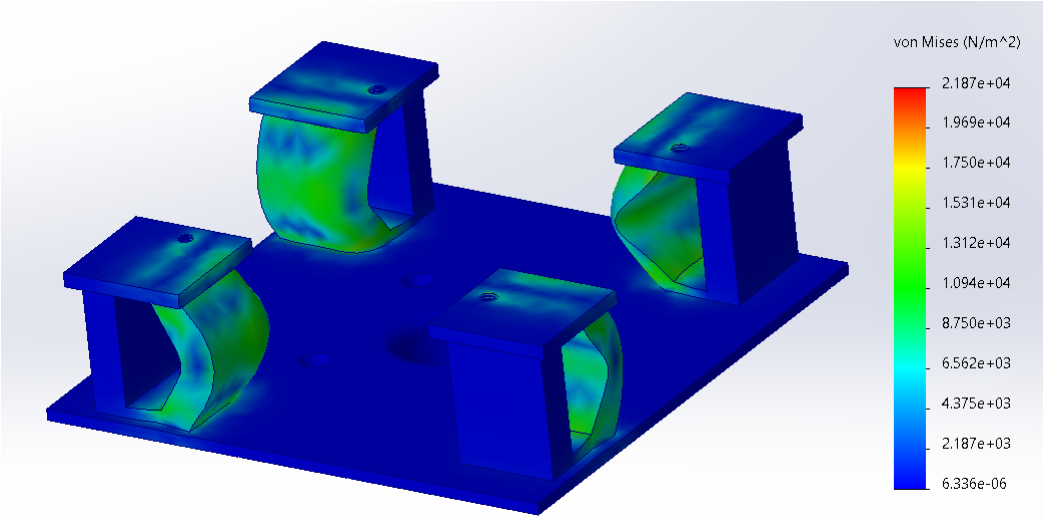

Figure 4.20: ***Booms' support plate equivalent strains due to constraints.***

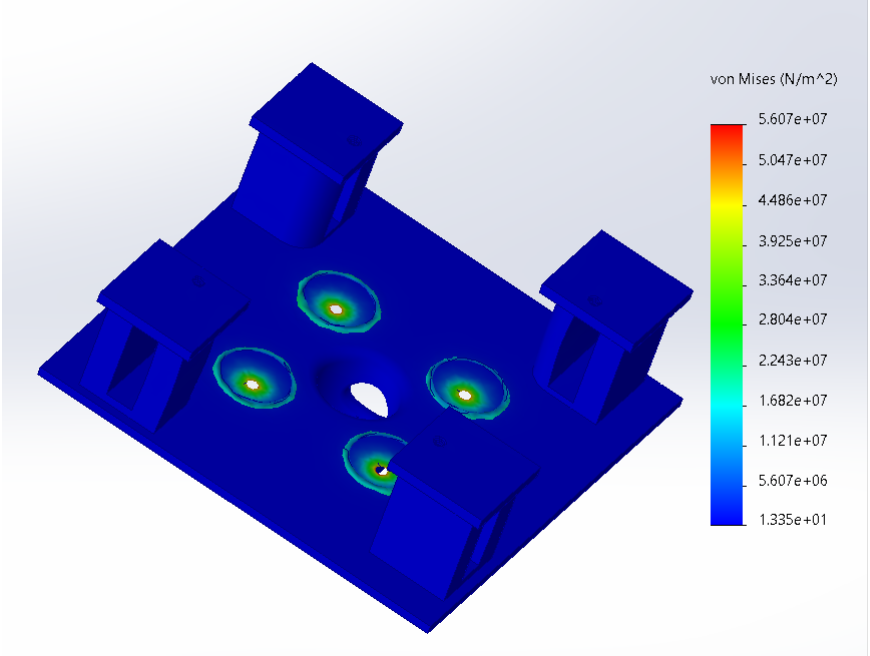

Figure 4.21: ***Booms' support plate equivalent strains due to screws.***

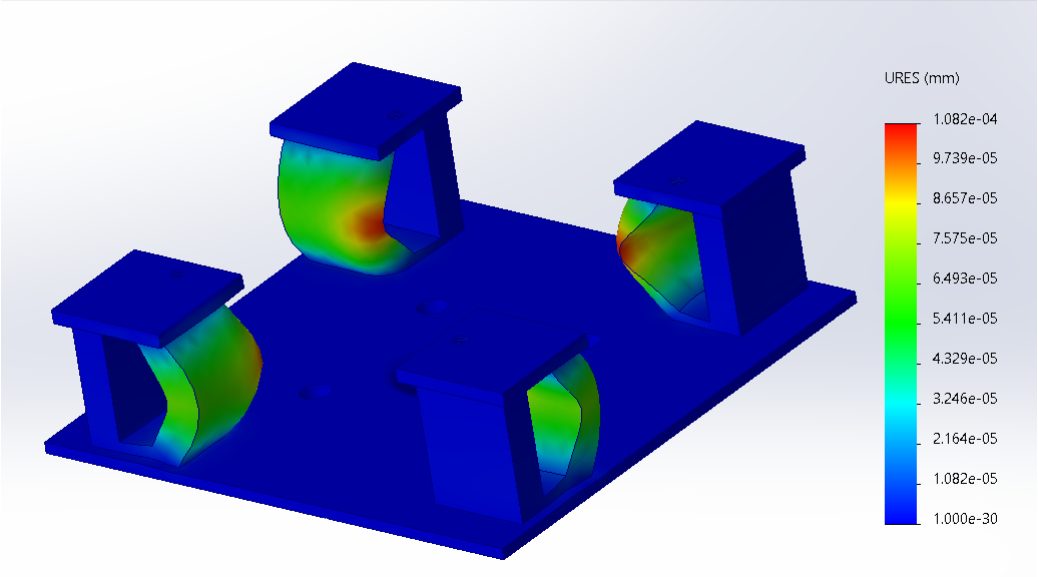

Figure 4.22: ***Booms' support plate displacements due to constraints.***

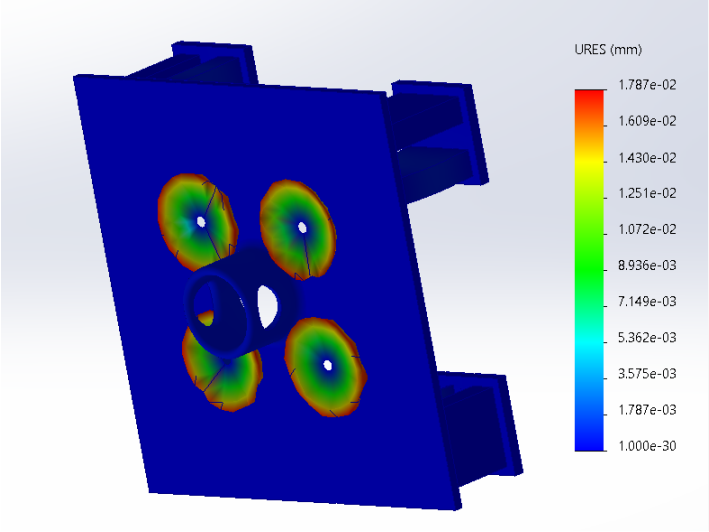

Figure 4.23: ***Booms' support plate displacements due to screws.***

4.3.2 Higher Assembly Static Analysis

Next simulations concern to study the interaction between rotating spindle and booms' support plate, trying to analyze the main differences that occur whenever taking the same constraints and assuming to put a local-interaction between the inner cylindrical surfaces they have in common. This would simulate the worse condition ever, in case of complete friction interference.

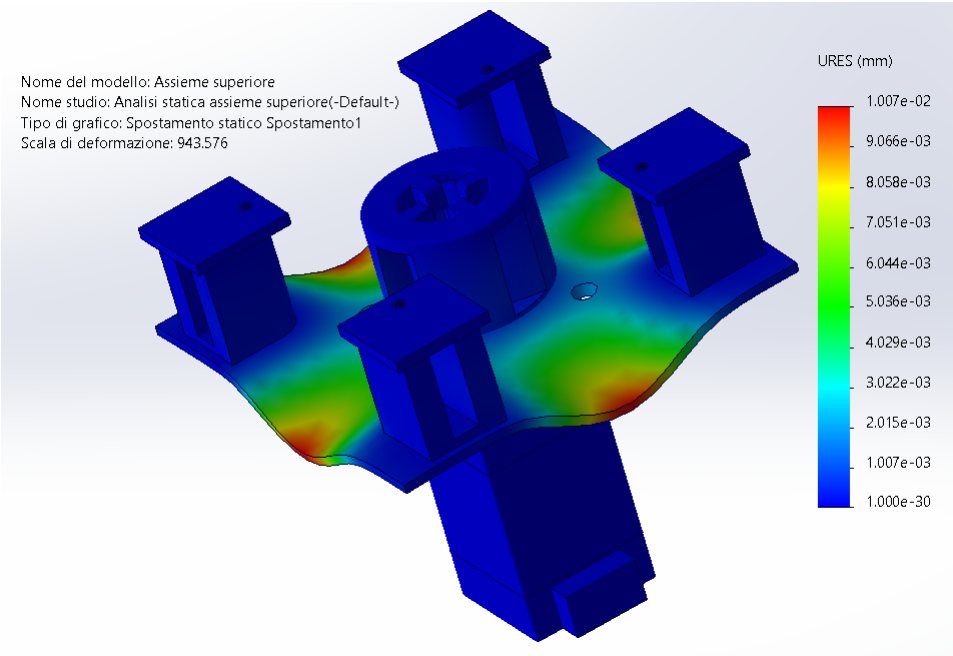

Figure 4.24: ***Higher assembly displacements.***

In **figure 4.24** the maximum displacements would locate between each couple of vertical supports, in proximity of their lower vertical widths. The newer maximum displacement has been reached in $10\mu m$ in magnitude, which is 100 times higher than of the single boom's plate one, hence achieving a truly higher solution once assuming a bad prototyping of designed components (for example due by the 3D printer accuracy). The maximum stress is achieved at $1.06 \cdot 10^6 \frac{N}{m^2}$, that should be less than 50 times more than of the boom's support plate. These stresses seem to go differently exchanging the contact pressure among the rotating spindle, **figure 4.25**, and increasing the central shaft's ones on its lower section. The tooth-shaped spindle's components result to be characterized by similar trends, demonstrated in **figure 4.26**.

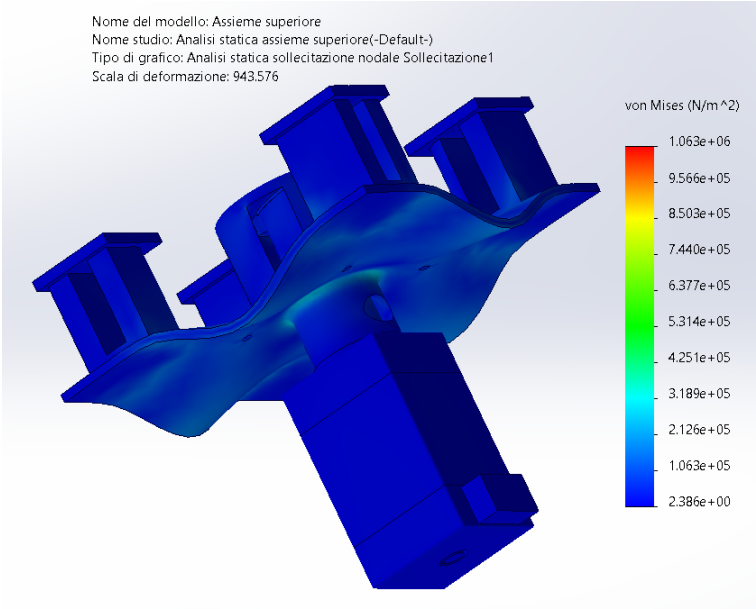

Figure 4.25: ***Higher assembly von-Mises stresses.***

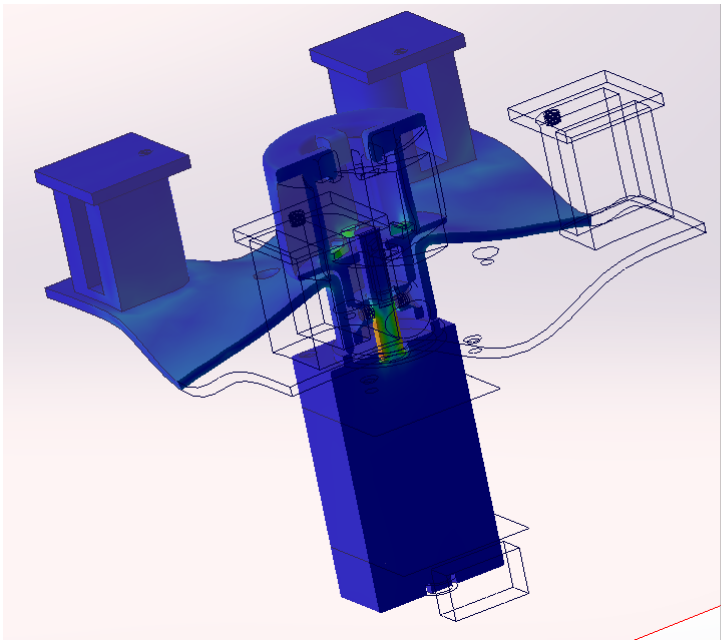

Figure 4.26: ***Higher assembly von-Mises internal stresses.***

In **figure 4.18**, it seems that the plate would absorb and distribute these stresses on an higher surface, reducing them to the only shaft. Each feather-key appears being unloaded and suffering very well the torque moving the electric motor's shaft.

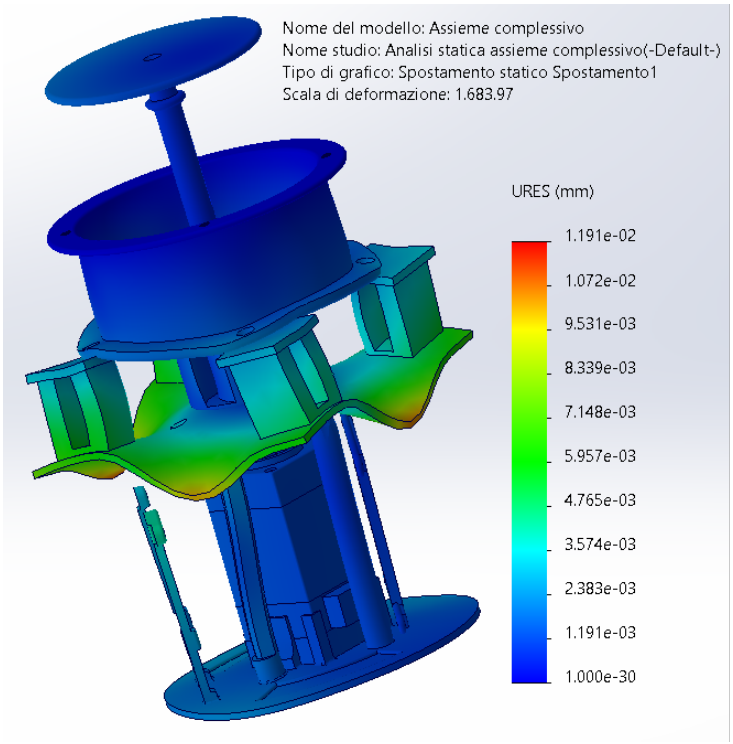

Figure 4.27: ***Overall frame assembly displacements.***

Moreover, it's been analyzed the global frame's behavior afterwords have inserted the lower electronics plate and the sail's stowage recipient in order to learn in which way the structure could resist to internal stresses, **figure 4.27**. The results should be similar and a bit higher to those proposed in **figure 4.24**, $12\mu m$ in magnitude, despite the booms' support plate would be more strained due to the upper sail's stowing component clamped by four higher *M3X3* screws. It's well observable a slight electronics' strain located on thin vertical supports on which there will be mounted required devices, with their magnitude being approximately $4\mu m$. What about constraints, this design is obtained clamping the electric motor to the lower electronics plate, then applying a local interference between this last and the booms' support plate and eventually making the same by connecting it to the upper sail's stowing plate. Before meshing the structure's frame, it should be necessary to simulate the mechanism connection to the CubeSat one by inserting an additional clamp on the higher surface characterized by the four holes. It can be useful to

pair obtained results to those from stresses, as immediately done approaching the von-Mises method:

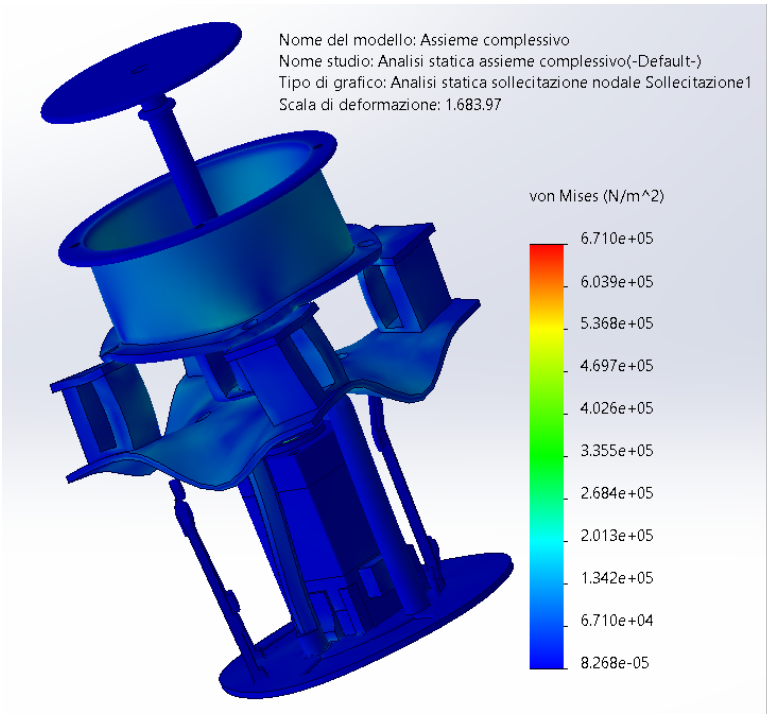

Figure 4.28: ***Frame assembly von-Mises stresses.***

Observing the mechanism's response from an higher point of view, it seems to have a quite-uniform strain distribution among all components involved. If trying to cut vertically the entire mechanism it could be observed a very similar behavior upon the inner shaft. The higher tooth-shaped spindle's interference parts, **figure 4.29**, will be much more stressed than of that located lower, hence an opposite case as in **figure 4.26**. Resuming, these results would reflect a practical frame's response due to the electric motor's rotating shaft, distributing as well its stresses mainly on central booms' support plate, whose higher and lower components increase the frame's maximum yield endurance to both efficiently counteract the global strain and theoretically to let the mechanism wrapping as wished.

4.3.3 Designing Materials

Most of components have been realized in *PLA/PHA* on the grounds of its availability, price and strength once paired to other plastic materials [**64**]. The lower electronics plate and feather-keys need an higher capable material for both functional prototyping and durable testing scenario, paired to a sufficient environmental

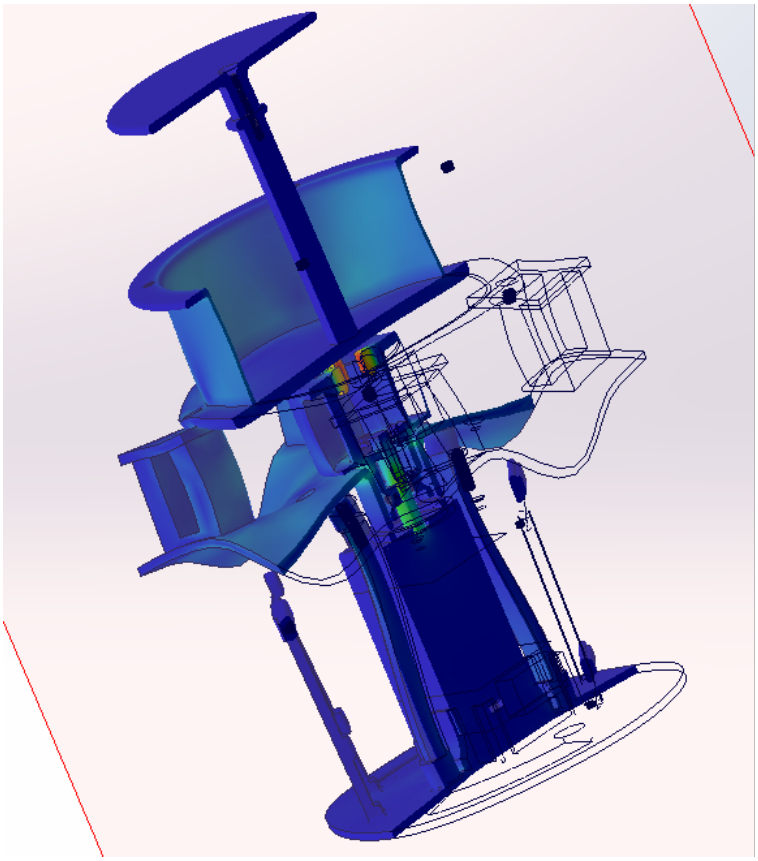

Figure 4.29: ***Internal assembly stresses.***

stability. *Nylon12* powder, [**65**], provided by *FormLabs*, suits pretty well for creating complex assemblies with minimal water absorption. This material could be also a better option for that components which may need a successful detail's level, but also letting the technician recycling up to 70 % of working wastes. *Nylon12* finished prints have been in general certified to absorb very little moisture and they result very resilient to light, heat and chemical agents. The electronics' plate needs to counteract as well the heat expelled by mounted devices. The feather-keys need a sufficient strength once paired to the electric motor and the rotating spindle, hence Nylon powder could enhance global performances. The *O*-rings, placed on each triangular-shaped foil vertex, are 3D-printed always using *Nylon12*, whose tensile-strength could suffer higher loads for avoiding to damage the sail on the meanwhile of its unfolding phase.

4.3.4 Spindle and Assembly Frequency Analysis

The modal analysis, [**66**], is a characterization technique of a system's dynamical behavior, in this case for obtaining the own frequencies to learn mechanism's dynamics and vibrational sequences. This method bases on a numerical approach of modal waves using both constraints and loads, acting like external stressing entities and internal ones like that provoked by measuring tapes' contact with booms' support plates.

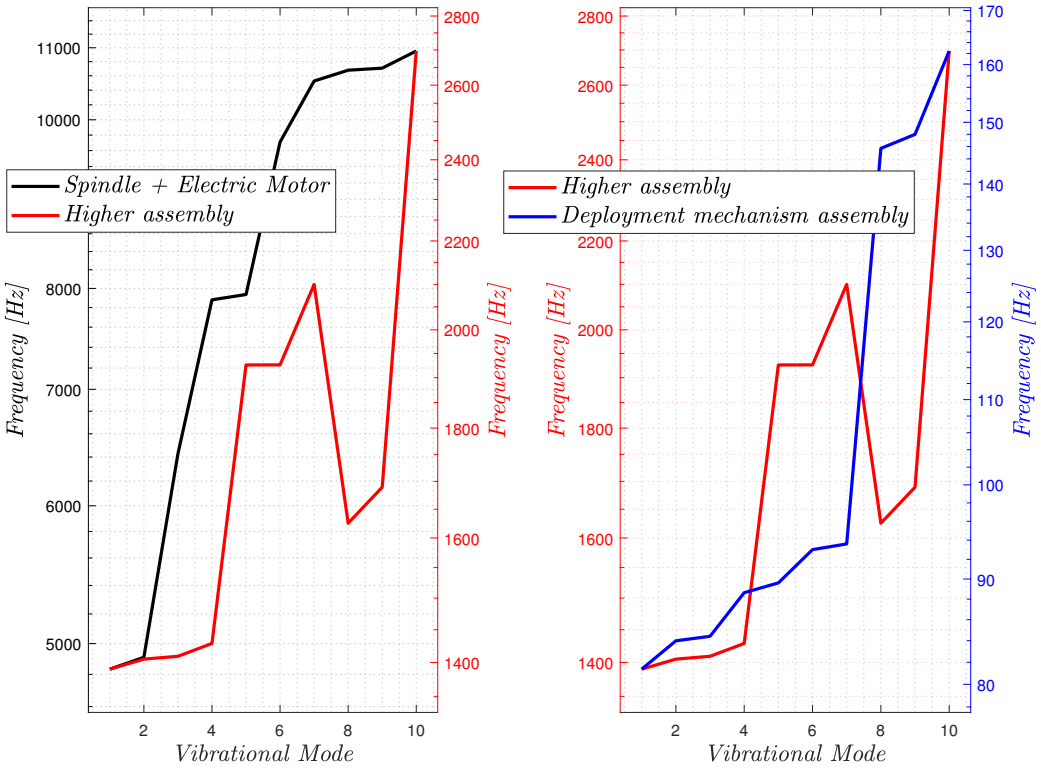

Figure 4.30: ***Frequencies against vibrational modes.***

There are retrieved the natural frequencies for several cases of study in which the purpose is to learn how stresses might propagate and which are main differences among their strains by applying *FEM*. *Solidworks* can provide the first 5/10 natural frequencies related to already introduced worse mechanical resonance responses, regarding that the electric motor should work with specific angular velocities comprehended between $100 \div 600$ rpm, which consists of a frequency-range of $1.67 \div 10.02$ Hz. It could be useful to avoid the matching between this and each of

the modal frequencies found afterwords.
The goal of this unit is to clarify what could modify to the mechanism's modeling whenever adding one more component to the deployment assembly, hoping to enhance its general attitude to suffer higher stresses induced by constraints and external loads. In **figure 4.31**, the first four modes result being comprehended in 4,932 to 15,133 Hz. What about the electric motor's response, the *AMPRES* [1] factor reflects the influence incidence of the single modal mode, in this situation decreasing going-up on frequencies. For instance, trying to add the rotating spindle to the previous pattern and adding several local interferences between components involved, most remarkable vibrational modes extend to the first six ones from 4,809.4 to 10,712 Hz. In opposition, the *AMPRES* factor should increase upon frequencies, thus it could be better working on lower trends and for achieving lower strains in time, **figure 4.32**. Moreover, referring to **figure 4.33**, vibrational response becomes even more worse once taking into account those frequencies due to assembly analysis. The first ten modes are ranged between 1,390 and 2,697 Hz, hence booms' support plate component doesn't improve the overall dynamical pattern, also bringing to quite-various increasing *AMPRES* factors, in which the worse obtaining ones are the second and the third. At last, by inserting the lower electronics' plate and the upper sail's stowing component, **figure 4.35**, the overall mechanism seems to behave well once the lowest resonance mode is achieved in 81.37 Hz, whereas the highest equal to 162.46 Hz, hence further from the working operative range calculated at first. The worst mode results being the ninth and all these solutions can demonstrate that most stresses would always refer to both electronics' vertical supports and mechanism's final hat. It's possible to state that all these natural frequencies reduce once adding other components to chosen/studied assembly, reflecting the higher system's capability to distribute as well stresses among supports paired one another, **figure 4.30**.
Eventually, vibrational-modes' trend are similar if taking the first and the third interpolated curves (black and blue), whereas the red one is characterized by a slight different behavior. In this way, these last modes initially increase with frequencies, then decreasing and at last increasing again. Electric motor's shaft frequencies result being far from that obtained for the overall assembly, hence rejecting any chance of resonance.

[1]The Amplitude Response values, for a modal analysis, reflects the relative pattern strain related to a specific vibrational mode. Although It hasn't a physical measurement unit, its value provides a way for how much the meshed structure deflect. In particular, it can be useful whenever making a comparison between all involved modal modes, in which if the system is excited to a frequency lower *AMPRES*, the structural response would be more contained and less problematic. An higher *AMPRES* would bring to higher strains and an increasing potential resonance risk, and vice versa.

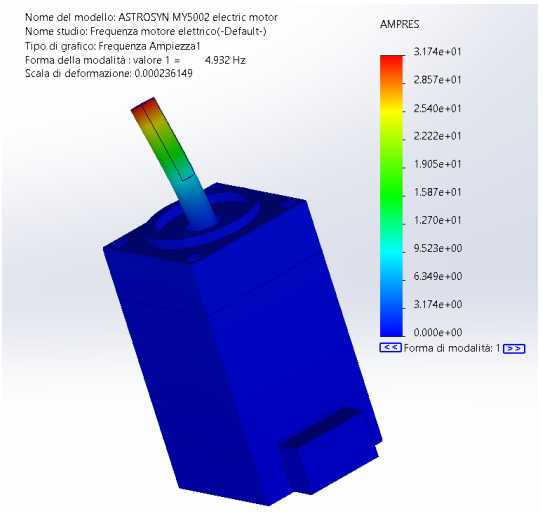

(a) 1^{st} ***vibrational mode.***

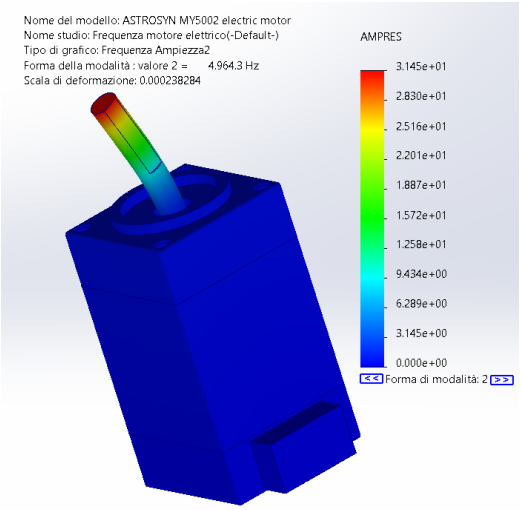

(b) 2^{st} ***vibrational mode.***

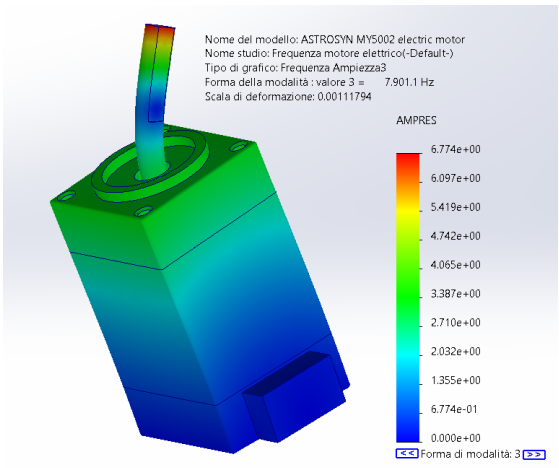

(c) 3^{st} ***vibrational mode.***

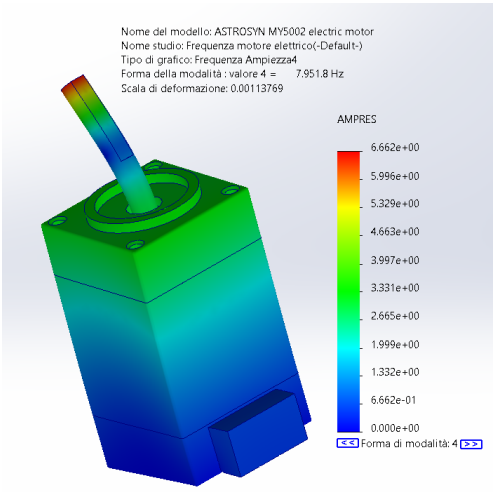

(d) 4^{st} ***vibrational mode.***

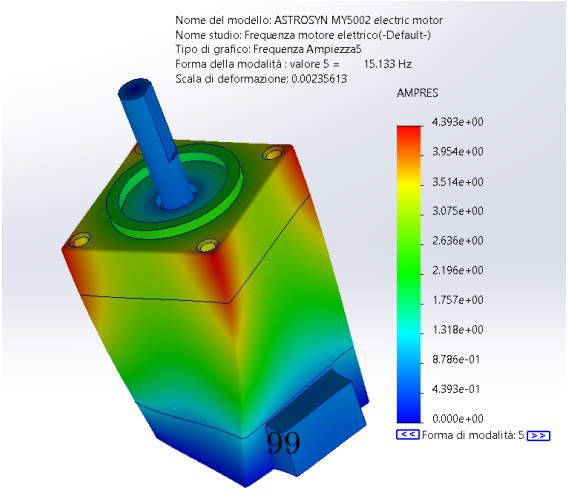

(e) 5^{st} ***vibrational mode.***

Figure 4.31: ***Electric motor vibrational modes.***

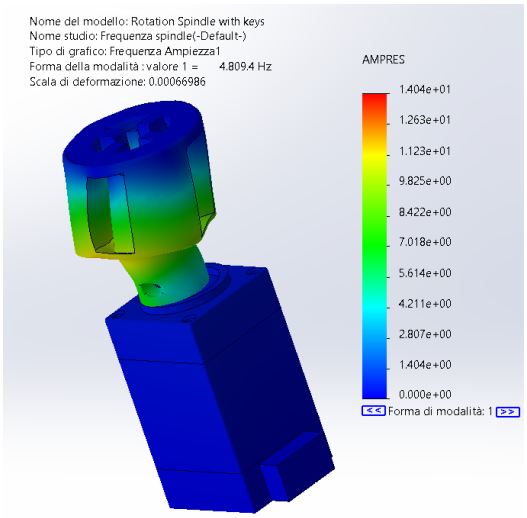

(a) 1^{st} ***vibrational mode.***

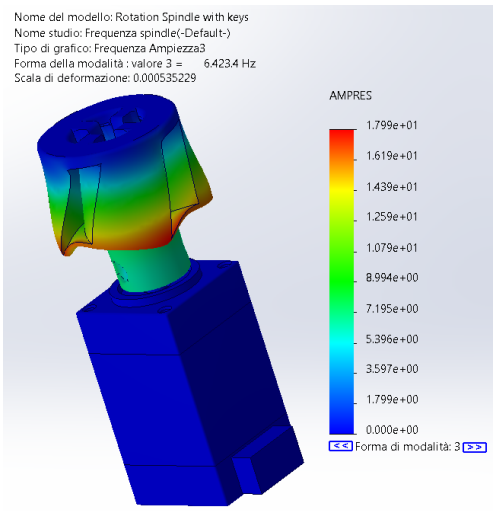

(b) 3^{st} ***vibrational mode.***

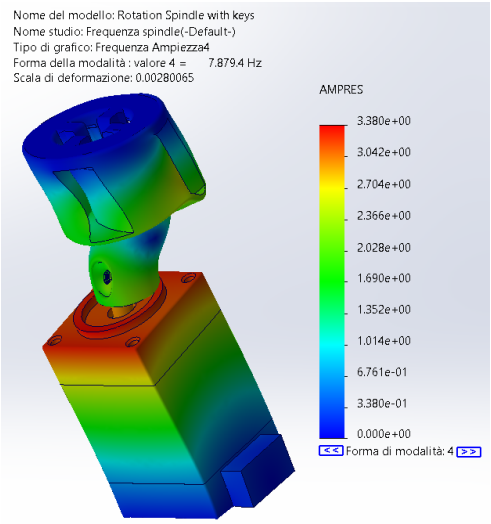

(c) 4^{st} ***vibrational mode.***

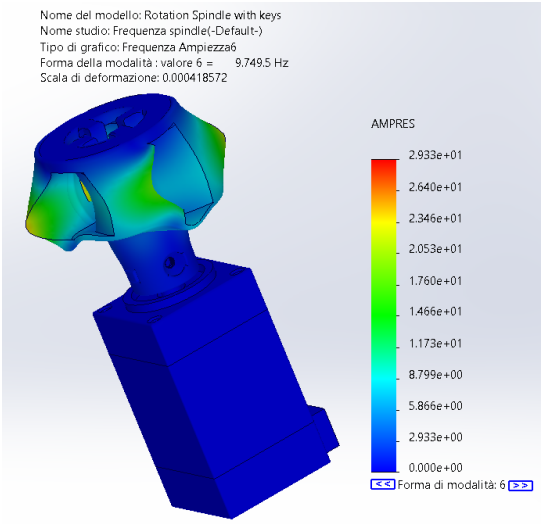

(d) 6^{st} ***vibrational mode.***

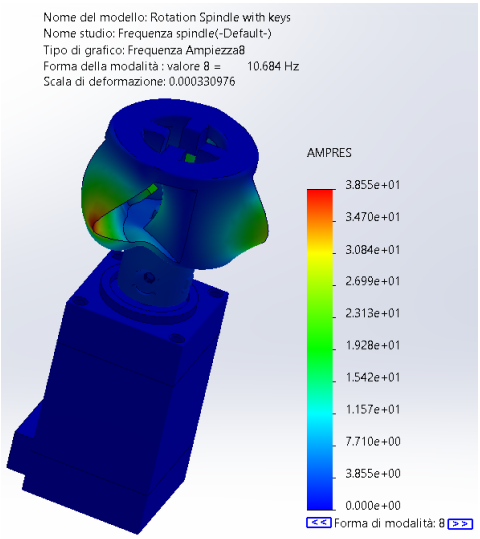

(e) 8^{st} ***vibrational mode.***

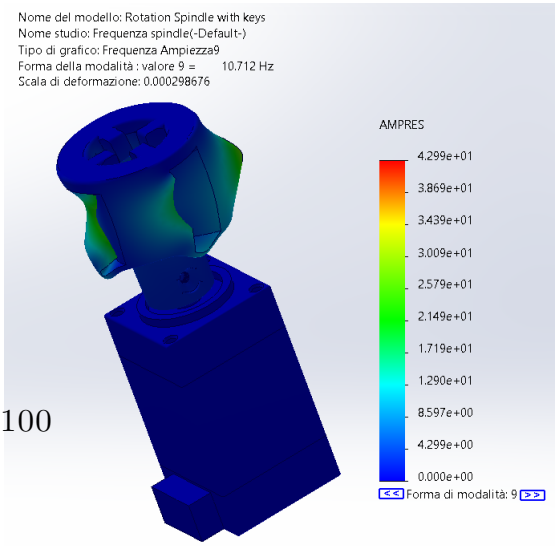

(f) 9^{st} ***vibrational mode.***

Figure 4.32: ***Electric motor and spindle vibrational modes.***

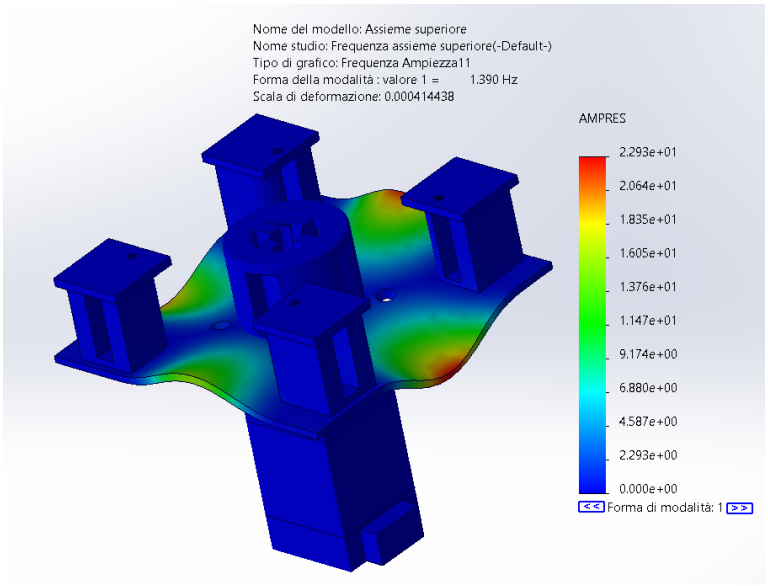

(a) ***Higher assembly*** 1^{st} ***mode.***

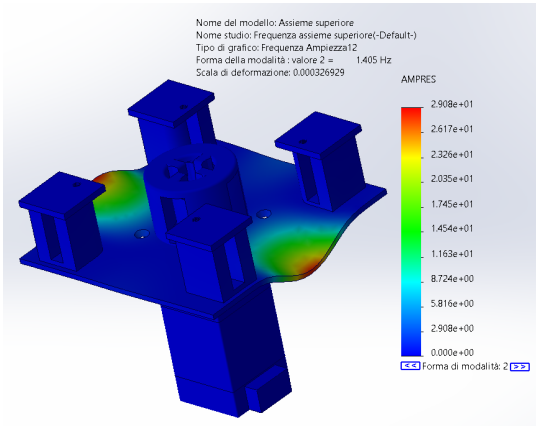

(b) ***Higher assembly*** 2^{st} ***mode.***

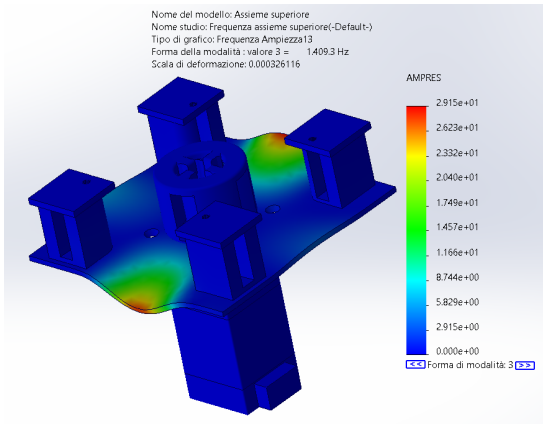

(c) ***Higher assembly*** 3^{st} ***mode.***

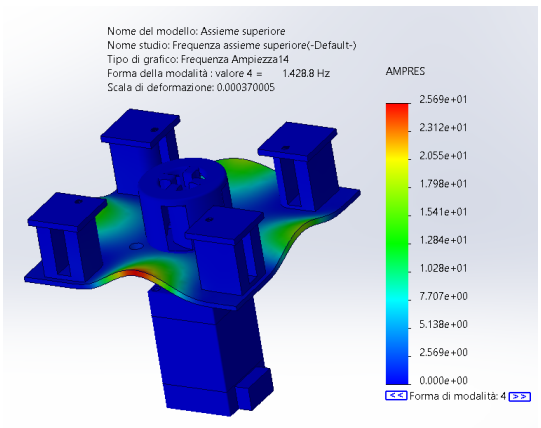

(d) ***Higher assembly*** 4^{st} ***mode.***

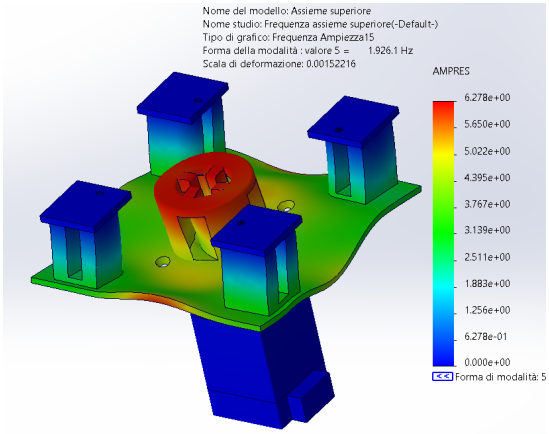

(e) ***Higher assembly*** 5^{st} ***mode.***

Figure 4.33: ***First five higher assembly modes.***

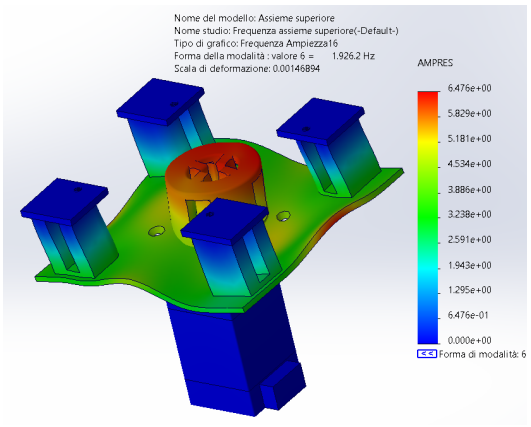

(a) ***Higher assembly*** 6^{th} ***mode.***

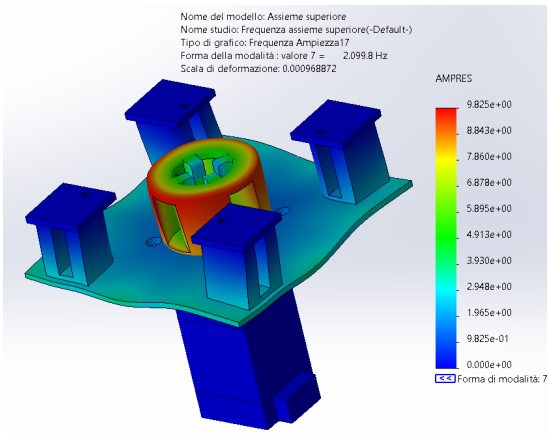

(b) ***Higher assembly*** 7^{th} ***mode.***

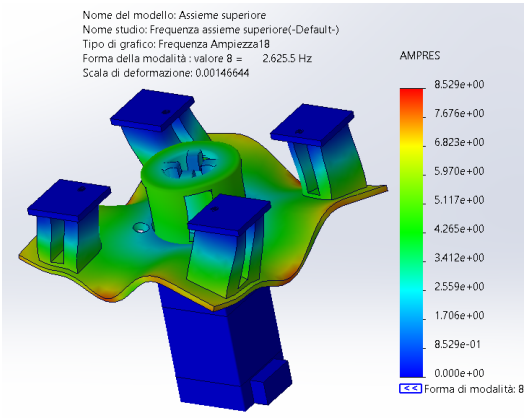

(c) ***Higher assembly*** 8^{th} ***mode.***

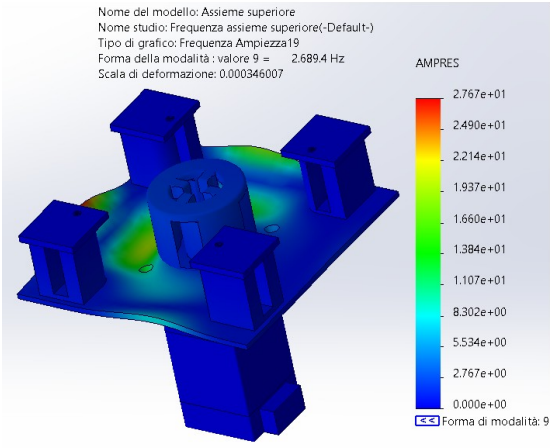

(d) ***Higher assembly*** 9^{th} ***mode.***

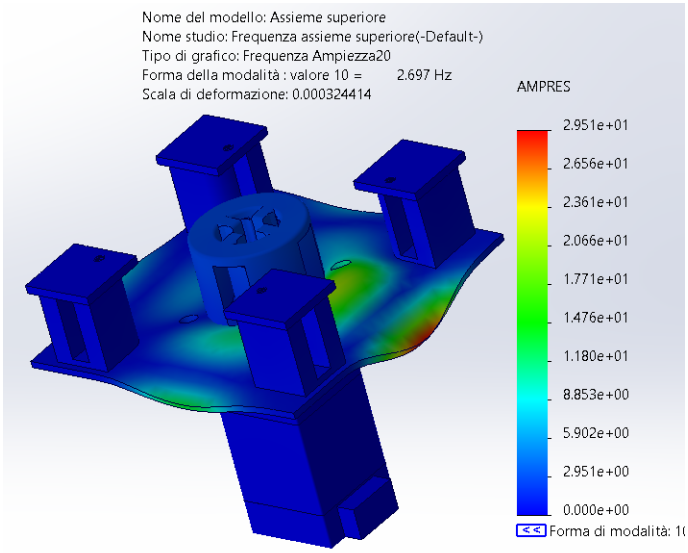

(e) ***Higher assembly*** 10^{th} ***mode.***

Figure 4.34: ***Last five higher assembly vibrational modes.***

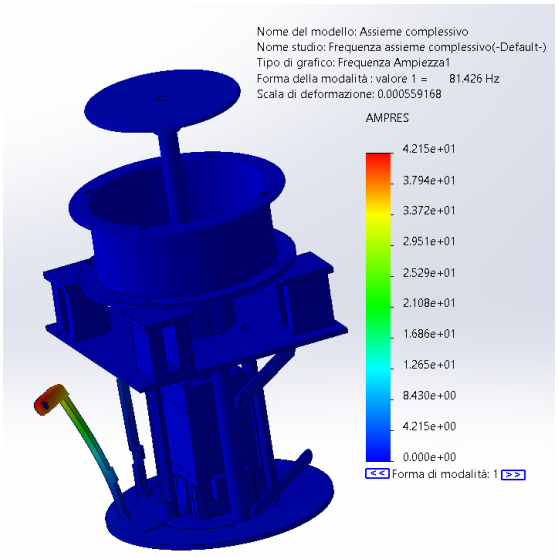

(a) ***Assembly*** 1^{st} ***vibrational mode.***

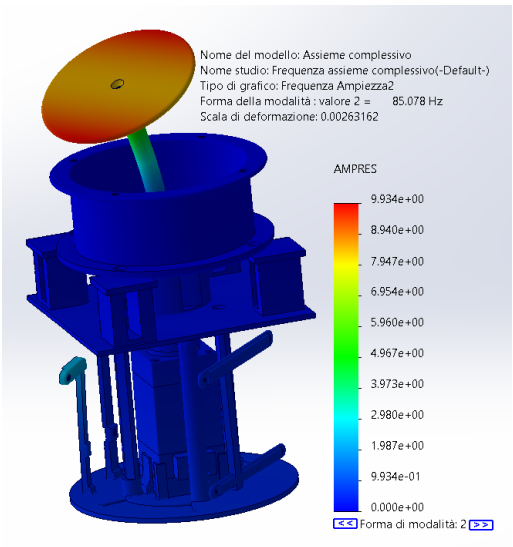

(b) ***Assembly*** 2^{st} ***vibrational mode.***

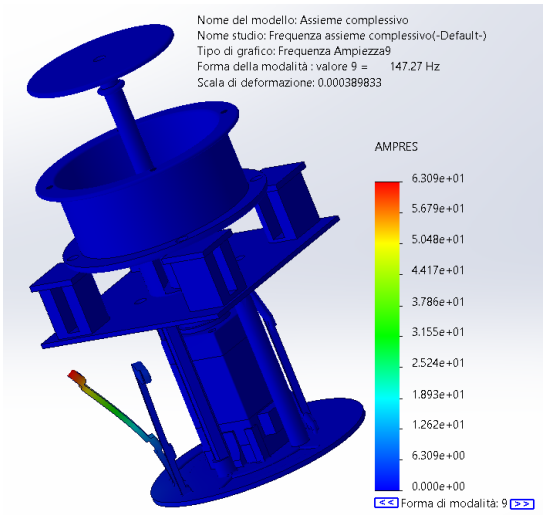

(c) ***Global assembly*** 9^{st} ***vibrational mode.***

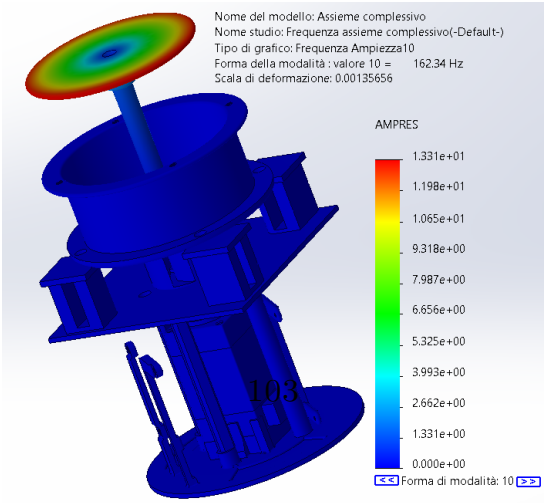

(d) ***Global assembly*** 10^{st} ***vibrational mode.***

Figure 4.35: ***Global assembly vibrational modes.***

4.4 Solar Sail Prototyping

Deployment mechanism realization requires to design the sail for imagined mission scenario, taking as reference what concerns about *CubeSail* mission [**67**]. It's necessary to take 4 emergency thermal blankets, 12 microns in width, whose core is made in Mylar and covered by Alluminium. The material's choice is based on both optical and mechanical properties at the grounds of typical features researched for several solar sail missions.

Figure 4.36: ***Four sections of triangular foils.***

The main issue conceives typical widths' ranges that can be described comprehended between $3 \div 4\mu m$, despite commercialized ones around 12 μm. This sail' sizing parameter regards both available spaces and industrial complexity development. Applied trade-offs refer to a 1:3.8 scaling model of deployed solar sail for proving that its initial stowed configuration could be inserted inside a truly small volume completely decoupled to internal CubeSat subsystems.

The first step regards to look for the best folding origami pattern for reducing both the sail's transverse and longitudinal sizes w.r.t. the vertical support connecting the lower stowage plate to its higher hat **figure 4.9**. The adopted technique consists of

(a) ***Needed tools and devices.***

(b) ***First sail folding-frame.***

(c) ***Secondary sail folding-frame.***

(d) ***Increasing compactness phase.***

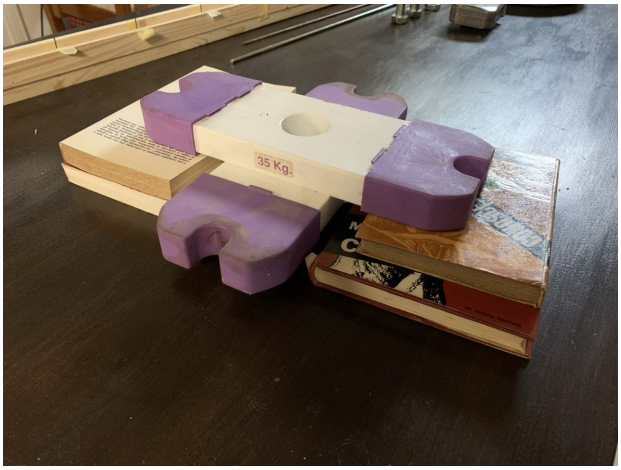

(e) ***Sail's rest under weights.***

Figure 4.37: ***Phases of physical realization.***

realizing a 3 meters wooden-long bar by using 24 pins as longitudinal guide to fold correctly the sail, depicted in **figure 4.37** and **4.38**. In this way, the developer may only move from right to left alternatively the sail putting a long metal-strip inside the C-section horizontal bar laid on a table, this for working both raised by floor and comfortably. The sail has been realized using an adhesive spray between thermal blankets' foils, assuring to give them enough time to dry and letting them

Figure 4.38: ***Detailed wooden-support guideline.***

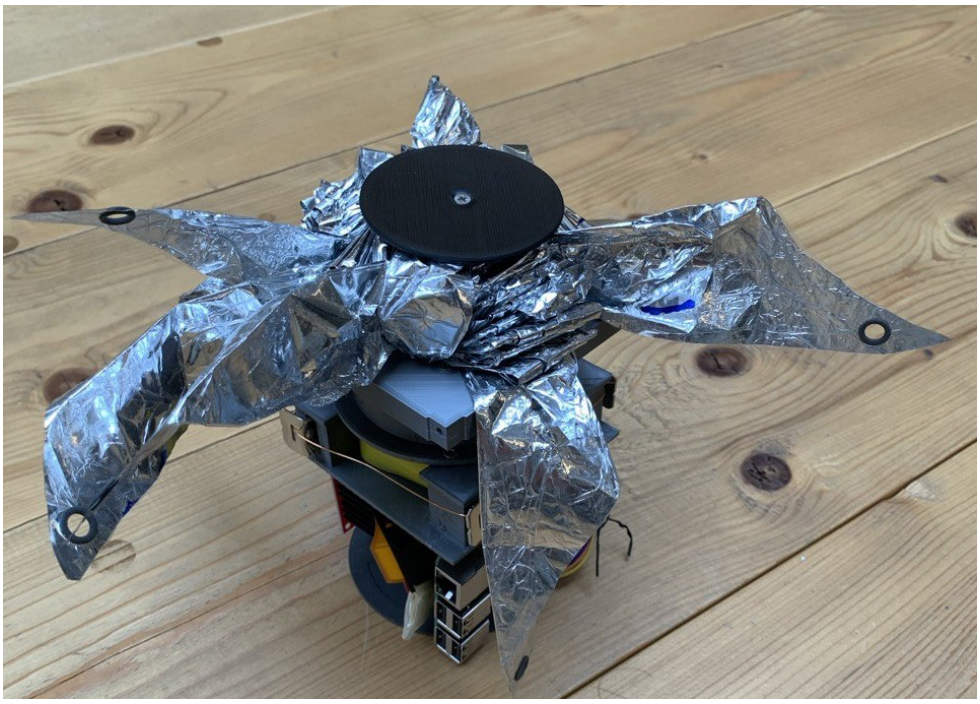

Figure 4.39: ***Deployment mechanism assembly with folded solar sail.***

to rest in a comfortable place and adequate moisture's levels. The tweezers' chest is needed to avoid the already folded sail's sections to 'escape' from wooden guideline and, once finished this process, heating it to increase its compactness by using an industrial dryer.

The volume left available by solar sail's stowing support is approximated to 7 cm in height and 3.5 cm in width, hence the folding technique results to fit well for packaging each triangular shape inside it correctly. Two 35 Kilos weights, **figure 4.37**, may be sufficient to replace all clamps, waiting to complete each of the four sail's triangular-shape foils through a cutter and a 410 cm ruler in length (built by using two similar plastic L-shaped bars bound by adhesive tapes for simplicity).

The final assembly consists of placing each foil inside the empty-left volume and adding 8 distinguished *Nylon12* rings connected to each ending hook through copper-wires, once radially deploying all booms, **figure 4.39**. These circular-designed rings aim to avoid solar sail's strains and tears during of unfolding, distributing uniformly all tensile loads induced by the electric motor's shaft.

4.5 Electric Circuit Logic

The electric mini-hybrid stepper motor, **figure 4.41**, works through continuous 1.8 stepped angles through an *L298N driver* device, whose command inputs come from using a *Raspberry Pi 3b+*. Afterwords have been chosen specific *GPIO* pins from this last device, the command input has been chosen adopting a remote control logic, this in order of avoiding to interfere with the sail's deployment and letting the user decide whenever either interrupting the unfolding process or wrapping it.

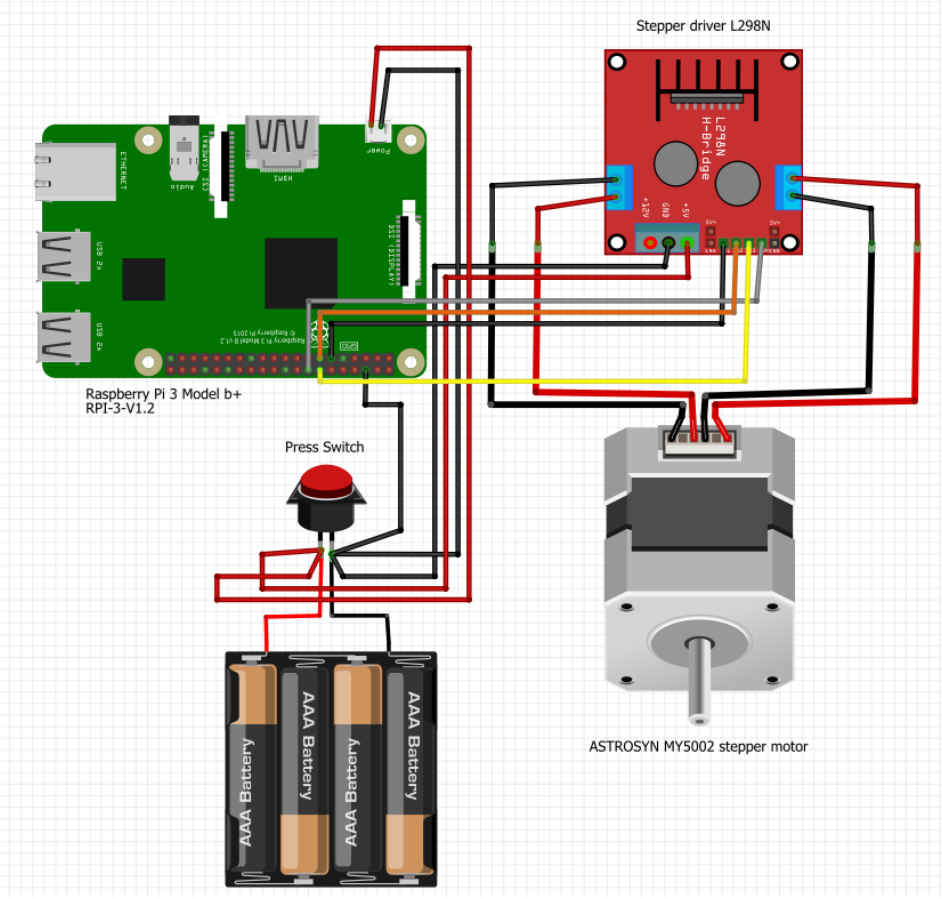

Figure 4.40: ***Electric circuit devices and wires.***

This passage has been let possible only using a device capable to interconnect the Raspberry Pi to the user's wills, hence taking a *GAMESIR Joystick controller* and connecting its *USB-Dongle* inside one of the computer's inputs (Type C), then downloading the libraries necessary to write manually the Python codes, directly on command-prompt, for implementing this logic circuit.

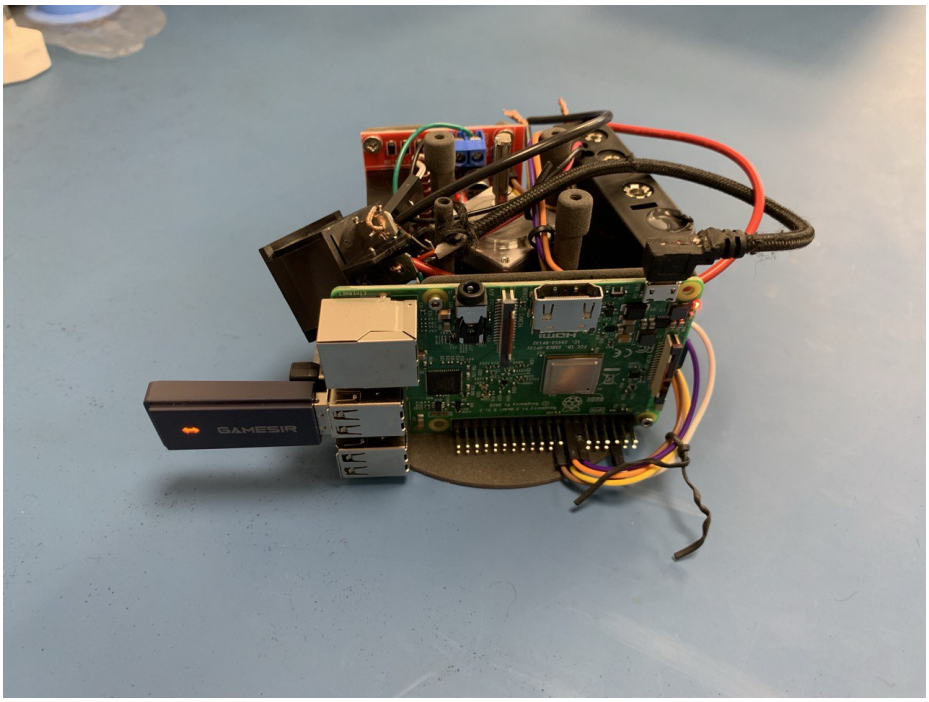

(a) ***Raspberry Pi, jumpers and joystick USB dongle in detail.***

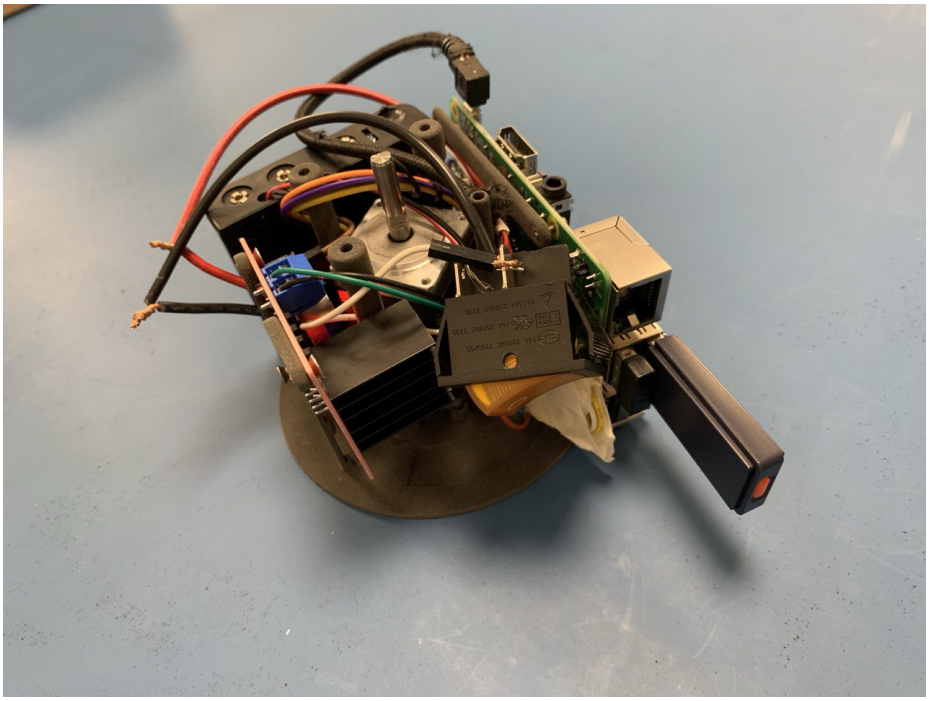

(b) ***Switch, batteries, stepper driver and electric motor in detail.***

Figure 4.41: ***Lower electronics plate assembly.***

Raspberry Pi and the stepper driver L298N have been connected to the same power supplier of 6 V (logically lower to the system's power source), **figure 4.40** and **4.41**, eventually regulating their activating phase manually by taking a *rocker-switch*. These functional aspects require both Bluetooth Mouse and Keyboard for the initial Controller setting, hence these aren't necessary for deploying the booms because directly given by the Joystick. The electric motor will be able to describe two specific rotations: the first clockwise and the second counterclockwise pushing on the **X** and **Y** buttons respectively. The first outputted code, shown in **figure 4.42**, is the command-prompt output given by the Python code, requiring inputting a generical number of steps (either positive or negative). This code is written to verify the electric motor could work properly inside the mechanism, although it isn't optimized for controlling it remotely yet.

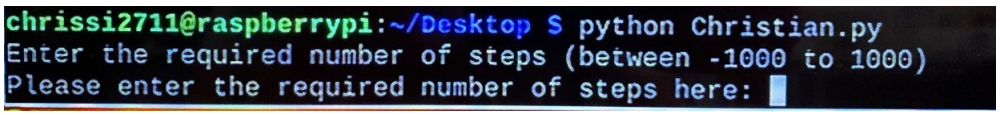

Figure 4.42: ***First Python code user interface.***

The third outputted Python code, **figure 4.43**, would let the user to release and press multiple times on previous joystick buttons, updating quicker this step-change after selecting a very low *'sleep-count'* value, which is essential to assure reactivity and command readiness. The interface window automatically update to all zeros once releasing, or not pressing outlined buttons. The choice of the best fitting

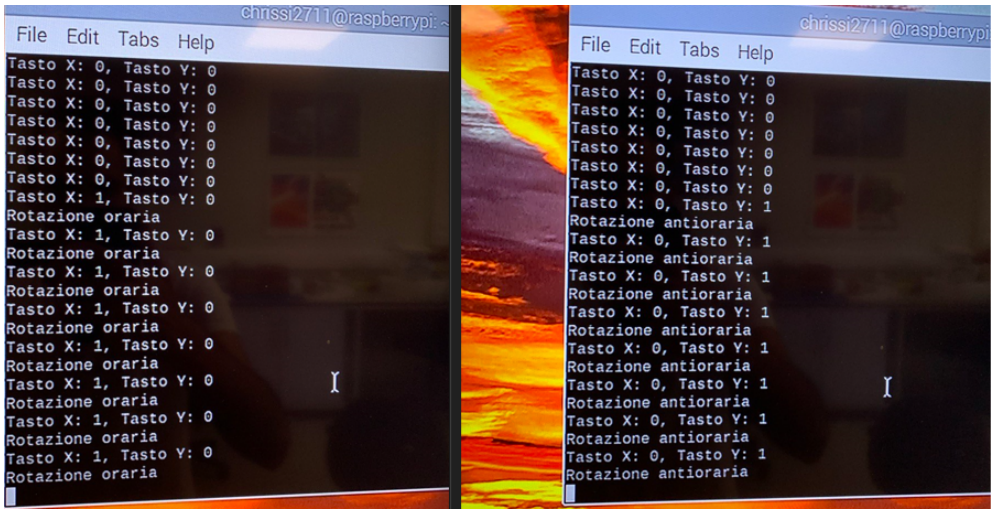

Figure 4.43: ***Third Python code user interface.***

electric motor focuses on provided maximum torque, mass, geometry coupled to

electronics devices, availability and price. The maximum torque has been studied making simple calculations about involved Inertia momenta for both fully stowed and deployed measuring tapes w.r.t. the plate and rotating spindle's vertical axis. The total mass characterizing the spindle's endurance to describe a counterclockwise orientation depends also on measure-tapes contribute. The shaft's arm, necessary to estimate needed torques, depend on measuring-tapes' initial and final deploying radius lengths, whose results are paired to literature *datasheets* for confirming electric motors' functionalities. The maximum rotational speed and the voltage supply aren't considered on these preliminary analysis, despite the second one may be lower than provided potential-difference given by both solar-panels and battery charge capacities summed effects.

Property	***Value***
Poor	(1)
Below average	(2)
Average	(3)
Above average	(4)
Excellent	(5)

Table 4.7: ***Decision matrix property values.***

It's necessary to underline that the idea on the ground of the electronics plate

Device series	***Max Torque***	***Max rot. speed [rpm]***
PEL00883	261 [gcm] (3)	19500 (-)
MY5002	9 [Ncm] (5)	N/A (-)
MY180	0.53 ÷ 0.75 [Nm] (5)	N/A (-)
517598	15.6 [mNm] (3)	11000 (-)
986D41 series	4923 [gcm] (5)	4289 (-)
950D series	78.4 [gcm] (5)	9869 (-)
Noise-attenuated	110 [gcm] (2)	5950 (-)
1271-12-188 series	14 [Ncm] (5)	9 (-)

Table 4.8: ***Electric motor's decision matrix, [68], [69], [70], [71].***

modeling was displacing that devices in order to reduce as more the wires' connections in order to define a very compact system. In addition to it, there were been inserted several plastic spacers to enhance the thermal exchange and avoiding

overheating issues, mainly due to the L298N stepper-driver and Raspberry Pi 3b+, encountered for long-lasting usages.

Mass [g]	***Manufacturer***
140 (3)	*PRO-ELEC*
200 (3)	*ASTROSYN*
650 (1)	*ASTROSYN*
80 (5)	*MAXON-MOTOR*
1070 (1)	*MFA/Como-Drills*
160 (3)	*MFA/Como-Drills*
110 (4)	*MFA/Como-Drills*
55 (5)	*MCLENNAN*

Table 4.9: ***Manufactured masses decision matrix.***

The sizing column of last decision matrix comprehend two different property values' typologies. *"Empty"* stands for free-volumes' matching between support plates and electric motor, whereas *"electronics"* is referred to wires and other devices' coupling, reducing interferences as more to bring higher compactness.

Sizing (empty/electronics) [mm]	***Voltage supply [V]***	***Costs [£]***
50 X 35.6 X 35.8 (2+3)	5 ÷ 12 (-)	5.59 (5)
74 X 28 X 28 (4+5)	5 ÷ 12 (-)	34.25 (3)
57 X 51 X 81 (2+2)	16.8 (-)	40.27 (3)
45 X 30 X 27 (2+3)	5 ÷ 12 (-)	135 (1)
114.5 X 51.8 X 51.8 (1+1)	5 ÷ 12 (-)	78.09 (2)
86 X 35 X 27.6 (2+2)	5 ÷ 12 (-)	18.05 (4)
64 X 30 X 27.5 (3+4)	5 ÷ 12 (-)	4.50 (5)
46 X 27 X 27 (2+3)	5 ÷ 12 (-)	25.50 (3)

Table 4.10: ***Functional decision matrix.***

Decision matrices confirm with 20 points that *ASTROSYN MY5002* electric motor results being the best choice for considered designing requirements.

4.5.1 Electric Motor Python Codes

On command-prompt were been installed three different libraries, in particular *time*, the *General Purpose Input/Output GPIO* and *pygame*. The third one is that associated to the Joystick controller, whereas the other two were been already installed onto *SanDisk microSD*.

Algorithm 1 ***Linear_Actuator.py: direct electric motor control***

import RPi.GPIO as GPIO
import time
Raspberry PI 3b pins' reading → GPIO.setmode(GPIO.BOARD)
No warnings → GPIO.setwarnings(False)
GPIOs could be chosen as preferred, define the four Pins with respective identifiers.
    → IN_1, IN_2, IN_3 and IN_4 = [13,15,16,18].
Set the output modes: GPIO.setup(IN_i, GPIO.OUT).
Define the rotation sequences with respect to step and working with boolean variables:
if step == 1: **then**
    GPIO.output(IN_i = ***True***, ***False***, ***False***, ***False***)
end if
if step == 2: **then**
    GPIO.output(IN_i = ***False***, ***False***, ***True***, ***False***)
end if
if step == 3: **then**
    GPIO.output(IN_i = ***False***, ***True***, ***False***, ***False***)
end if
if step == 4: **then**
    GPIO.output(IN_i = ***False***, ***False***, ***False***, ***True***)
end if
Time-to-sleep definition (command-prompt updating ratio): time.sleep(0.03)
def main():
print("Enter the required number of steps (between -1000 to +1000)")
total_steps = ***int***(***input***("Please enter the required number of steps here: "))
if $0 < total\_steps \leq +1000$: **then**
    for i in ***range***(1, total_steps + 1): **do**
        step = (i + 4)
        if step == 0: **then**
            step = 4
        end if
        rotate(step)
    end for

```
33: end if
34: if −1000 < total_steps < 0: then
35:     for i in range(total_steps, 0): do
36:         step = abs(i - 4)
37:         if step == 0: then
38:             step = 4
39:         end if
40:         rotate(step)
41:     end for
42: end if
43: GPIO.cleanup()
44: if ___name___ == "___main___": then
45:     main()
46: end if
```

The second code is necessary to verify and prove the connection between the *Raspberry Pi 3b+* and Joystick controller.

Algorithm 2 ***Bluetooth Controller_connection.py testing***

```
1: import pygame
2: pygame.init()
3: joystick = pygame.joystick.Joystick(0)
4: joystick.init()
5: Verify if buttons react to user's press. The command-prompt will show a
   continous updating window.
6: try:
7: while True: do
8:     pygame.event.pump()
9:     for i in range(joystick.get numaxes()): do
10:        print(f" Axis {i}: {joystick.get_axis(i) } ")
11:    end for
12:    for i in range(joystick.get_numbuttons()): do
13:        print(f" Button {i}: {joystick.get_button(i) } ")
14:    end for
15:    pygame.time.wait(100)
16: end while
17: except KeyboardInterupt:
18:    print("Ended by the User")
19: finally:
20:    GPIO.cleanup()
21:    pygame.quit()
```

Algorithm 3 ***Motor_working.py running simulation***

1: ***import*** RPi.GPIO as GPIO
2: ***import*** pygame
3: ***import*** time
4: IN_1, IN_2, IN_3 and IN_4 = [13,15,16,18] to stepper driver L298N
5: GPIO.setmode(GPIO.BOARD)
6: GPIO.setup(IN_i, GPIO.OUT)
7: Define both possible rotation sequences using the Boolean algebra expressed as HIGH and LOW variables, directly readable by the electric motor:
8: step_sequence_clockwise = [
9: GPIO.HIGH, GPIO.LOW, GPIO.LOW, GPIO.LOW),
10: GPIO.LOW, GPIO.LOW, GPIO.HIGH, GPIO.LOW),
11: GPIO.LOW, GPIO.HIGH, GPIO.LOW, GPIO.LOW),
12: GPIO.LOW, GPIO.LOW, GPIO.LOW, GPIO.HIGH),
13:]
14: step_sequence_counterclockwise = [
15: GPIO.LOW, GPIO.LOW, GPIO.LOW, GPIO.HIGH),
16: GPIO.LOW, GPIO.HIGH, GPIO.LOW, GPIO.LOW),
17: GPIO.LOW, GPIO.LOW, GPIO.HIGH, GPIO.LOW),
18: GPIO.HIGH, GPIO.LOW, GPIO.LOW, GPIO.LOW),
19:]
20: ***def*** step_motor(direction, delay=0.03):
21: **if** direction == "clockwise": **then**
22: step_sequence = step_sequence_clockwise
23: **end if**
24: **if** direction == "counterclockwise": **then**
25: step_sequence = step_sequence_counterclockwise
26: **end if**
27: **for** step in step_sequence: **do**
28: GPIO.output(IN_i, step[0,1,2,3])
29: time.sleep(delay)
30: **end for**
31: pygame.init()
32: joystick = pygame.joystick.Joystick(0)
33: joystick.init()
34: joystick_count = pygame.joystick.get_count()
35: **if** joystick_count == 0: **then**
36: ***print("No detected Controllers")***
37: pygame.quit()
38: GPIO.cleanup()
39: ***exit()***

```
40: end if
41: print(f"Controller connected: {joystick.get_name()}")
42: try:
43: while True: do
44:     pygame.event.pump()
45:     X = joystick.get_button(3)
46:     Y = joystick.get_button(4)
47:     print(f"Button X: {X}, Button Y: {Y}")
48:     if X and not Y then
49:         print("Clockwise rotation")
50:         step_motor("clockwise", delay=0.03)
51:     end if
52:     if Y and not X then
53:         print("Counterclockwise rotation")
54:         step_motor("counterclockwise", delay=0.03)
55:     else
56:         GPIO.output(IN_i, GPIO.LOW)    →    switch-off the electric motor if
    not pressing.
57:     end if
58:     time.sleep(0.001)
59: end while
60: except KeyboardInterrupt:
61:     print("Ended by the User")
62: finally:
63:     GPIO.cleanup()
64:     pygame.quit()
```

4.5.2 Stepper Motor Key-Findings

An electric motor is always needed whenever designing a mechanism having one/-more moving mechanical parts, hence the problem reduces to clarify the main motifs on the grounds of learning how an hybrid-stepper motor works, **figure 4.44**: These could be resumed as follows, [**72**] and [**73**]:

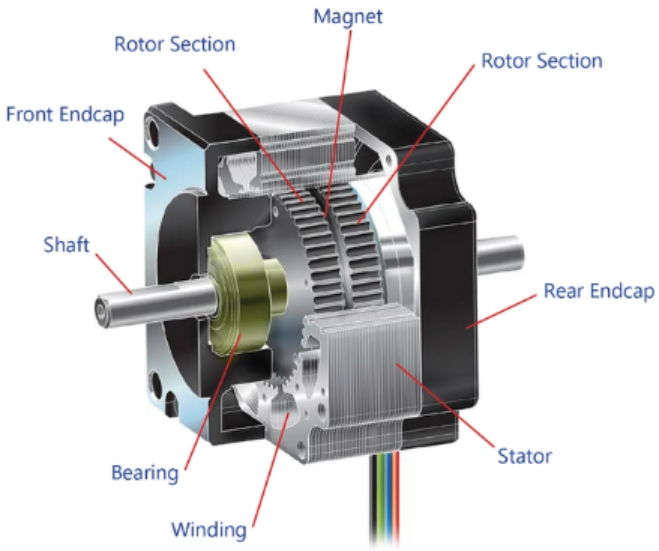

Figure 4.44: ***Mini-hybrid stepper motor, source [72].***

- One of the key advantages of this type of electric motor is its controllability. The simplicity of its electronic driver, combined with its high torque-to-power ratio, allows for the development of a functional deployment mechanism by directly controlling its stepping motion (in this case, 1.8°) and operating the stator-rotor assembly at lower speeds. This mechanical feature enhances the user's ability to control the mechanism, ultimately reducing both friction and heat generated by the contact between the booms and their support plate. Moreover, this design eliminates the risk of magnetic saturation, which typically limits the motor's peak torque capabilities;
- The electric motor utilization is designed with low-noise technology, achieved by operating at lower angular velocities. This is a typical design choice for extreme temperature missions, as in cryogenic conditions, the power budget may become limited. This technology is particularly well-suited for motors used in open-loop position control applications, where feedback mechanisms are not required. In contrast, *brush/brushless* and *piezo-electric* motors often

need a feedback positioning system, such as sensors or mechanical end-stoppers, to ensure accurate positioning;

- Stepper motors are often considered the best option for *microgravity* environments, especially when the design requires the ability to stop at multiple angular positions and control motion in both clockwise and counterclockwise directions. They are particularly suited for applications where speed and dynamic behavior do not demand excessively high rotational speeds, fast transfers, or short stabilization times. However, if these criteria are not met, the choice becomes less clear. In such cases, the motor may not function optimally on its own and could require additional electronic components for support;
- Their typical applications include solar array drives, cover plate openings, mechanical switches, and deployment mechanisms in general. The other motors mentioned earlier, such as *brushless*, *piezo-electric* and *brushed motors*, are primarily used for applications like reaction wheels, valve actuations, attitude control systems, scanning devices, gyroscopes, and geared mechanisms.

4.6 Critical Aspects and Observations

- One of the most critical aspects to consider is the process of folding and fabricating the specified sail from a single large aluminized-Mylar film, without the use of adhesive sprays or tapes to join different sections. For this project, a cost-effective and time-efficient solution has been developed by selecting a compound film from a single, continuous roll that meets the required reflective properties, aiming to address the project's objectives while highlighting the key challenges involved. For example, it would be beneficial to explore the most suitable machine tools capable of producing this large, highly reflective sheet for future solar sail interplanetary missions. Such an exploration could improve manufacturing efficiency in terms of both time and cost, particularly when considering large-scale production, such as that required for assembling a larger lunar-orbital system close to instantaneous L_1^* points. The sail's 95% reflectivity requirement is taken from Mylar optical properties, though it remains unproven whether this is sufficient for optimal sail performance. To further substantiate these considerations, it could be possible to test the sail's ability to reflect incoming radiation by designing a sensor capable of measuring how much of the lunar albedo and solar radiation is reflected by aluminized *PET*. Although this isn't part of the original project scope, further investigation into solar sail's optical properties can enhance overall performances needed for future space-shading applications;

- In a potential future space application, the On-Board Computer *OBC* should provide direct control over the electric motor. However, for this project, it's necessary to implement a remote control of these electrical devices by writing several Python codes, allowing them to be tested using a joystick capable of operating over relatively long distances from its USB dongle. The main focus of the investigation regards the dongle's communication frequencies and its responsiveness to command inputs triggered by pressing designated buttons. Additionally, to verify the controller's effectiveness, a Raspberry Pi is set up to evaluate the connection between the stepper motor driver and the USB dongle. The system is tested by observing whether button presses were correctly read by the command prompt using a binary system (1 for true and 0 for false), similar to the way Boolean variables are utilized;

- One of the most critical issues is related to single-point electric motor's failure. As a potential area for further investigations, it's suggested to explore ways to increase spindle's stability and determine optimal shaft's angular velocities to prevent damage, such as rips or strains in the sail, carried-on by adopted folding techniques. Additionally, significant time was dedicated to establish the best method for securing the spindle to the electric motor's rotating shaft,

exploring options such as feather keys, screws, pins, and tabs;

- A key-finding to delve on is to learn more about stresses and plastic strains induced to the spindle by screws. This would involve exploring the possibility of replacing them with more advanced technological solutions, especially after conducting thermal and structural simulations to assess the threads' response to stress. These simulations could help determine the optimal screws for connecting the mechanism's components, taking into account cumulative effects and ensuring reliable performances under stresses;
- It is essential to thoroughly investigate the method by which all four vertices of the square-shaped sail can be safety attached to an adjacent solar sail, this to develop the final orbital assembly. Various solutions can be adopted, such as magnetic connectors or docking systems equipped with mechanical hooks, which would allow a durable connection, but also enabling the sail to detach when necessary. This designing aspect plays a crucial role in ensuring flexibility and functionality, particularly in scenarios where solar sails must be deployed or retracted. Furthermore, careful considerations are given to the overall coupling process, as it is critical in facilitating the integration of multiple CubeSats into a cohesive system.

Chapter 5

Conclusions

This project focuses on a precursor mission design pursued to reduce the incoming solar radiation to mitigate climate change on Earth, based on solar sailing technologies. The project discusses about solar sail's translational and rotational dynamics in Earth-Moon orbital plane and concluding it with a conceptual framework of its deployment mechanism.

The Bi-Circular Restricted Four-Body Problem is exploited to model orbital dynamics, taking into attention gravitational forces and external disturbances acting on the solar sail like solar radiation pressure and reflected part from Earth and Moon. The solar sail's orbital trajectory is assumed being close to the cislunar equilibrium point L_1 belonging to the Earth-Moon orbital plane. Additionally, technological limitations from past solar sail missions have been considered, including deployment radius, mass, insulation factors and CubeSat platform specifications. The solar sail's projected shadow cone could be achieved from technological validation processes from both proposed preliminary design and literature researches.

The attitude and orbital trajectory of the Precursor mission are analyzed using a specific formulation expressed in the form of Solar Radiation Pressure Control Law. This technique aims to determine the ideal control that actuation devices may apply to properly orient the solar sail. For instance, the selected orbital trajectory follows a linear path along the x-axis around L_1 located onto the Earth-Moon conjunction-line, with the y and z-axis motions set to zero over one simulation period. The proposed control logic can be easily applied to specific *HALO* families studied for Planetary Sunshade modeling in the Sun-Earth orbital plane, then adapted to Earth-Moon Cartesian coordinate system. These families are intended to provide different trajectories' perspectives with the primary purpose of assuring periodical attitude angles' α and δ w.r.t. Sun's motion in synodic reference frame.

The concluding chapter focuses on developing the solar sail deployment mechanism, encompassing static and vibrational analyses, electronic integration, and final laboratory testing validation. Key contributions are centered on the design and refinement of critical components, with particular attention given to electronics' integration and solar sail's stowage configuration in alignment with structural components. The project design is exemplified by choosing a simpler and scaled solar sail's modeling. Additionally, the research highlights those technological complexities oriented to the fabrication of large square-shaped solar sails, in particular material's selection, electronic systems, and advanced manufacturing techniques. These challenges are compounded by constraints related to folding methodologies and payload volume limitations given by typical CubeSat sizing orders. Decision matrices are employed to identify the optimal materials and electric motor configuration, with laboratory testing putting into foreground the empirical validation of these trade-offs. The deployment mechanism is intended to reduce both its volume and mass. The proposed approach underscores the potential for developing lightweight and compact deployment systems, paving the way for future space applications in small satellite missions.

Bibliography

[1] Matteo Bernardelli. *Cambiamenti climatici, ognuno faccia la sua parte*. 24/11/2022. URL: https://agronotizie.imagelinenetwork.com/agricoltura-economia-politica/2022/11/24/cambiamenti-climatici-ognuno-faccia-la-sua-parte/77702 (cit. on p. 2).

[2] GeoPop magazine. *Eruzione del Krakatoa*. May 2023. URL: https://www.geopop.it/leruzione-del-krakatoa-del-1883-cosa-accadde-e-perche-fu-cosi-letale/ (cit. on p. 3).

[3] World Vision staff. *Hurricane Katrina, Facts, FAQs and how to help*. Nov. 2023. URL: https://www.worldvision.org/disaster-relief-news-stories/2005-hurricane-katrina-facts (cit. on pp. 3, 4).

[4] Maurizio Encari. *The day after tomorrow, il film é ancora attuale?* Sept. 2022. URL: https://cinema.everyeye.it/articoli/speciale-the-day-after-tomorrow-film-roland-emmerich-attuale-58965.html (cit. on p. 4).

[5] *Geostorm*. Oct. 2017. URL: https://www.imdb.com/title/tt1981128/plotsummary/ (cit. on p. 5).

[6] Michael Irving. *Effects of Hurricane Katrina in New Orleans*. Apr. 2017. URL: https://newatlas.com/before-after-photos-glaciers-climate-change/49143/ (cit. on pp. 5, 6).

[7] Marcello Romano, Bruce Chesley, Catello Leonardo Matonti, S. Sita Sonty, and Magdalena Gutowska. «Survey and comparison of in-space and in-atmosphere geoengineering concepts for climate change mitigation». In: *Paper ID: 75007, GLOC*. IAF Global Space Conference on Climate Change, 2023 (cit. on pp. 8, 9, 39).

[8] NASA Marshall Space Flight Center. *Sailing Among the Stars*. 8/17/10. URL: https://www.flickr.com/photos/nasamarshall/4919475067 (cit. on p. 11).

[9] Marcello Romano, Bruce Chesley, Catello Leonardo Matonti, S. Sita Sonty, and Magdalena Gutowska. «A Conceptual Framework for Climate Change mitigation Actions employing In-Space Geoengineering». In: 74th International Astronautical Congress (IAC), Baku, Azerbaijan, 2023 (cit. on pp. 11, 13).

[10] Catello Leonardo Matonti and Marcello Romano. «New Families of Halo Orbits about the Photo-Gravitational Equilibrium in the Sun- Earth–Moon System's Center of Mass Elliptic Restricted Three Body Problem for Planetary Sunshade Missions». In: () (cit. on p. 12).

[11] Catello Leonardo Matonti et al. «A Roadmap toward a Planetary Sunshade for Space-based Solar Geoengineering». In: () (cit. on p. 12).

[12] Catello Leonardo Matonti and Marina Coco. *Solar Sails swarm space infrastructure*. 24/11/2022. URL: https://www.linkedin.com/posts/catello-leonardo-matonti_planetarysunshade-climatechange-space-activity-7256604743781732352-M9WL?utm_source=share&utm_medium=member_desktop (cit. on p. 13).

[13] Bruce Murray Space Image Library The Planetary Society. *Halley's Comet solar sail concept*. 2024. URL: https://www.planetary.org/space-images/halleys-comet-solar-sail (cit. on p. 14).

[14] RAND Research Group. *Why not space mirrors?* Oct. 2022. URL: https://www.rand.org/pubs/commentary/2022/10/why-not-space-mirrors.html (cit. on p. 15).

[15] Louis Friedman. *STARSAILING, Solar-Sails and Interstellar Travel*. Boston Public Library: The Wiley Science editions, 1988 (cit. on p. 16).

[16] Allan I. S. McInnes. «Strategies for Solar-Sail mission design in the circular restricted three-body problem». M. Eng. thesis. Purdue University, 2000 (cit. on pp. 21, 34).

[17] Colin R. McInnes. *Solar-Sailing: Technology, Dynamics and Mission Applications*. Springer-Verlag Berlin Heidelberg GmbH, Chapter 5, Chapter 2, 1999 (cit. on pp. 23, 37).

[18] Guido Colasurdo and Giulio Avanzini. *Astrodynamics, SEEDS, Space Exploration and Development Systems, cap. Lunar trajectories, Restricted Circular Three-Body Problem,* Third edition 2007-08, Version 2.0.1, Politecnico di Torino (cit. on p. 24).

[19] *What is a Lagrange Point?* URL: https://science.nasa.gov/resource/what-is-a-lagrange-point/ (cit. on p. 24).

[20] Catello Leonardo Matonti. «Guidance, Navigation and Control design for final approach Rendezvous operations about cislunar Near Rectilinear Halo OrbitsLocation of the Equilibrium points (cap 2.5.2)». M. Eng. thesis. Facoltà di Ingegneria civile e industriale, Università di Roma La Sapienza, 2020/2021 (cit. on p. 24).

[21] Chiara Finocchietti. «Studio Preliminare di Missioni Spaziali a Bassa Spinta verso Orbite Lyapunov Verticali». M. Eng. thesis. Università degli studi di Pisa, 2010/2011 (cit. on p. 27).

[22] Gregory Archambeau, Philippe Augros, and Emmanuel Trelat. «Eight Lissajous orbits in the Earth-Moon system». In: HAL Open-Science, 2008 (cit. on p. 27).

[23] Marco di Lorenzo. *L'ORBITA AUREOLA NON RETTILINEA*. Sept. 2020. URL: https://aliveuniverse.today/rubriche/approfondimenti/4820-l-orbita (cit. on p. 27).

[24] Element-115. URL: https://www.artstation.com/artwork/Ze644w (cit. on p. 28).

[25] European Space Agency. *Euclid overview, Science and Exploration, Space science*. July 2023. URL: https://www.esa.int/Science_Exploration/Space_Science/Euclid_overview (cit. on p. 27).

[26] ASI Agenzia Spaziale Italiana. *Euclid*. URL: https://www.asi.it/esplorazione/cosmologia/euclid/ (cit. on pp. 27, 28).

[27] NASA. *Themis mission overview*. Feb. 2007. URL: https://science.nasa.gov/mission/themis-artemis/ (cit. on p. 27).

[28] *10 Years Strong with NASA's THEMIS Mission*. URL: https://moon.nasa.gov/news/14/10-years-strong-with-nasas-themis-mission/ (cit. on p. 29).

[29] ASI Agenzia Spaziale Italiana. *Lisa-Pathfinder*. URL: https://www.asi.it/esplorazione/cosmologia/lisa-pathfinder/ (cit. on p. 28).

[30] European Space Agency. *Lisa-Pathfinder operations*. Dec. 2015. URL: https://www.esa.int/Enabling_Support/Operations/LISA_Pathfinder (cit. on pp. 28, 29).

[31] NASA Blogs Home. *Monitoring Webb's Mirrors for Optimal Optics*. Nov. 2024. URL: https://blogs.nasa.gov/webb/ (cit. on pp. 29, 30).

[32] NASA. *James-Webb Space Telescope overview*. Dec. 2021. URL: https://webb.nasa.gov/content/about/orbit.html (cit. on p. 29).

[33] P. Mazzoldi, M. Nigro, and C. Voci. *Fisica, Volume 1*. Edises Editore, Seconda edizione, Meccanica e Termodinamica, Capitolo 1, Paragrafo 13, 1999 (cit. on p. 31).

[34] Kathleen C. Howell Brian P. McCarthy. «Quasi-Periodic orbits in the Sun-Earth-Moon Bicircular Restricted four-body problem». In: Purdue University, 2021 (cit. on p. 31).

[35] Andrea Caruso, Lorenzo Niccolai, Alessandro A. Quarta, and Giovanni Mengali. «Effects of attitude constraints on solar sail optimal interplanetary trajectories». In: Department of Civil and Industrial Engineering, University of Pisa, I-56122 Pisa, Italy, Published in Acta Astronautica, Vol. 177, December 2020, pp. 3947 (cit. on p. 34).

[36] Catello Leonardo Matonti, Erica Scantamburlo, and Marcello Romano. «New families of Halo orbits about the Photo-Gravitational Equilibrium between Sun and the Earth-Moon system for planetary Sunshade Missions». In: 74th International Astronautical Congress (IAC), Baku, Azerbaijan, 2023 (cit. on pp. 35, 53, 54, 59).

[37] P. Stepanek C. Rodriguez-Solano and U. Hugentobler. «Comparison of Earth radiation pressure models for DORIS satellites». In: Institut fur Astronomische und Physikalische Geodasie, Technische Universitat Munchen, Geodetic Observatory Pecny, Research Institute of Geodesy, Topography and Cartography in Zdiby, Venice, Italy, IDS Workshop 2012 (cit. on p. 36).

[38] Carlos Javier Rodriguez Solano. «IMPACT OF ALBEDO MODELLING ON GPS ORBITS». M. Eng. thesis. Earth Oriented Space Science and Technology, Technische Universitat Munchen, 2009 (cit. on p. 37).

[39] Barbara Cohen Les Johnson, Leslie McNutt, and Julie Castillo-Rogez. «Solar-Sail Propulsion for Interplanetary CubeSats». In: NASA MSFC and NASA JPL, Propulsion Energy, 2015 (cit. on p. 38).

[40] Andrew J Tang and Xiaofeng Wu. «An Interplanetary Mission Design of a Solar-Sailing CubeSat to Mars». In: *NSW, Journal of Physics: Conference Series, Australia* (2006) (cit. on p. 38).

[41] P. Mazzoldi, M. Nigro, and C. Voci. *Fisica, Elettromagnetismo e Onde, Terza edizione, Capitolo 3, Paragrafo 2, NOTA*. Edises Editore, a cura di R.C. Iotti, G. Barbero, 1998 (cit. on p. 39).

[42] Colin R. McInnes. «Space-based geoengineering: challenges and requirements». In: Special Issue Paper, September 15 2009 (cit. on p. 40).

[43] Kristina Hogstrom. «Small but Powerful: State of the Art in Small Flight Systems». In: Jet Propulsion Laboratory, California Institute of technology, Keck Exploring Once-in-a-Lifetime Targets Short Course, 10/29/18 (cit. on p. 42).

[44] ESA Agency. *Proba-3, il creatore di eclissi solari dell'ESA*. Apr. 2024. URL: https://www.esa.int/Space_in_Member_States/Italy/Proba-3_il_creatore_di_eclissi_solari_dell_ESA (cit. on p. 49).

[45] Osservatorio Astrofisico di Torino INAF Istituto Nazionale di Astrofisica. *Proba-3*. URL: https://www.oato.inaf.it/progetti/proba3/ (cit. on p. 49).

[46] Giulio Avanzini. *Spacecraft Attitude Dynamics and Control*. Dinamica e controllo di Assetto di satelliti, Politecnico di Torino, 2008/2009 (cit. on pp. 52, 65–67).

[47] Elisa Capello. *Passive and Active stabilization, Dinamica e controllo di veicoli spaziali, Chapter 3b, Politecnico di Torino*. 2021/2022 (cit. on p. 52).

[48] «CubeSat Design Specification Rev. 14.1, The CubeSat Program, Cal Poly SLO». In: (2024) (cit. on pp. 73, 79).

[49] Craig Underwood, Andrew Viquerat, Mark Schenk, and Ben Taylor. *InflateSail de-orbit flight demonstration results and follow-on drag-sail applications, InflateSail, eoPortal, Satellite Missions Catalogue*. Sept. 2014. URL: https://www.eoportal.org/satellite-missions/inflatesail (cit. on p. 73).

[50] Celeste R. Smith, Lacey M. Littleton, E. Glenn Lightsey, and Daniel Cavender. «Assembly Integration and Test of the Lunar Flahlight Propulsion System». In: *AIAA SciTech Forum* (Jan. 2022) (cit. on p. 73).

[51] Spacecraft and Stellar Exploration Inc. Satellites Planetary Society. June 2024. URL: https://spaceflight101.com/spacecraft/lightsail-a/ (cit. on p. 73).

[52] Planetary Society Space Exploration. *LightSail 2 spacecraft sucessfully demostrates flight by light*. Aug. 2019. URL: https://phys.org/news/2019-08-lightsail-spacecraft-successfully-flight.html#google_vignette (cit. on p. 73).

[53] Thomas Svitek Chris Biddy. «LightSail-1 Solar Sail Design and Qualification». In: Planetary Society, Stellar Exploration Inc. , Proceedings of the 41st Aerospace Mechanisms Symposium, Jet Propulsion Laboratory, Jan. 2022 (cit. on p. 74).

[54] Juan M. FERNANDEZ. «Advanced Deployable Shell-Based Composite Booms for Small Satellite Structural Applications Including Solar Sails». In: NASA Langley Research Center, Structural Dynamics Branch (cit. on p. 74).

[55] Leslie McNutt, Les Johnson, Dennon Clardy, Julie Castillo-Rogez, Andreas Frick, and Laura Jones. *Near-Earth Asteroid Scout, NASA Marshall Space Flight Center, Jet Propulsion Laboratory, Pasadena, American Institute of Aeronautics and Astronautics* (cit. on p. 74).

[56] Juan Orphee, Ben Diedrich Andrew Heaton, and Brandon C. Stiltner. «Solar-Torque Management for the Near-Earth Ateroid Scout CubeSat using Center of Mass position control». In: NASA MSFC, Jacobs ESSSA Group, Paper (cit. on p. 74).

[57] *NanoSail-D2, eoPortal, Satellite Missions Catalogue*. June 2012. URL: https://www.eoportal.org/satellite-missions/nanosail-d2#mission-status (cit. on p. 74).

[58] JD.C. Alhorn. «FeatherSail, The next generation of Nano-Class sail vehicle». In: Marshall Space Flight Center (MSFC) (cit. on p. 74).

[59] *CubeSail, Surrey Space-Center, Space Missions*. URL: https://www.surrey.ac.uk/surrey-space-centre/missions/cubesail (cit. on p. 74).

[60] R. L. Burton, J. K. Laystrom-Woodard, G. F. Benavides, D. L. Carroll, V. L. Coverstone, G. R. Swenson, A. Pukniel, A. Ghosh, and A. D. Moctezuma. «Initial Development of the CubeSail/Ultrasail spacecraft». In: CU Aerospace, L.L.C. , University of Illinois at Urbana-Champaign, Aug. 2014 (cit. on p. 74).

[61] Solar sail's materials Matthew Hernandez: Carbon Fiber Reinforced Polymers (CFRP): Material Properties and MatWeb: Datasheets American Durafilm: Physical Properties of KAPTON. URL: https://www.matweb.com/search/datasheet.aspx?matguid=f1cb670bd777424c925a8276d1aacf5e&ckck=1 (cit. on p. 75).

[62] Mylar (Polyester). URL: https://www.morettisrl.it/catalog/film-mylar/ (cit. on p. 75).

[63] CubeSat Solar Sail Lightning Talk. URL: https://www.youtube.com/watch?v=JE9YeO7yDrw (cit. on p. 83).

[64] Jingyao Sun, Jingjing Shen, Shoukai Chen, Merideth A. Cooper, Hongbo Fu, Daming Wu, and Zhaogang Yang. *Nanofiller Reinforced Biodegradable PLA/PHA Composites: Current Status and Future Trends*. 7/05/2018 (cit. on p. 95).

[65] FormLabs. *Engineering material, Nylon 12 Powder For Strong, Functional Prototypes and End-Use Part*. Nylon 12 Powder is specifically developed for use on the Fuse 1, 2020 (cit. on p. 96).

[66] H. Jimin and F. Zhi-Fang. *Modal Analysis* (cit. on p. 97).

[67] S. Nasir Adeli and Advisor Vaios J. Lappas. «Deployment System for the CubeSail nano-Solar Sail Mission». In: () (cit. on p. 104).

[68] Electric motors datasheet. *ASTROSYN MY180, MY5002*. URL: https://cpc.farnell.com/astrosyn/my5002/stepper-motor-11-50mm/dp/mc01838?mckv=s_dc%7Cpcrid%7C490691434472%7Ckword%7C%7Cmatch%7C%7Cplid%7C%7Cslid%7C%7Cproduct%7CMC01838%7Cpgrid%7C81075586787%7Cptaid%7Cpla-1211575637034%7C&CMP=KNC-GUK-CPC-SHOPPING-946695261-81075586787-MC01838&s_kwcid=AL!5616!3!490691434472!!!network (cit. on p. 111).

[69] Electric motors datasheet. *MAXON MOTOR, 517598 series* (cit. on p. 111).

[70] Electric motors datasheet. *McLENNAN, 1271 series*. URL: www.mclennan.co.uk (cit. on p. 111).

[71] Electric motors datasheet. *MFA/ComoDrills, 950D SERIES 35mm SINGLE RATIO METAL GEARBOX, 986D SERIES 52mm DIA (EPICYCLIC) METAL GEARBOX*. URL: https://www.mfacomodrills.com/motors/motors.html (cit. on p. 111).

[72] *Hybrid stepper motors*. URL: https://www.linengineering.com/technology/hybrid-stepper-motors (cit. on p. 117).

[73] E. Favre, P. Gay-Crosier, N. Wavre (ETEL), and M. Verain (ESA/ESTEC TOS-MM The Netherlands). «European Electric Space rated motors handbook». In: *ETEL Motion Technology* (Feb. 2024) (cit. on p. 117).